Concurrent multiscale modelling for heterogeneous materials with CutFEM

Ehsan Mikaeili

Supervisors: Prof. Pierre Kerfriden
Dr. Susanne Claus
Prof. Tony Jefferson

A thesis submitted to the graduate school in fulfillment of the requirements for the degree of Doctor of Philosophy
Cardiff School of Engineering

May 2023

Abstract

Computational modelling of heterogeneous materials with complex microstructures is challenging due to their multiscale nature. While direct numerical simulations lead to accurate results, it is not tractable for large-scale models. Therefore, in this thesis, two novel concurrent multiscale frameworks have been developed for tractable simulation of 2D/3D highly heterogeneous materials, including composites and trabecular bone materials. The difficulty of discretising such materials with complex microstructure is circumvented by using the cut finite element method (CutFEM). Then, two efficient zooming techniques are proposed for coupling micro and macroscale models. In our multiscale frameworks, the CutFEM technique is utilised to discretise the corresponding micro/macro interface besides the microstructure.

In the first framework, the smooth transition concurrent multiscale method, the two models are blended in a transition region and discretised over a single fixed computational mesh. While in the second framework, the two models have different meshes and are coupled over a sharp interface using Nitsche's method. In both frameworks, the CutFEM technology has been used for discretisation purposes that permits representing the microstructure and micro/macro interfaces in a mesh-independent fashion. This feature of CutFEM allows to (re)locate the zooming region(s) (the region(s) we require microscopic analysis) over a fixed background mesh arbitrarily, thus improving the robustness of multiscale modelling and analysis. In chapter 3, the efficiency and robustness of the smoothed concurrent multiscale method is demonstrated for 2D and 3D linear elasticity problems. Then, in chapter 5, the performance of the second concurrent multiscale framework with a sharp interface is tested for 2D linear elasticity and plasticity materials.

In chapter 4, the smoothed concurrent multiscale method developed in chapter 3 is extended for brittle fracture problems, which are a prevalent example of multiscale phenomena. According to the literature, fracture initiation starts in microscopic length scales by an accumulation of micro cracks in a process zone that eventually leads to the creation of macro cracks. In this thesis, the phase field model has been adopted for the fracture problem, which considers the fracture in a diffusive way. Since phase field models suffer from demanding extremely refined meshes to represent cracks, an efficient numerical framework is essential to balance accuracy and computational costs. In chapter 4, we show that our smoothed concurrent multiscale framework is a suitable choice for such problems.

Declaration

DECLARATION
I declare that this work has not previously been accepted in substance for any degree and is not concurrently submitted in candidature for any degree.

Signature: Ehsan Mikaeili Date: 31 May 2023

Statement 1
This thesis is being submitted in partial fulfillment of the requirements for the degree of PhD.

Signature: Ehsan Mikaeili Date: 31 May 2023

Statement 2
This work is the result of my own independent work/investigation, except where otherwise stated. Other sources are acknowledged by explicit references.

Signature: Ehsan Mikaeili Date: 31 May 2023

DECLARATION
I hereby give consent for my thesis, if accepted, to be available for photocopying and

for inter-library loan, and for the title and summary to be made available to outside organisations.

Signature: Ehsan Mikaeili Date: 31 May 2023

Acknowledgement

This dissertation is the outcome of my research work that was carried out between 2018 and 2022 at Cardiff University. This work is part of the Rapid Biomechanics Simulation for Personalized Clinical Design (RAINBOW) project, funded by the European Union's Horizon 2020 research and innovation program under the Marie Sklodowska-Curie grant agreement No. 764644.

First and foremost, I would like to express my heartfelt gratitude to my supervisors, Prof. Pierre Kerfriden, Dr. Susanne Claus and Prof. Tony Jefferson, for their assistance, guidance, and unwavering support throughout my Ph.D. journey. Their deep knowledge in the field of computational mechanics, came as a tremendous benefit to my research. Undoubtedly, the achievement of this dissertation would not have been feasible within the time frame of the project if it had not been backed by their excellent and careful scientific support. I am grateful for their mentorship, patience, and trust in me to explore this fascinating topic.

Furthermore, I am deeply grateful to the friends I have made through the RAINBOW network and at Cardiff University. The mutual support we gave each other was essential to keep motivated and consistent in the research.

I would like to acknowledge Prof. Miguel Otaduy from the University of Rey Juan Carlos in Madrid for hosting my secondment during my research. Although we did not have a direct collaboration, I had the privilege of conducting research in his lab and learned a great deal from his exemplary manner, discipline, and humbleness. His presence and the atmosphere of his lab had a profound impact on my research experience, and I am thankful for the valuable lessons I gained from observing his approach to academia.

I would also like to extend my gratitude to the examination committee members, Prof. Rubén Sevilla and Dr. Abhishek Kundu, for their thorough evaluation and constructive feedback on this thesis. Their insightful comments and suggestions have significantly contributed to improving the quality of this work. I am thankful for their time, expertise, and valuable inputs throughout the examination process.

Lastly, I am profoundly grateful to my family and loved ones for their unwavering support, encouragement, and understanding throughout this journey. Their belief in me has been a constant source of motivation and inspiration.

Contents

List of Figures

List of Tables

Acronyms

AES Assumed Enhanced Strain.

ALE Arbitrary Lagrangian-Eulerian.

BFGS Broyden Fletcher Goldfarb Shanno.

CAD Computer Aided Design.

cgFEM cartesian grid Finite Element Method.

CuFEM Cut Finite Element Method.

CZM Cohesive Zone Method.

DDM Domain Decomposition Method.

FCM Finite Cell Method.

FEM Finite Element Method.

GFEM Generalised Finite Element Method.

LEFM Linear Elastic Fracture Mechanics.

LSM Level Set Method.

MMTT Modified Mori-Tanaka Technique.

MTT Mori-Tanaka Technique.

PDE Partial Differential Equation.

PFM Phase Field Method.

PUFEM Partition of Unity Finite Element Method.

PUM Partition of Unity Method.

SDM Strong Discontinuity Method.

VBFEM Voxel-Based Finite Element Method.

XFEM Extended Finite Element Method.

XIGA Extended Isogeometric Analysis.

Nomenclature

$\bar{\mathcal{H}}$	Phase field history function
$\bar{\phi}$	Porosity parameter in modified Mori-Tanaka homogenisation
Γ	Discrete crack
Γ_d	Crack density function
$\mathcal{D}^h$	Scalar-valued continuous piecewise linear space for phase field
$\mathcal{U}^h$	Vector-valued continuous piecewise linear space for displacement field
Φ	Total energy
Ψ_d	Damaged solid strain energy function
τ	Traction
B_v	Bone volume fraction
V_t	Total volume in modified Mori-Tanaka homogenisation
V_v	Void volume in modified Mori-Tanaka homogenisation
W	Energy required for creation of two new surface during fracturing
α	Blending (mixing) function
$\bar{\beta}$	Ghost penalty regularisation parameter for phase field

β	Ghost penalty regularisation parameter for displacement field
ℓ	length scale parameter
ϵ	Half size of smoothening length
γ	Nitche's penalty term
λ	Lamé parameter
$\mathcal{F}_G$	Cut elements edges
$\mathcal{F}_{G_T}$	Cut elements edges in transition region
$\mathcal{H}$	Hierarchical multiresolution mesh characteristic parameter
$\mathcal{Q}_h$	Finite element space of continuous linear function
$\mathcal{Q}_\mathcal{T}$	Fictitious domain
$\mathcal{S}$	Smooth function
$\mathcal{T}$	Triangulation of background mesh
μ	Lamé parameter
$\nabla \cdot \sigma$	Divergence of Cauchy stress
ν	Poisson's ratio
Ω	Domain of interest
Ω^h	Fixed background mesh
$\partial\Omega_t$	Neumann boundary condition
$\partial\Omega_u$	Dirichlet boundary condition
ϕ	Signed distance level set function

Π	Total energy function
Ψ	Elastic energy density function
σ	Cauchy stress tensor
σ_d	Degraded (damaged) stress tensor
ε	Strain tensor
ε^{dev}	Deviatoric strain tensor
a	Bilinear form function
D	Hooke's tensor of isotropic linear elastic material
d	Phase field
$d_{\mathcal{M}}$	Macroscale phase field
d_m	Microscale phase field
E	Young's modulus
f_b	Body force
g	Critical energy release rate per unit area
G	Shear modulus
h	Mesh size parameter
$H^1(\Omega)$	Hilbert space (one)
K	Bulk modulus
l	Linear form function
n	Vector normal

q	Virtual phase field
s	Ghost penalty regularisation term
u	Displacement field
v	Virtual displacement field

List of contributions

Papers in Referred Journals

Ehsan Mikaeili, Susanne Claus, Pierre Kerfriden. "Concurrent multiscale analysis without meshing: Microscale representation with CutFEM and micro/macro model blending".

In: Computer Methods in Applied Mechanics and Engineering 393 (April 2022)

DOI: https://doi.org/10.1016/j.cma.2022.114807

Papers preprints on arXiv

Ehsan Mikaeili, Susanne Claus, Pierre Kerfriden. "Local uncovering of unresolved physics in structural mechanics: seamless choice of modelling resolution using a CutFEM level-set approach". (January 2022)

DOI: https://doi.org/10.48550/arXiv.2201.04698

To be submitted to the International Journal for Numerical Methods in Engineering.

Papers under preparation

Ehsan Mikaeili, Susanne Claus, Pierre Kerfriden. "A concurrent multiscale framework for phase field fractures based on CutFEM".

Ehsan Mikaeili, Bernhard Schrefler, Susanne Claus, Pierre Kerfriden. "A stable unfitted finite element method for shear band modelling in unsaturated porous media".

Introduction

Motivation. Highly heterogeneous structures, such as composites and porous media, are commonly used in many engineering fields due to their high efficiency and performance. Accurately predicting the behaviour of these structures is essential for advancing or optimising their engineering analysis and design. However, due to the multiscale nature and rapid spatial variations in material properties of such structures, their computational modelling poses a significant challenge. For instance, composites are commonly used in aerospace engineering to reduce weight and improve the performance of aircraft structures. However, designing advanced composites requires a deep understanding of their behaviour at different length scales. Similarly, the application of porous materials such as soil and concrete in civil engineering requires accounting for behaviours at more than one length scale because of their complex properties.

Direct numerical simulation methods for modelling and analysis of such structures are computationally expensive and may not be tractable when dealing with large-scale structures. Homogenisation methods, which pass data from small to large length scales to obtain the properties of such materials, have been widely used to overcome this challenge. However, these methods suffer from drawbacks, including macroscopic uniformity and RVE periodicity assumptions. The uniformity assumption is not satisfied in critical regions of high gradients like interfaces, complex geometries with sharp angles, and severe plasticity and softening regions. The periodicity assumption is also not fulfilled when the material's microstructure is nonuniform.

Concurrent multiscale methods [2, 3, 4] have been developed to overcome the limitations of homogenisation methods and enable efficient computational modelling

of highly heterogeneous structures by bridging the microstructural and homogenised macroscale descriptions efficiently. These methods divide the computational domain into separate sub-domains, where each sub-domain requires different levels of discretisation resolution and/or different length-scale constitutive models. The primary motivation of concurrent multiscale modelling is (i) to adopt a localised complex model for the regions of interest undergoing critical phenomena (such as plasticity, fracture, complex microstructure, etc.) and not the entire domain; (ii) to employ different discretisation space for the regions of interest (ROI) and the surrounding region; (iii) to avoid creating a complex large scale model, which is a time-consuming task.

This thesis advocates utilising concurrent multiscale analysis based on CutFEM technology [5]. We aim to extend the CutFEM technology, as a fictitious domain method, for concurrent multiscale modelling of the heterogeneous structures undergoing linear elasticity, plasticity and fracture behaviours. Herein, the motivation is (i) to emulate the main advantage of the CutFEM in seamless and mesh-independent modelling of complex geometries within our microscale region and then employ a homogenised FEM model in the macroscale region; (ii) to adopt different discretisation space for the micro and macroscale regions, and investigate the CutFEM framework performance for the micro/macro concurrent coupling.

State of the art. One of the main challenges of the concurrent multiscale methods is choosing an appropriate coupling technique for linking the corresponding sub-domains. In the literature, several types of concurrent multiscale methods have been proposed that are mainly distinct in terms of their coupling approaches. We categorise these approaches into two groups of overlapping and non-overlapping. As shown in Figure 1, in non-overlapping approaches, two sub-domains (the microscale and macroscale sub-domains are denoted by Ω_m and $\Omega_{\mathcal{M}}$, respectively) are connected via a sharp interface Γ, while in overlapping approaches, the two sub-domains are partly overlapped and coupled over Ω_T (shown by yellow colour).

In non-overlapping techniques, also referred to as interface coupling, the coupling operators are implemented across the interface Γ, which is typically done by Lagrange

multipliers or Nitsche's method to enforce the continuity and compatibility conditions over the interface. In the Lagrange multipliers approach, extra unknowns are added to the system of equations associated with the Lagrange multipliers that increases the computational efforts [6]. The Nitsche's method, on the other hand, introduces a symmetric formulation that stabilises the bilinear form using a penalty term that must be sufficiently large and imposes the interface conditions weakly [7, 8]. The s-method [9] and the mortar method [10] are popular examples of non-overlapping coupling techniques that have demonstrated acceptable precision and efficiency in coupling various models with similar or different length scales.

The overlapping techniques, on the other hand, employ a surface coupling instead of the interface coupling to connect the different sub-domains, which is shown to reduce oscillatory irregular numerical solutions fields in their transition region Ω_T. These oscillations are ubiquitous when linking subdomains with different length scales such as continuum-atomistic [11, 12, 13] and continuum-molecular [14, 15]. However, this technique has also been demonstrated to be efficient for continuum-continuum problems [16]. The well-known examples of overlapping methods are the Arlequin method [17, 18], the bridging domain method [19, 20] and the works developed by [21, 22, 23].

Another challenge in concurrent multiscale methods is the discretisation of the computational domain, including the inside of sub-domains and the interface separating the sub-domains. This is crucial in particular when

- one deals with structures that own complex microstructures,
- the ROI is non-stationary or time-dependent, and the corresponding Γ or Ω_T alters during the simulation.

An efficient and robust approach for the discretisation of such problems is utilising a non-conforming method. Non-conforming or unfitted discretisation techniques intend to decouple meshing from geometry for problems involving embedded interfaces or complex geometries. This feature alleviates the remeshing necessity, which is a common issue in the context of fitted methods such as the finite element method

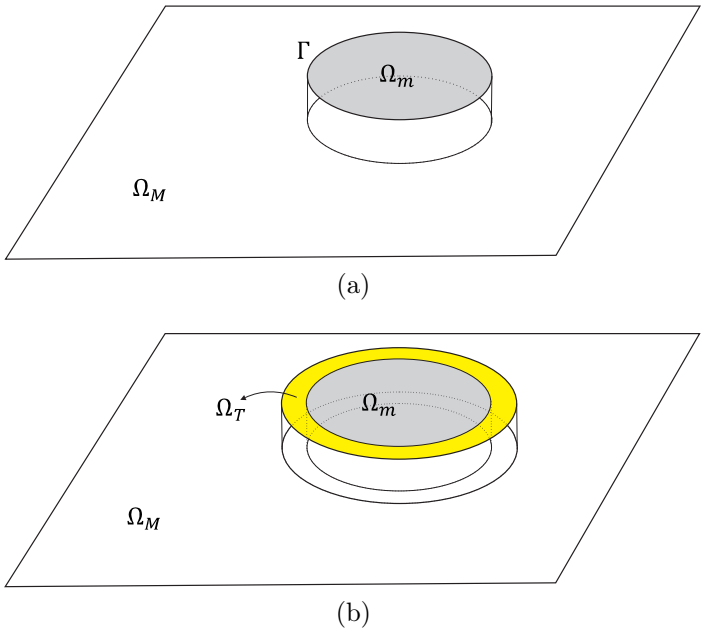

Figure 1: Various coupling techniques in concurrent multiscale methods: (a) non-overlapping technique and (b) overlapping technique. The microscale and macroscale models defined over Ω_m and $\Omega_{\mathcal{M}}$, respectively, are coupled either across an interface Γ with non-overlapping techniques or over a overlapping region Ω_T with overlapping techniques.

(FEM). However, the majority of previous concurrent multiscale methods were developed within fitted discretisation techniques.

In general, interface problems are covered by two categories of unfitted discretisation methods. The first group deals with embedded interfaces, such as cracks, while the second group focuses on immersed boundary modelling that aims to treat complex geometries in an arbitrary way. The extended finite element method (XFEM) [24] is probably the most well-known example of the first group that adds extra degrees of freedom for the intersected elements and employs suitable enrichment functions (such as Heaviside function) within the partition of unity method to account for discontinuities implicitly, in the solution field (instead of modelling the geometry of discontinuity explicitly, as done in the FEM). The XFEM has been applied to a wide range of problems in computational mechanics, including different types of fracture problems in full scales. But in the context of concurrent multiscale analysis, it has

been mainly used to represent cracks inside local sub-domains, see for instance [25].

Later on, authors in [5] proposed the CutFEM, which is considered as a generalisation of the XFEM for immersed boundary modelling. However, the enrichment technique in the CutFEM is different from the one used in the XFEM. In the CutFEM, an extra element is added to the element cut by interface; where each of the double elements represents different sides of the interface. Then, the overlapped elements are glued together with the Nitsche's method. Unlike the XFEM, which struggles with singularity issues when the interface intersects an element by being very close to its node(s), the CutFEM can handle such cases smoothly. This is due to the regularisation terms [26] that CutFEM implements in the formulation of cut elements. It is worth mentioning that the CutFEM without regularisation was originally proposed by [27] for linear elasticity problems.

The literature on CutFEM, similar to XFEM, is vast. Here, we will solely focus on the area of domain decomposition and multiscale modelling, as a thorough literature review is done in chapter 1. One of the most relevant works in this area is carried out by authors in [28], who developed a multi-mesh framework based on CutFEM for multi-component structures. In their methodology, each component of the large structure is meshed separately while each mesh is allowed to overlap the CutFEM fixed background mesh arbitrarily. Their method allows the CutFEM background mesh to be intersected by more than one interface (corresponding to the overlapped meshes) simultaneously. They use Nitche's method to enforce interface conditions in the intersected elements. In the context of concurrent multiscale modelling, however, to the author's best knowledge, there are no published papers by other authors using the CutFEM technique.

This thesis aims to extend the CutFEM for concurrent multiscale modelling of heterogeneous materials. The CutFEM represents the microscale geometry, which can be expressed in terms of an analytical distance function or a given surface mesh. In this thesis, we present two novel concurrent multiscale methods; each one features a novel coupling strategy for linking microscale and macroscale models.

In the first strategy, we adopt a mixing technique over a single computational mesh, which is refined in the ROI and coarse elsewhere. The mixing technique al-

lows us to mix or couple the microscale and macroscale models in their transition region Ω_T (a region where the two models are overlapped). This type of coupling strategy belongs to the class of smoothened overlapping methods, such as Arlequin or the Bridging Domain Method. In this technique, we intend to avoid the two common challenges mentioned previously associated with the concurrent multiscale modelling. To do so, we perform the glueing procedure "naturally", using a smoothening weight function to take an average of the microscale and macroscale models in their Ω_T, which we refer it as a smooth interface. In our multiscale framework, the smooth mixing strategy is inspired by the Arlequin method. However, contrary to the Arlequin mixing strategy, we do not cross and glue a high resolution mesh to the underlying mesh. Instead, we use a level set function over a single background mesh to define the Ω_T. Then, we blend the two scales in the elements inside the Ω_T. We demonstrate the efficiency of our framework for linear elasticity (chapter 3) and for phase-field fracture (chapter 4) problems.

In the second strategy, we propose another concurrent multiscale framework comprised of microscale and macroscale models that are separated with a sharp interface (instead of the smoothed interface in the first strategy). Here, we deal with two types of interfaces, including the interface representing the microstructure geometry, and the second interface separates the microscale model with microstructure from the surrounding homogenised macroscale. In this multiscale framework, we use CutFEM for two outstanding purposes. First, we represent the microstructure in Ω_m using CutFEM. Second, we discretise the micro-macro interface with CutFEM, which allows it to intersect the background mesh and microstructure interface arbitrarily. We treat the stability of the corresponding intersected elements by ghost penalty regularisation. This framework has been applied to problems with linear elastic and elasto-plastic behaviours.

Outline of the thesis. The structure of the thesis is as follows: Chapter 1 presents a literature review for the implicit frameworks for solving interface problems including unfitted domains and embedded interfaces.

Chapter 2 discusses different types of homogenisation techniques and domain

decomposition methods available in the literature of computational mechanics.

Chapter 3 shows the smoothed concurrent multiscale algorithm for 2D and 3D heterogeneous structures and presents the numerical results at the end of chapter.

Chapter 4 is comprised of two parts. The first part applies the proposed smoothed concurrent multiscale framework for phase-field fracture problems. In the second part, within an inverse problem framework, different homogenisation aspects of the phase-field problems are investigated.

Chapter 5 presents a novel multiresolution formulation based on CutFEM for concurrent multiscale modelling and the corresponding numerical results.

Chapter 6 summarises the main contributions proposed in the thesis and suggests future studies.

Chapter 1

Implicit interface PDEs solvers

1.1 Introduction

Many complex physical phenomena in scientific and engineering problems can be described through Partial Differential Equations (PDEs), such as structural and material behaviours, fluid-structure interaction and multiphysics diffusion problems. Finite element method (FEM) is deemed a robust numerical tool for solving PDEs. In the FEM, the governing PDE is discretised over the computational domain with elements that have a simple shape. The classical version of FEM requires a mesh that conforms or fits to the geometry of the physical body and small elements in the regions where the solution is less smooth. A schematic presentation for the conforming (fitted) FEM is shown in Figure 1.1a.

Constructing an accurate geometry and the corresponding meshing for problems with complex architecture and/or moving interface is a time-consuming task and makes the modelling stage with the classical FEM more cumbersome. For instance, crack propagation, laser ablation and tumour growth are the common time-dependent problems that need to update the initial mesh configuration during the simulation. Recent advances in high resolution imaging techniques have provided an invaluable tool for explicitly modelling problems mentioned above. They propose a simulation framework comprised of high resolution volumetric images embedded

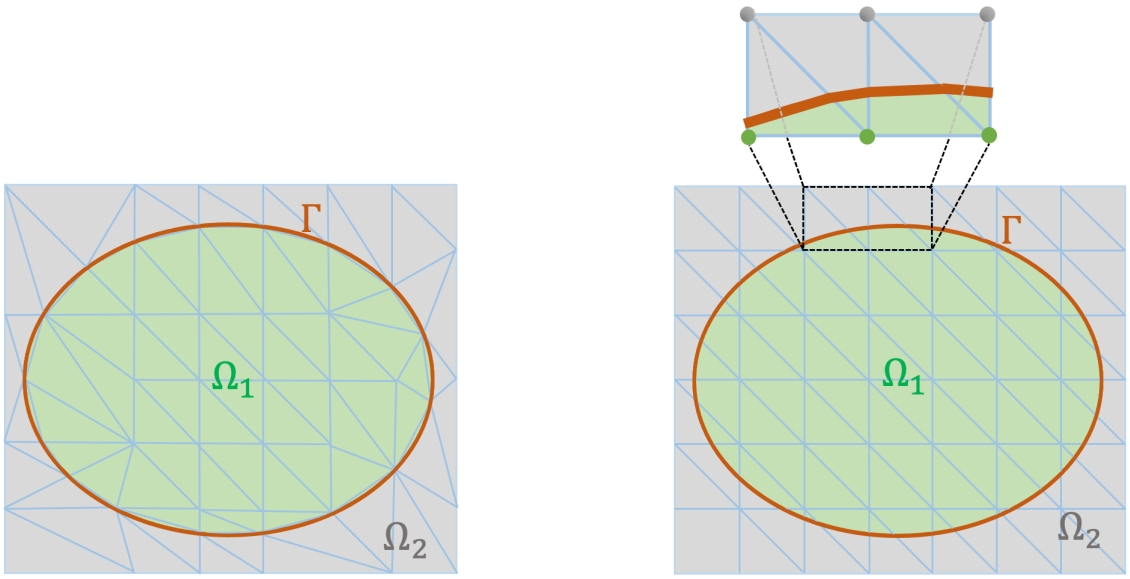

(a) (b)

Figure 1.1: Computational meshes; a) fitted FEM and b) unfitted FEM.

in the FEM, which take into account the actual architecture during the simulation. Within this context, Voxel-Based FEM (VBFEM) is considered a common approach proposed by [29] that generates conforming (fitted) finite element meshes with respect to the pixel values. VBFEM is applied successfully for problems in biomechanics [29, 30], material science [31], and solid mechanics [32]. Using VBFEM has the advantage of straightforward construction and bypassing the image segmentation stage [33, 34]. However, all these advantages are still subject to high computational costs (due to the fine mesh usage and remeshing), which limits the robustness and tractability of the approach when dealing with large-scale structures.

Despite the advantages of fitted FEMs in handling a wide range of problems with complex geometries and boundary conditions, alternative approaches are also available in the context of unfitted FEMs. Figure 1.1b illustrates a typical computational mesh used for arbitrary domains with unfitted FEMs. Unlike fitted FEMs (shown in 1.1a) where the mesh conforms to the actual physical geometry during the simulation, the unfitted FEM allows interfaces representing the geometry to cut

the elements in an arbitrary way. However, the cut elements in the unfitted FEMs require advanced numerical techniques, which will be discussed in the remainder of this chapter.

This chapter deals with a literature review on various unfitted FEMs that cover two categories of problems: (1) unfitted domains and (2) embedded interfaces. In section 1.2, we will discuss the well-known unfitted FEMs for the unfitted domain problems, namely the cut finite element method (CuFEM) [5], finite cell method (FCM) [35], cartesian grid finite element method (cgFEM) [36]. For the second category, in section 1.3, we will have a review of the extended finite element method (XFEM) [24], strong discontinuity method (SDM) [37, 38] and CutFEM. Besides, in the last section (1.4), we will review briefly a popular implicit fracture approach called the phase field method (PFM) [39, 40].

1.2 Unfitted FEMs for arbitrary domains

Due to the limitations and lack of flexibility of fitted FEMs in modelling time-dependent and complex geometries that require time-consuming geometry construction procedures, several unfitted FEMs have been proposed to handle these issues during the last few decades. As shown in Figure 1.1b, an immersed boundary modelling is the main feature of unfitted FEMs that are intended for such problems. In all unfitted FEMs, the aim is to decouple geometry construction from meshing. However, within unfitted approaches, the elements intersected with the boundaries require more versatile numerical algorithms to guarantee the accuracy of the solution field and robustness of the numerical method. The following will discuss the well-known unfitted FEMs for arbitrary domains, including CutFEM, FCM and cgFEM.

1.2.1 Cut Finite Element Method

CutFEM, as a fictitious domain method, aims to facilitate the computations of complex and evolving geometries [41, 5, 42]. The method is originated from the unfitted FEMs that are based on Nitsche's method and boundary stabilisation terms,

see for instance [6, 43, 41, 27, 44, 45]. The CutFEM presents the computational domain over a fixed background mesh, letting the interface corresponding to the domain cut through the mesh freely. In other words, it decouples the geometry of the physical problem from the finite element spaces and the background mesh. The main idea behind this method is to define the PDE and the geometry by the FE variational form. It is worth noting that the idea of computation and updating the geometry in the discretised formulation tremendously reduces the preprocessing costs of the meshing.

In CutFEM, a common interface tracking approach employed is the Level Set Method (LSM) which has been developed for several complex problems in the computational mechanics community, including laser ablation [46], neuro-cell morphologies [47], contact problems [48] and two-phase fluids [49]. There are also other tracking methods have also shown promising results when coupled with the CutFEM, including boundary meshes [50] and fast marching method [46].

The level set functions let us compute the intersection of the fixed background mesh with the interface $\Gamma(t)$ in a straightforward manner. This allows CutFEM to accurately track moving complex boundaries/interfaces without stability issues in 2D and 3D simulations. A schematic representation of $\Gamma(t)$ is shown in Figure 1.2.

In the LSM, a function $\phi(x,t)$ is applied to the space where the interface exists, where x denotes a point in the space and t is time. Signed distance function is a common type of function used in the LSM, in particular to ensure that ψ is not too flat or too steep near Γ. The signed distance function is defined as

$$\phi(x) = \|x - x_\Gamma\| \operatorname{sign}(n_\Gamma \cdot (x - x_\Gamma)) \tag{1.1}$$

where x_Γ is the closest point projection of x onto the discontinuity Γ, and n_Γ is the normal vector to the interface at point x_Γ. In this definition, $\|\|$ denotes the Euclidean norm, where $\|x - x_\Gamma\|$ specifies the distance of point x to the discontinuity Γ. By using the signed distance function in our LSM, the interface $\Gamma(t)$ is defined by $\phi(x,t) = 0$, while the exterior and interior points are given respectively by $\phi(x,t) > 0$ and $\phi(x,t) < 0$.

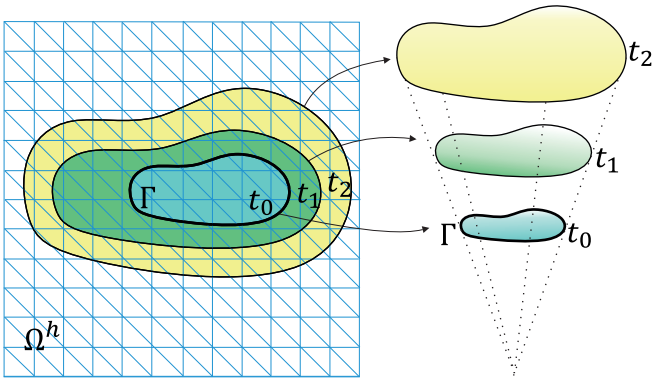

Figure 1.2: Schematic presentation of 2D level set functions at various times over the fixed background mesh Ω^h.

Aside from the efficient geometry description, the method ensures the stability of its discretisation technique by implementing ghost penalty regularisation terms in cut elements [26]. The terms are acted on the jumps of functions over the cut elements' edges. Authors in [51] show that similar stability as for the ghost penalty can be achieved with optimal approximation properties. This technique modifies the finite element space close to the boundary and extends it from the stable interior elements over the boundary in a stable way.

The enrichment strategy in CutFEM is based on an overlapping technique applied to intersected elements. In this enrichment method, for every element intersected by the interface, an extra element is added that overlaps the original element, and they represent two different solution fields from different sides of the interface. In this way of enrichment, the degrees of freedom in the cut elements are doubled. Any form of discontinuity in the solution field, including jumps and kinks, occurs without directly changing the stiffness matrix. Authors in [52] show that such enrichment can be reproduced with another well-known unfitted FEM called XFEM. CutFEM conventionally uses Nitsche's method for glueing together the overlapped domains and enforcing boundary conditions.

The Nitsche's method proposed originally by [53] is a variationally consistent method for enforcing Dirichlet boundary conditions weakly and has been used extensively for interface problems over the last two decades. It proposes a symmetric

formulation and stabilises the bilinear form using a penalty term that must be sufficiently large. Recently, [54] employed a nonsymmetric version of Nitsche's method for elliptic interface problems. They showed that their technique does not require sufficiently large parameters to guarantee stability, unlike the symmetric Nitsche method. However, in this thesis, we will use a symmetric version of the Nitsche for enforcing the interface conditions.

The CutFEM technology is applied for a range of weak discontinuity problems, such as unilateral contact [48], multiphysics phenomena [55, 56, 46], porous media flow [57], and fiber-reinforced composites [58]. It has also been recently developed for modelling multi-component structures using different meshes for each component by [59, 60], where multiple meshes can overlap over a fixed background mesh arbitrarily, and the intersected elements are regularised with the ghost penalty technique. CutFEM for fluid-structure interaction problems is another main application of the method that significantly reduces the burdensome of generating high quality meshes required with conventional methods such as arbitrary Lagrangian-Eulerian (ALE); see for instance, the work done by [61].

1.2.2 Finite Cell Method

The initial FCM proposed by [35] can be interpreted as a combination of a fictitious domain approach with high order finite element methods. The method employs high order elements for the cut elements with interfaces, which are decomposed into adaptive sub-elements. A large number of quadrature points are aggregated around the immersed boundary, allowing to resolve the discontinuity in the integrands of the variational formulation. Similar to the CutFEM, the physical domain is embedded in a geometrically larger domain that is discretised with structured mesh. However, the method has also been tested successfully with unstructured tetrahedral [62, 63] and polygonal meshes [64].

In FCM, the fictitious part of the computational domain is considered as a soft material which makes the discretisation of the embedding domain with standard FEM possible. The fast convergence to an accurate result, however, is due to the

fact that a high order Ansatz space is used [65]. The dense distribution of integration points serves to capture the boundary, as in level sets, and to increase the accuracy of integration over cells independent of the physical domain. The stabilisation analysis of FCM with Neumann and weakly forced Dirichlet conditions are carried out by [66] and [67], respectively.

The method has successfully been applied to a wide variety of applications, for instance, in solid mechanics [68], structural analysis [69], and fluid-structure interaction [70].

1.2.3 Cartesian Grid Finite Element Method

The cgFEM is another so-called unfitted FEM introduced for solving elasticity problems with arbitrary domains over a mesh made up of regular quadrilateral elements in 2D [36] or regular hexahedral elements in 3D problems [71]. This way of discretisation, which employs similar elements in the mesh, yields several computational advantages. Firstly, the similarity of elements helps to use the same integrand for the integrals of all elements by only scaling the obtained ones in a reference element. Secondly, in this method, using h-refinement leads to less computational costs as the projection of information between different mesh sizes is practical and straightforward.

Another main advantage of cgFEM is that it can consider the computer aided design (CAD) geometry for numerical integration. This makes cgFEM a suitable method to improve the gap measures. For instance, see [72, 73] for the application of the cgFEM in image-based structural analysis. The cgFEM is applied successfully for various problems in computational mechanics, including contact mechanics [74], plasticity [75], large deformation [76], and optimisation [36].

Similar to the FCM and the CutFEM, cgFEM deals with a fixed background mesh over Ω^h and a computational domain over Ω in which the mesh does not need to conform the geometry under the following condition: $\Omega^h \subset \Omega$. However, unlike classical versions of the FCM and the CutFEM that use triangular elements, the cgFEM employs quadrilateral elements in the background mesh [36]. As shown in

Figure 1.3, they apply distinct discretisation techniques for dealing with the arbitrary domains. In the CutFEM (1.3a), the cut elements are stabilised by the ghost penalty regularisation, particularly when the interface is close to a node and only a tiny portion of the cut element is left. In the FCM (1.3b), the cut elements are enriched with higher order elements where a softer stiffness is employed for the fictitious part of the domain to maintain the accuracy of the method. In the cgFEM (1.3c), the cut elements are hierarchically refined if the true geometry is not embedded in the Cartesian grid.

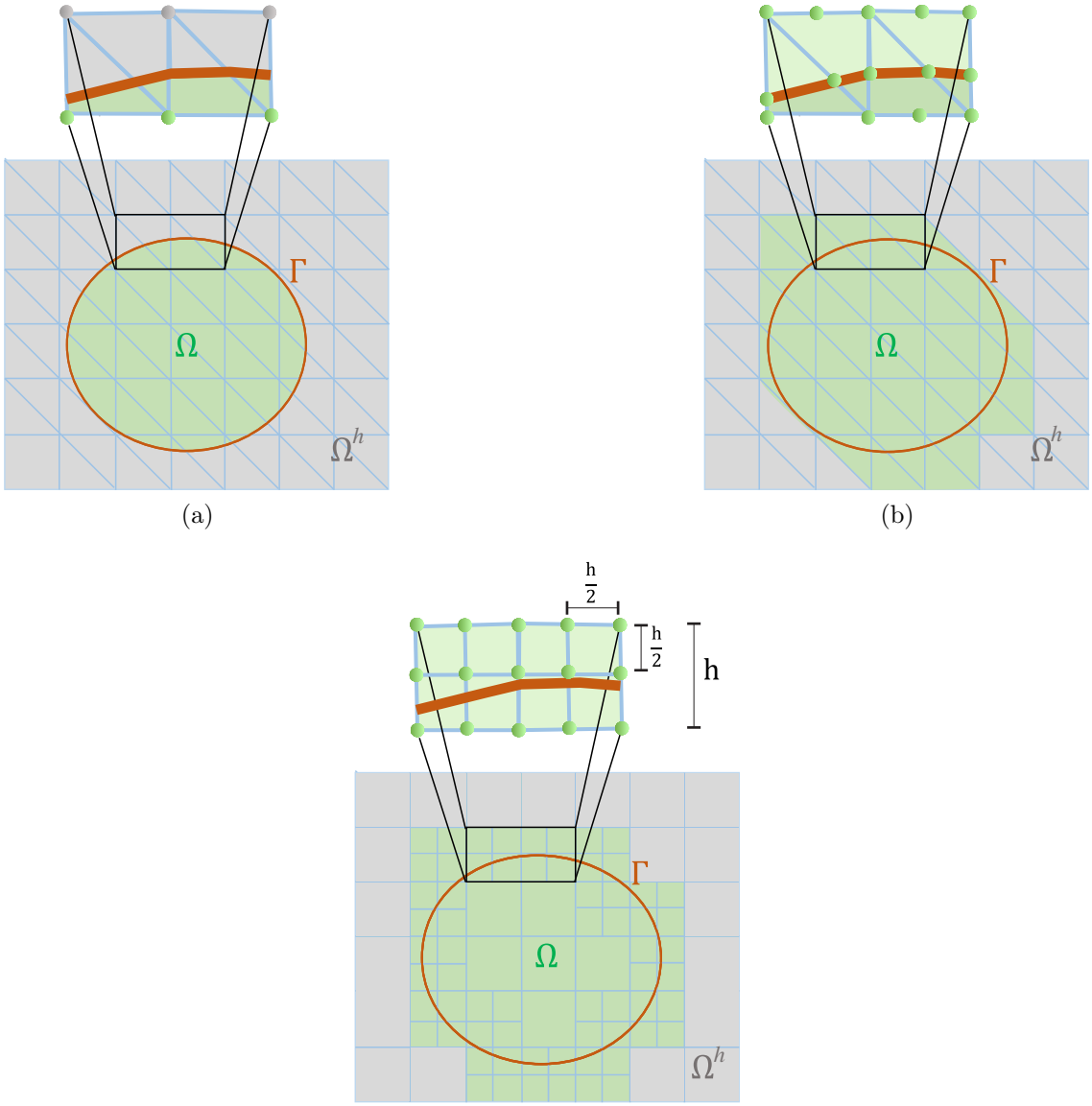

Figure 1.3: Schematic presentation of domain discretisation for different unfitted FEMs; a) CutFEM, b) FCM and c) cgFEM.

1.3 Unfitted FEMs for embedded interfaces

In recent decades, we have seen the development of classical FEM to geometrically unfitted FEMs, which cover problems with embedded interfaces such as cracks and shear bands. XFEM and SDM are well-known examples of such developments [37, 38]. These methods aim at decoupling geometry from meshing by enriching the solution field when required. Therefore, the conventional way of modelling any form of discontinuity (e.g. jumps or kinks) in the mesh in an explicit way is replaced with an implicit approach where the solution field is enriched with suitable enrichment functions over a fixed mesh. From a computational standpoint, the unfitted approaches permit an accurate description of the solution fields while saving a large number of degrees of freedom in comparison to the standard low order boundary-fitted techniques. These certainly explain their current popularity in the computational mechanics community for analysing complex problems.

The idea of enrichment technique was originally proposed by [77] that was able to deal successfully with the strong discontinuity with FEM. The method, which is assumed in the class of embedded elements, captures strong discontinuities in FE to improve the resolution of shear band localisation. In their method, additional DOF, due to localised deformation modes, are eliminated at the element level by static condensation. Based on this idea, [78] proposed a method to model strain localisation by imposing two parallel weak discontinuity lines in a single element so that the element was able to contain the band of localised strain. One of the distinct differences between these two methods is that the width of the localised band is smaller than the mesh size in the method proposed by [78]. In contrast, the localisation bandwidth is of the same size as the mesh size in the method by [77], and a very fine mesh was required to resolve the localisation band. In further work, [79] proposed a method based on displacement interpolated embedded localisation lines, which was insensitive to mesh size and distortions. This method was much more flexible than schemes that allow discontinuities only at element interfaces and was used easily to model the crack growth without remeshing. The idea was similar to the XFEM, which was developed a decade later by [80]; in fact, the embedded elements

introduce additional unknowns into the variational formulation. The XFEM has been proposed in modelling strong discontinuities from the earliest studies of the technique by [24, 81].

Another innovative method was also proposed by Hansbo and Hansbo [27] for modelling strong discontinuities, where the approximation was constructed from two different fields. In their method, the crack kinematics was obtained by overlapping elements instead of introducing additional degrees of freedom. The idea was based on the superposition of an additional element to the element cut by the discontinuity in order to construct the enriched displacement field. [82] presented that the Hansbo–Hansbo method can be derived from the standard XFEM technique by using a linear combination of the XFEM basis.

In the following, a review of the XFEM, SDM and CutFEM as popular unfitted FEMs for modelling discrete cracks will be presented. Then, the well-known phase field method as an implicit approach for modelling fracture problems will be introduced.

1.3.1 Extended Finite Element Method

The XFEM was initially introduced by [80, 24] for fracture problems. The method was developed based on the mathematical basis of the partition of unity finite element method (PUFEM) proposed by [83] that allows new capabilities while keeping the main advantages of FEM. In fact, with XFEM, we can model discontinuities or singularities in the solution field by introducing an appropriate set of enrichment shape functions while preserving the original geometry and mesh configuration. The conventional FEM requires a suitable mesh to preserve the accuracy when discontinuity or singularity happens in the solution field, for instance, the crack propagation in three dimensions, which is an arduous task. However, the XFEM can handle these situations over a fixed mesh using an appropriate enrichment function.

XFEM augments the FEM space with enrichment functions within the framework of the partition of unity method (PUM). The method adds additional degrees of freedom to the nodes close to the strong discontinuities and singularities and implements

enrichment functions locally to the conventional FEM approximation space [84]. The jump in the solution field is conventionally referred to as the strong discontinuity that can be considered a crack.

Apart from the extensive applications for fracture analysis (involving cracks enforcing strong discontinuity and singularities in the solution field), XFEM has also been successfully applied for arbitrary/moving domains. For instance, Sukumar et al. [85] developed new enrichment functions for modelling holes and inclusions and Chessa and Belytschko in [86] applied XFEM for two-phase flow with surface tension effects.

Coupling the computational methods related to tracking moving boundaries, such as the LSM, with the XFEM has created a powerful tool for simulating complex time-dependent geometries. The XFEM lets us represent the geometry in a mesh-independent fashion, and the level set technique simplifies the selection of enriching nodes and their implementation.

The first implementation of coupled XFEM and LSM in the modelling of voids and inclusions was performed in [85], where the LSM is used to represent the location of voids, inclusions, and material interfaces. Later, [87] used this technique to model micro structures with complex geometries and to present the capability of the model for the homogenisation of periodic basic cells. The method has also been applied for nano-materials by [88] to calculate the overall elastic properties of nano-materials with nano-scale interface effects and to determine the size-dependent effective elastic moduli of nano-composites with randomly distributed nano-pores. According to [89], the coupled XFEM and LSM technique has proven to be a suitable framework for the numerical homogenisation of heterogeneous materials with complex microstructures.

In the last two decades, the XFEM has been applied to a wide range of problems in computational mechanics, including contact mechanics [90], cracking [91], shear bands [92, 93, 94], damage [95, 96], multiscale [97, 98] and multiphysics [99, 100, 101]. The efficiency and popularity of the XFEM led it to be used in industrial problems as well, which has been implemented by famous companies such as LS-DYNA and ABAQUS.

1.3.2 Strong Discontinuity Method

Authors in [102] proposed an assumed enhanced strain (AES) framework to enhance the strain field for the elements showing locking due to their lack of bulk incompressibility and bending. The main motivation for the invention of AES was to treat elements with localised deformation. This framework was the basis of developing the strong discontinuity method (SDM), which is now considered as a popular unfitted FEM for interface problems.

The SDM was presented by Simo, Oliver and Armero [37] for modelling strong (displacement) discontinuity by taking into account the softening constitutive law and the interface traction-separation relation. Here, the displacement field is comprised of regular and enhanced components, while the enhanced term leads to a jump along the discontinuity interface. The SDM adds no additional degrees of freedom to the localised elements, which is achieved by the static condensation technique. The static condensation is used to eliminate the need for the element enhancement before the global assembly; therefore, no additional degrees of freedom are introduced into the global equation system. Moreover, the application of the static condensation for the constant strain triangular elements led to the well-known Galerkin embedded strong discontinuity method by [103].

The differences between the XFEM and SDM have been investigated by the [104, 105, 1]. The main distinction originates from their enrichment methods, where the XFEM enriches the nodes while the SDM enriches the element. The schematic presentation of the two methods of enrichment is presented in Figure 1.4. We can conclude that the enrichment in the SDM leads to fixed global unknowns, while the XFEM yields increasing global unknowns.

The SDM has gained considerable attention in the last two decades for modelling weak and strong discontinuities. Different fracture mechanisms have been developed within the SDM, including traction-opening [106], traction-sliding [107] and traction-closure [108]. The method has also shown promising results for various 2D and 3D simulations under quasi-static, dynamic, cycling and impact loading regimes, see for instance [109, 110].

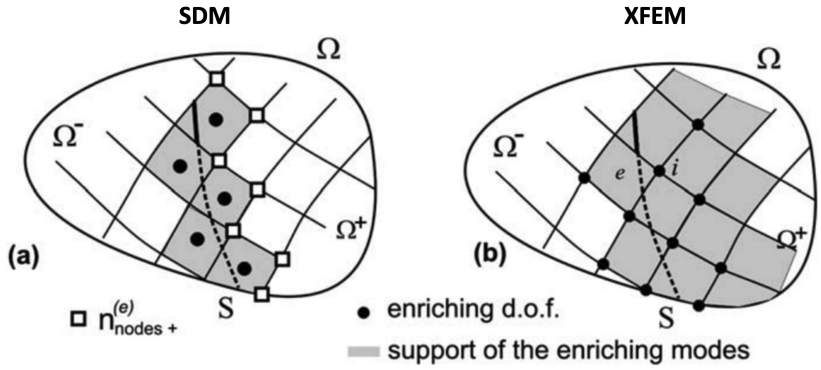

Figure 1.4: Schematic presentation of enrichment methods by the SDM (a) and the XFEM (b) reprinted from [1].

1.3.3 Cut Finite Element Method

CutFEM, as a generalisation of the XFEM, aims to handle not only arbitrary domain problems but also problems with sharp interfaces such as cracks. As discussed earlier, unfitted FEMs use enrichment techniques to apply the interface conditions for the intersected elements. Within the CutFEM enrichment, an extra element is added for the elements intersected by the crack interface, leading to a doubled degree of freedom in the cut elements. Then, the interface condition is enforced by Nitsche's method for the overlapped elements. Here, proposing an extra element for the cut element (each element representing different sides of the interface) leads to the enrichment of the solution field. This differs from the other popular unfitted FEMs, such as XFEM, where an enrichment function, such as the Heaviside step function, is typically employed for the intersected element to capture the jump (i.e. crack opening) in the field.

The CutFEM has been applied for the fracture problems in [5, 27], limited to the linear elasticity. Recently, [111] developed the CutFEM for cracks and contact problems within a large deformation regime. However, the CutFEM is still under-developed for complex interface problems. For instance, it can be developed for other fracture mechanisms, such as crack closure and sliding and weak discontinuity problems, such as strain localisation.

1.4 Phase Field Fracture Method

The computational modelling of fracture constructs a framework not only to predict the failure of cracking structures but also to explain the fracture nature in different materials. Brittle and ductile fractures are two prevalent failure mechanisms studied in computational mechanics. Ductile fractures are characterised by large plastic deformations, while in brittle fractures, little or no plastic deformations are perceived, and failure occurs rapidly [112]. In this thesis, we focus on the computational modelling of brittle fracture as a predominant failure mechanism in many heterogeneous media such as concrete, bone, or composites.

In the literature, there are two main approaches available for modelling the brittle fracture; a discrete crack approach and a smeared crack approach. In the former, the crack is interpreted as a sharp interface, and its fundamental theory was presented by Griffith [113] and Irwin [114] for linear elastic fracture mechanics (LEFM). The simulation of discrete crack initiation and propagation is carried out explicitly by several unfitted FEMs such as XFEM [24], generalised finite element method (GFEM) [115], extended isogeometric analysis (XIGA) [116], cohesive zone method (CZM) [117], and SDM [102]. In the second approach, the crack surface is treated as a diffuse entity through a scalar variable named as damage field. Here, the cracked material is considered a continuum that undergoes a strain-softening phenomenon. While discrete crack approaches provide a physically appealing way to introduce fracture in numerical simulations, the complications that arise when describing phenomena like crack branching, coalescence, and curved crack boundaries tend to favour the use of the smeared crack approaches. The main limitation of the smeared approaches is their pathological mesh size dependency, which can be alleviated by enhancing their constitutive models, for instance, with enhanced gradient terms [118].

Phase field fracture models, sometimes referred to as smeared crack/damage models, consider the initiation and evolution of crack interface through a PDE defined in terms of the phase field parameter. This scalar parameter can vary from 0 to 1, where the value 0 represents an intact region and the value 1 is a fully cracked material. The application of the phase field for fracture problems was proposed for

the first time by Francfort and Marigo [119], who developed a variational framework to approximate the classical Griffith theory of energy used in brittle fractures. Later, [120, 121, 39, 40] regularised the variational formulation of Griffith energy introducing length scales to address the mesh dependency issues and called it the phase field method.

The main advantages of the phase-field method over previous methods are its ability to capture crack initiation without the necessity of additional ad-hoc criteria and simulate complex crack propagation with branching and coalescence. The phase-field method gains these advantages by translating the discrete problem with constraints into a continuous problem that can be solved through PDEs using conventional FEM. Therefore, it requires less implementation burdensome in comparison to the other methods. For further information on various implementation techniques for the phase field method, we refer to the recent review paper by [122].

The phase field method that was initially applied for brittle fractures has subsequently been tested for other types of fractures, including ductile [123, 124], cohesive [125, 126, 127] and dynamic fractures [128, 129].

1.4.1 Phase field modelling of brittle fractures

In the context of brittle fractures, different phase field models have been developed. The well-known and widely implemented second-order phase field models are AT1 [130], AT2 [121, 40] and phase field-cohesive zone model (PF-CZM)[131]. AT1 and AT2 models use a simple quadratic degradation function that are applicable for brittle fracture, while PF-CZM employs a rational degradation function with multiple user-defined parameters to calibrate a traction-separation law. Moreover, the PF-CZM can be used for both brittle and cohesive fractures.

AT1, AT2, and PF-CZM are the well-known phase field fracture models that have been used for not only brittle fracture but also more complicated cases, such as dynamic brittle [132], anisotropic fracture [133], multiphysics fracture [134].

1.4.2 Adaptive meshing techniques for phase field fracture

A major bottleneck of the phase field method is its huge computational costs when dealing with large-scale real-world fracture problems. This is mainly due to the steep gradient of the damage profile produced by the phase field method, which naturally demands refined elements to obtain a spatially converged solution. A common approach for breaking this bottleneck is to refine mesh adaptively in the cracked regions. However, because of the progressive nature of the fracture problems, the mesh adaptivity has to be based on a sophisticated algorithm.

In the literature, there are several mesh-adaptivity techniques have been proposed for phase field fracture models. According to [135], the adaptive phase-field approaches are categorised into global and local. In the global methods, prior knowledge of the crack path is required to refine the mesh before computations, while in the local methods, the crack path is not known, and the refinement is carried out during the crack evolution [136]. Within the local methods, a damage-based error estimate algorithm is a common approach employed by [137]. However, this approach requires a non-zero damage value to initiate the mesh refinement, which is considered error-prone.

Authors in [138, 139] developed the idea of goal-oriented error estimates for mesh adaptivity [140] for phase field fracture models. They showed that the error estimate based on a local quantity of interest is an effective choice for phase field problems. [141] developed a hybrid multi-level mesh adaptivity to avoid hanging nodes by adding triangular elements to the quadrilateral mesh. However, their approach is difficult in terms of implementation and not efficient due to its huge computations. [142] constructed a local adaptive mesh refinement approach within a multiscale finite element framework.

1.5 Conclusion

In conclusion, this chapter has provided a comprehensive literature review on various unfitted FEMs, which have been developed to address the challenges of com-

plex geometry and moving interfaces. These methods aim to decouple the geometry construction from meshing, and they permit an accurate description of the solution fields while saving a large number of degrees of freedom compared to explicit approaches. The well-known unfitted FEMs for arbitrary domains include CutFEM, FCM, and cgFEM, while XFEM and SDM are examples of unfitted FEMs for embedded interfaces. The discussion of these methods highlights the importance of versatile numerical algorithms to guarantee the accuracy of the solution field and the stability and robustness of the numerical method.

Furthermore, this chapter has presented the phase field fracture method as a recently developed numerical framework for modelling fracture mechanics implicitly. This method offers several advantages over previous approaches, including the ability to capture crack initiation without the need for additional criteria and simulate complex crack propagation with branching and coalescence. Moreover, it requires less implementation burden compared to other methods. Therefore, the phase field fracture method has the potential to become a valuable tool for predicting and understanding the nature of fractures in different materials.

Overall, this chapter provides insights into various types of advanced discretisation techniques for solving PDEs corresponding complex problems in the field of computational mechanics, highlighting their strengths and limitations, and paves the way for future research in this area.

Chapter 2

Multiscale methods for heterogeneous structures

2.1 Introduction

Some materials in engineering and biology, such as composites, cements, bones and tissues, possess highly heterogeneous structures at certain length scales. While employing direct numerical simulations at a fine scale provides accurate and detailed results, they are expensive to measure and not tractable for large scale problems due to their costly, complex computations. One common solution is the multiscale simulations that enable us to take into account the essential length scales features and behaviours with affordable computational costs and without compromising on accuracy. In the multiscale methods, the microscale and macroscale models are bridged in an appropriate way to take advantage of the macroscale models' efficiency and the microscale models' high accuracy.

In problems where there is a strong coupling between different scales (wherein the behaviour at one scale depends strongly on the behaviour of the other scales), the microscale and macroscale models are typically solved simultaneously in an integrated model. Two primary classes of multiscale methods have been developed for such cases: hierarchical methods and domain decomposition methods (DDMs).

Hierarchical methods, also known as homogenisation methods, aim to incorporate the microscale behaviours into the macroscale solution across the entire domain. These methods establish a connection between the two scales at the same location within the domain. By integrating the microscale behaviours in the macroscale model all over the domain, the hierarchical approach ensures a comprehensive representation of the structure's behaviour.

On the other hand, in DDMs, the communication between the two scales is carried out with some type of handshake approach. In this approach, the heterogeneous structure is divided into two subdomains. One subdomain, typically exhibiting homogeneity, is discretised with a coarse mesh, while the remaining subdomain accurately captures the microstructure and microscale behaviour using a fine mesh.

In this chapter, our aim is to provide a comprehensive review of the prominent multiscale modelling strategies applicable to continuum mechanics and fracture processes. We begin by delving into the homogenisation technique, which forms the basis of our discussion in section 2.2. In section 2.3.1, we explore the DDM within the context of sub-modelling techniques. In the subsequent section (2.3.2), we delve into another category of DDMs known as concurrent multiscale methods. Here, we focus on an in-depth exploration of conforming (fitted) and non-conforming (unfitted) discretisation techniques within the concurrent multiscale modelling. Lastly, in section 2.4, we review multiscale methods specifically tailored for fracture problems.

2.2 Homogenisation techniques

Over the last decades, a large body of literature on homogenisation techniques has been developed to measure the effective/macroscopic properties of materials with different microstructures. The microstructure characteristics can be identified based on the type of micro inclusions, regularity of microstructure and the constitutive behaviour. [143] proposed a self-consistent approach to calculate the effective properties of the microstructures that are comprised of a matrix and spheroidal inclusions. The extensions of the self-consistent approach can be found in [144] for reinforced composites, and [145, 146] for nonlinear material behaviours. For other types of mi-

crostructures, whether regular or irregular, the effective properties can be calculated via unit cells or representative volume elements (RVEs) with appropriate boundary conditions.

Nevertheless, in the case of highly irregular microstructure, it is challenging to determine the effective properties by the RVEs. For this reason, Voigt [147] and Reuss [148] introduced a range of possible effective properties in terms of bounds. They related the effective properties with the volume fraction parameter. Their frameworks were later extended with the variational framework of Hashin and Shtrikman [149], the mean-field homogenisation framework by Mori-Tanaka [150] and interface problems by Babuska [151].

Another class of the computational homogenisation method is called FE^2 [152, 153] where the constitutive relation in the macroscale is governed point by point by solving an RVE of the microscale. It is called FE^2 because it employs the FEM to discretise both macro and micro scale boundary value problems. A fundamental assumption for the computational homogenisation methods is the separation of scales. According to this principle, the scale of microstructural fluctuation in the heterogeneous material (l_μ) needs to be smaller than the scale of the RVE (l_m) and again much smaller than the macroscopic solution field fluctuation $l_\mathcal{M}$. We show the corresponding schematic Figure in 2.1 and formulation as,

$$l_\mu < l_m \ll l_\mathcal{M}. \tag{2.1}$$

The assumption mentioned above, however, is hardly satisfied for highly nonlinear problems within the first order homogenisation. Regions of a high gradient of deformation, strain localisation and damage are the common cases where the scale separation is violated in the corresponding RVE. A common way out of this issue is to apply enhancement techniques for the first order homogenisation to capture the related softening phenomenon at the RVE level. Prevalent examples of such enhancements are introducing additional degrees of freedom or high gradient terms in weak formulation [154, 155]. Another common approach for such nonlinear problems is a second order extension of the computational homogenisation, which is based on the

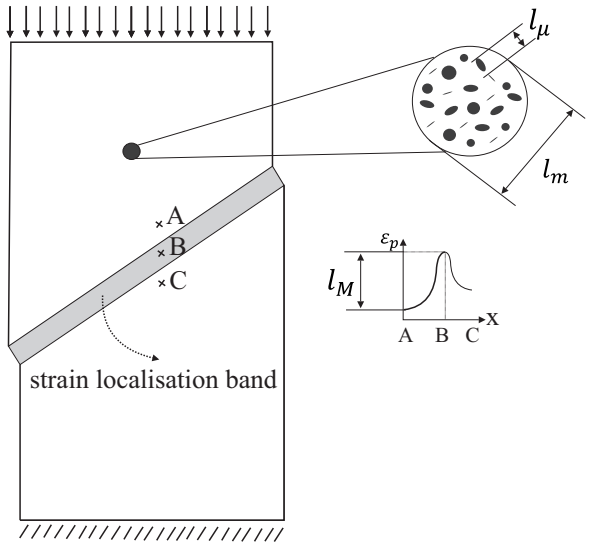

Figure 2.1: Schematic presentation of different length scales for a 2D rectangular domain under compressive load, with a strain localised band. ε_p denotes the effective plastic strain which is accumulated in the grey zone.

assumption of the gradient of the deformation gradient. This extension was initially introduced by [156] for moderate strain localised problems, then modified by [157] to account for severe strain localisation using a new formulation for the macroscale deformation gradient tensor. Since then, several techniques have been proposed based on the second order homogenisation discussing different ways for applying macroscale kinematic variable on the RVE undergoing softening, see for instance [158, 159, 160].

2.3 Domain decomposition methods

Domain decomposition methods (DDMs) tackle the modelling challenges of large structures undergoing complex phenomena in a different way [161]. The basic idea of applying DDMs for structures made of heterogeneous materials is to divide the computational domain into two subdomains: one subdomain (discretised by a coarse mesh) response is usually homogeneous and elastic, and the other subdomain (discretised by a fine mesh), the response is typically nonlinear exhibiting intense plastic deformations and/or fracturing processing.

The DDMs are not necessarily related to multiscale analysis, but they are utilised for modelling large scale problems that often own complex heterogeneous properties. For the interface between the subdomains, the condition of either displacement continuity ([162]) or traction continuity ([163]) is imposed.

In the following two categories of DDM are discussed: Sub-modelling method and concurrent multiscale method, which are mainly distinguished in terms of the method of solution of the subdomains.

2.3.1 Sub-modelling methods

In the context of DDMs, Zohdi et al. [3, 164, 2, 165] proposed a sub-modelling method for the analysis of heterogeneous structures. This approach separates the computational domain into macroscale and microscale subdomains while using the macroscale solution as a boundary condition for the microscale subdomain. This communication between scales is one-way and occurs from macroscale to microscale. The subdomain problem's boundary conditions can take the form of either displacement or traction, which are computed by solving an inexpensive auxiliary boundary value problem on a regularised microstructure.

A similar methodology, known as the LATIN method, was introduced by Ladeveze et al. [166, 167]. Operating on a non-incremental iterative strategy, the microscale solution is updated through a macroscale linear problem, and by means of interface conditions. According to the LATIN method, it is required to solve the macroscale problem over the entire domain at each iteration, along with the microscale problem in the subdomain region. The approach relies on an appropriate search direction to guarantee and expedite the global convergence.

However, when considering nonlinear constitutive behaviours and mechanisms, the application of the sub-modelling method, where macroscale behaviour is imposed as an interface condition, can introduce inaccuracies into the solution of the multiscale system. This becomes particularly challenging when dealing with the nonlinear phenomena extended to the interface, which makes the convergence of such problems a difficult task. As a consequence, many researchers over the past two

decades have focused on developing more flexible and versatile coupling techniques between the two scales. One prominent development in this field is the use of concurrent solvers. In the literature, this group of DDMs is referred to as "concurrent multiscale methods", and we will discuss them in detail in the following section.

2.3.2 Concurrent multiscale methods

According to [168], when modelling heterogeneous materials with domain decomposition methods, the main computational challenges that we encounter are

- utilising an appropriate coupling technique for linking the two sub-domains with the same or different length scales,
- performing the spatial discretisation of the interface separating the two sub-domains.

Here, we initially discuss various techniques to deal with the first challenge mentioned above using concurrent multiscale solvers. The majority of these techniques were introduced within conforming discretisation methods in their early developments. In the following, we will also discuss the challenges and available methods for discretising concurrent multiscale methods in a non-conforming fashion.

2.3.2.1 Conforming concurrent multiscale methods

Since the early development of the domain decomposition methods within sub-modelling techniques, several concurrent solvers have been invented for coupling the models with the same or different scales. In concurrent multiscale methods, we do not, however, pass information between models. Instead, we couple the fundamental quantities in the solution of each model, such as the displacement field.

The concurrent multiscale methods are categorised into two main groups based on their coupling techniques: (1) overlapping and (2) non-overlapping. In the overlapping concurrent multiscale methods, the two models with either the same or different length scales are allowed to coexist in a finite overlapping region. Figure 1b shows

a typical overlapping region in concurrent multiscale methods, which is also referred to as a *transition region*. This handshake technique shows acceptable efficiency for coupling multiple models such as continuum-continuum [16], continuum-atomistic [11, 12, 13] and continuum-molecular [14, 15], which is demonstrated to reduce the oscillatory irregular numerical solution fields over the transition region. The well-known examples of overlapping methods are the Arlequin method [17, 18], the bridging domain method [19, 20] and the works developed by [21, 22, 23].

The non-overlapping techniques, in contrast, link the two models along a sharp interface, also referred to as interface coupling [14, 169] (see Figure 1a). Therefore, here, the coupling between the two models happens along an interface rather than over an overlapped region. The s-method [9] and the mortar method [10] are popular non-overlapping coupling techniques that have demonstrated acceptable precision for coupling various models with the same and different length scales. It is worth mentioning that for both overlapping and non-overlapping approaches, the interface conditions are implemented in a framework of coupling operators, such as the Lagrange multiplier approach [6] that is extensively used in the Arlequin method [16, 170] and Nitsche's approach [7, 8], which imposes interface conditions weakly.

In contrast to the mentioned coupling techniques that are all intrusive, Gendre et al. [171] introduced a non-intrusive strategy for coupling global and local models. In this approach, the local model is superposed over the global model without modifying it. All the computations for both models are performed with standard FEMs and communicated with each other using an iterative algorithm. Recently, [172] employed second-order homogenisation kinematics to improve the iterative algorithm for highly localised problems. This approach has been successfully applied for various global/local problems with crack propagation [173, 174], localised deformations [175] as well as multiscale analysis in time and space [25, 176]. We also mention another family of non-intrusive techniques based on hierarchical enrichment algorithm using GFEM [177]. Both families are computationally efficient for large-scale problems with nonlinear phenomena occurring locally in small portions of the total domain.

2.3.2.2 Non-conforming concurrent multiscale methods

The conventional conforming discretisation methods for concurrent multiscale models impose outstanding computational costs in the pre-processing meshing stage, in particular, when

- the heterogeneous material owns complex microstructure,
- the phenomenon occurring is progressive (such as crack propagation), which requires the microscopic region (zoom) to be updated during the simulation.

These restricting factors can be easily tackled by employing suitable non-conforming discretisation techniques. In the non-conforming concurrent multiscale methods, the aim is to bypass the meshing of heterogeneous materials requiring local high resolution fine scale models in the region(s) of interest (e.g. regions with cracks, strain localisation) and low resolution coarse scale models elsewhere. Unlike conforming methods, the computational mesh is decoupled from the geometry of the multiscale model that is comprised of two types of interfaces: (1) the microstructure interface for representing the microscopic inclusions and (2) the interface between two models or micro-macro-interface.

This has several practical advantages. Firstly, the zoom interface that separates the two models is not required to be meshed or aligned with the elements' edges. This helps to locate the zooms in the desired locations easily and facilitates their relocation during the simulation, which is typical for time dependant problems. Secondly, the geometry inside the zoom regions that usually possess heterogeneous properties with complex microstructures is not meshed explicitly. These prominent advantages can be utilised for stationary and moving zooms.

The early work of non-conforming meshes or interfaces is related to a domain decomposition method proposed by [178]. In this framework, the two meshes are linked together over a non-matching interface based on the idea of employing elements with modified basis functions that satisfy the interface discontinuity conditions. Later, authors in [179] developed for the first time a non-conforming version of the non-intrusive global/local models [171]. They introduced a virtual interface framework

based on radial basis functions interpolation and localised Lagrange multiplier that demonstrated to effectively link global coarse meshes and local fine meshes in a non-conforming way. On the other hand, [180] also introduced an overlapping technique for the non-intrusive global/local models that could handle non-conforming meshes. The fine local model comprises two sub-regions in their overlapping technique. The first sub-region represents the region of interest where the local phenomenon happens, and the second sub-domain introduces an overlapping region responsible for linking the two models in a non-conforming fashion. In the case of multi-component structures, [59, 28] recently developed a non-conforming multi-mesh framework based on the CutFEM, wherein each component is allowed to possess a separate mesh. The framework allows a simultaneous overlapping of three or more meshes over a fixed background mesh.

2.4 Multiscale methods for fracture problems

A fundamental understanding of fracture and failure phenomena requires small length-scale simulations at dislocation cores and crack fronts, particularly when dealing with heterogeneous materials. The fracture behaviour in these materials is typically dominated by the underlying microscale features, including the type of microstructure constituents. Besides, computational models at the macroscale with homogenised properties often result in inaccurate predictions of the fracture behaviour, which accentuates the necessity of analysing such problems at the microscale level. Nevertheless, as discussed earlier, employing a direct numerical simulation to such heterogeneous structures with complex behaviours, including the fracture process at the microscale, is not affordable in terms of computational costs.

For instance, in the case of the phase field fracture model, these costs may be far beyond the capacity of computing machines. Compared with discrete crack models, the phase field method suffers from demanding extremely refined meshes in the regions where the crack happens to resolve high damage gradients and maintain accuracy. Also, in brittle fracturing, where discrete cracks are prevalent, we require highly refined elements to recover them through phase-field models, which creates a high

computational burden, particularly in large models with engineering applications.

In view of this situation, a common approach to tackle the computational costs of phase-field modelling is the multiscale frameworks [181, 182]. Computational homogenisation is one of the primary multiscale methods that has been applied for several fracture and damage problems in recent decades. However, due to the lack of scale separation and high deformation gradient in the cracked/damaged regions, the standard computational homogenisation is not a suitable choice. Later, [183] proposed a second-order homogenisation method to relax the scale separation assumption in the critical regions by considering a linear variation of the deformation field in the RVE. Their strategy can account for the size effects of microstructure and allow for moderate localisation of macroscale deformations [184, 185]. However, it is still inappropriate for fracture problems with high localised deformations.

The multiscale methods mentioned above are valid until two assumptions are satisfied: (1) the separation of scales is prominent, and (2) an RVE can be well-defined. Following these assumptions, an accurate homogeneous description of the microstructures is inevitable. Despite that, when the microstructure is highly heterogeneous (the microstructure heterogeneities are not homogeneous), the effective description is expected to be impacted by a coupled behaviour of the damage and the microstructure. This restrains the above methods from accurately up-scaling the information. Moreover, in the context of non-separated scales, a proper setup and interpretation of fracture phase-field models in the presence of holes and inclusions are still challenging and under-developing research topics. Recently, [186] proposed a computational homogenisation framework to provide a more in-depth interpretation of this topic. They follow the work by [187] to identify the different parameters of the homogenised phase-field model by fitting a typical force-displacement response on a heterogeneous model. In other words, they construct an inverse problem based on microscale and macroscale phase-field models and then predict the macroscopic fracture energy release rate. Their results show that the captured homogenised models can correctly reproduce the crack path and force curve.

Apart from homogenisation techniques developed for the phase-field models, the concurrent multiscale method is another family of multiscale methods that can deal

with the high computational costs and tackle the above-mentioned homogenisation barriers. The concurrent multiscale method is particularly appealing for problems where the fracture occurs in a small portion of the domain. The method divides the computational domain into macroscale and microscale subdomains. This way, the scale separation assumption will no longer be needed as the critical regions are modelled directly (explicitly) with a microscopic model. Recently, [188] proposed a concurrent multiscale method based on the s-version coupling technique for phase-field modelling of structures with complex microstructures. They solved localised phase-field problems with prior knowledge of the crack path and showed that the s-version of concurrent multiscale modelling is accurate as long as the crack is kept inside the microscale region.

2.5 Conclusion

In conclusion, this chapter provides a literature review on hierarchical multiscale modelling techniques for heterogeneous structures, with a particular focus on homogenisation techniques and concurrent multiscale methods. The homogenisation techniques discussed in this chapter aim to calculate the effective properties of materials by considering the characteristics of the microstructure. Self-consistent approaches, unit cells, and representative volume elements are commonly employed to determine these effective properties. Additionally, the computational homogenisation method is another famous technique which utilises the FEM to solve both macro and microscale boundary value problems. However, these techniques face challenges when applied to highly nonlinear problems with critical regions, such as localised deformations, plasticity, damage, and fracture. To address these issues within homogenisation methods, enhancements are proposed such as second-order extensions of computational homogenisation that has demonstrated to capture such complex softening phenomena accurately.

Conversely, concurrent multiscale methods, a popular class of domain decomposition methods, offer an alternative approach to address the modelling of complex and highly nonlinear problems. These methods partition the computational domain into

macro and microscale regions, in contrast to homogenisation techniques that aim to compute effective properties throughout the entire domain. By directly modelling (or explicitly considering) the regions experiencing local intense nonlinear mechanical phenomena, such as strain localisation, within the microscale region, concurrent multiscale methods allow the remaining regions to be modelled using less computationally expensive macroscopic models. Furthermore, these methods can adaptively update the size and location of microscale regions to capture progressive phenomena, such as fracture propagation. However, selecting the appropriate microscale region in concurrent multiscale methods can be challenging and may require robust techniques for optimisation purposes.

In summary, each category of multiscale techniques has its own advantages and drawbacks. The selection of the most suitable method should be based on the underlying mechanical mechanisms, scale of the problem, and computational capacity limitations. By understanding the strengths and limitations of these multiscale techniques, researchers and engineers can effectively address the challenges posed by heterogeneous structures and highly nonlinear phenomena in computational mechanics.

Chapter 3

Concurrent multiscale analysis with smoothed micro-macro interface

3.1 Introduction

3.1.1 Motivation

As discussed in chapter 1, classical FEM is not efficient for problems with time-dependent and complex geometries, which are prevalent features in microscale models. For such problems, we require mesh refinement and regeneration to maintain the accuracy of solutions within the FEM. Nevertheless, it still might be problematic when modelling large-scale problems due to the limited computational resources. One common remedy is to replace FEM with fictitious domain methods such as the CutFEM. As explained in chapter 1, in CutFEM, the geometry is decoupled from the finite element mesh (background mesh), which facilitates the discretisation of the problems with varying geometry and complex architectures. Then, the geometry is defined in terms of an analytical signed distance function or a given surface mesh. When dealing with large-scale structures, the signed distance function or surface mesh of the model is projected over a multiresolution background mesh to gain a balance between computational costs and accuracy. A refined mesh is adopted in the regions where the microscale phenomena occur, which is also referred to as regions of

interest (ROI) or "*zooming regions*", while a coarse mesh is used for the surrounding region.

Using an adapted background mesh, however, is not always sufficient in the context of CutFEM. In fact, a straightforward projection of the singed distance functions over the adapted background mesh can give rise to the random appearance of geometrical artefacts in the coarse mesh area. These geometrical artefacts with jagged edges can create unrealistic stress singularity. Thus, in this chapter, the main motivation is to alleviate this issue by developing a multiscale CutFEM framework.

In our multiscale framework, we replace the signed distance function description in the coarse region with a homogenised domain. Then, we introduce a smooth mixing technique to couple the fine microscale region (as the ROI) with the coarse macroscale region. We use a smoothed interface instead of a sharp interface because the arbitrary intersection of the porous domain by a sharp zooming interface can result in bad conditioning for the assembled system matrix. Our smooth coupling technique is based on a decaying weighted average function that takes the average of the two models in their smooth interface.

In the following, we first discuss the drawbacks of the CutFEM with multiresolution meshes. Subsequently, we propose our concurrent multiscale framework that has already been published in [189].

3.1.2 Introduction of the multiresolution level-set-based CutFEM

This section provides a brief illustrative two-dimensional analysis of the CutFEM formulation with a multiresolution background mesh for modelling heterogeneous structures. Here, the CutFEM formulation begins with the definitions: domain partitioning of heterogeneous structures, strong and weak form of governing equations for the linear elasticity problem and the corresponding discretised formulation.

Let Ω be the computational domain of a micro porous heterogeneous medium comprised of a matrix subdomain Ω_1 and a pore subdomain Ω_2, as illustrated in

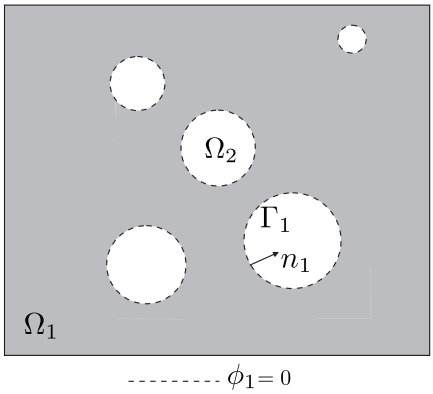

Figure 3.1: Domain partitioning for heterogeneous domain Ω partitioned into matrix subdomain Ω_1 and pore subdomain Ω_2 ($\Omega = \Omega_1 \cup \Omega_2$) with interface Γ_1

Figure 3.1 and

$$\Omega_i \subset \mathbb{R}^d, \quad i = 1, 2, \quad d = 2, \tag{3.1}$$

where the interface between Ω_1 and Ω_2 is determined by a continuous level set function ϕ_1 defined as follows

$$\phi_1(x) = \begin{cases} > 0 & x \in \Omega_2, \\ = 0 & x \in \Gamma_1, \\ < 0 & x \in \Omega_1. \end{cases} \tag{3.2}$$

The normal vector in $x \in \Gamma_1$, pointing from Ω_1 to Ω_2, is given by

$$n_1 = \frac{\nabla \phi_1(x)}{\|\nabla \phi_1(x)\|}. \tag{3.3}$$

In the previous definition, $\|x\|$ denotes the Euclidean norm $\|x\| = \sqrt{x \cdot x}$.

We consider linear elastic behaviour for Ω and look for the deformation field $u : \Omega \to \mathbb{R}^d$ which satisfies

$$\operatorname{div} \sigma + f = 0 \qquad \text{in } \Omega, \qquad \text{with } \ \sigma(u) := D : \nabla_s u \tag{3.4}$$

where f is the volume source term, $\nabla_s . = \frac{1}{2}(\nabla . + (\nabla .)^T)$ is the symmetric gradient

operator, and $D \in (\mathbb{R}^d)^4$ is the fourth order Hooke tensor of isotropic linear elastic material defined as

$$D : \nabla_s . = \lambda \mathrm{Tr}(\nabla_s .)\mathbb{I} + 2\mu \nabla_s . \tag{3.5}$$

where Tr is the tensor trace operator, $\lambda = \frac{E\nu}{(1+\nu)(1-2\nu)}$, $\mu = \frac{E}{2(1+\nu)}$ are the Lamé parameters expressed by the Young's module E and the Poisson's ratio ν.

We define the corresponding variational equation to find $u : \Omega \to \mathbb{R}^d$, $u \in H^1(\Omega)$, satisfying

$$\int_\Omega \sigma(u) : \nabla_s v \, dx = \int_\Omega f \cdot v \, dx + \int_{\partial\Omega_t} \tau \cdot v \, dx \,, \tag{3.6}$$

for all test functions $v : \Omega \to \mathbb{R}^d$, $v \in H^1_0(\Omega)$ which satisfy the homogeneous Dirichlet boundary condition $v = 0$ on Ω_u. In the previous equation, τ is the traction applied at the Neumann boundary.

We introduce triangulation $\mathcal{T}$ for the background domain Ω and then define the corresponding finite element space of continuous linear function as

$$\mathcal{Q}_h := \{w \in \mathcal{C}^0(\Omega) : w|_K \in \mathcal{P}^1(K) \,, \forall K \in \mathcal{T}\}, \tag{3.7}$$

where K represents the individual elements or triangles in the triangulation $\mathcal{T}$ and $\mathcal{P}^1(K)$ refers to the space of piecewise linear polynomial functions defined on each element K. Here, the related physical domain, Ω^h is approximated as

$$\Omega^h = \{x \in \Omega | \phi^h(x) \geq 0\}, \tag{3.8}$$

Now we can present the approximate interface Γ^h

$$\Gamma^h = \{x \in \Omega^h \,|\, \phi^h(x) = 0\}. \tag{3.9}$$

Here, we will not provide details on definitions of the fictitious domain and the stabilisation technique corresponding the CutFEM technique (for such details see the study by Burman et al. [5]). Instead, we will focus on numerical results to highlight the issue regarding the discretised Γ^h over coarse mesh regions.

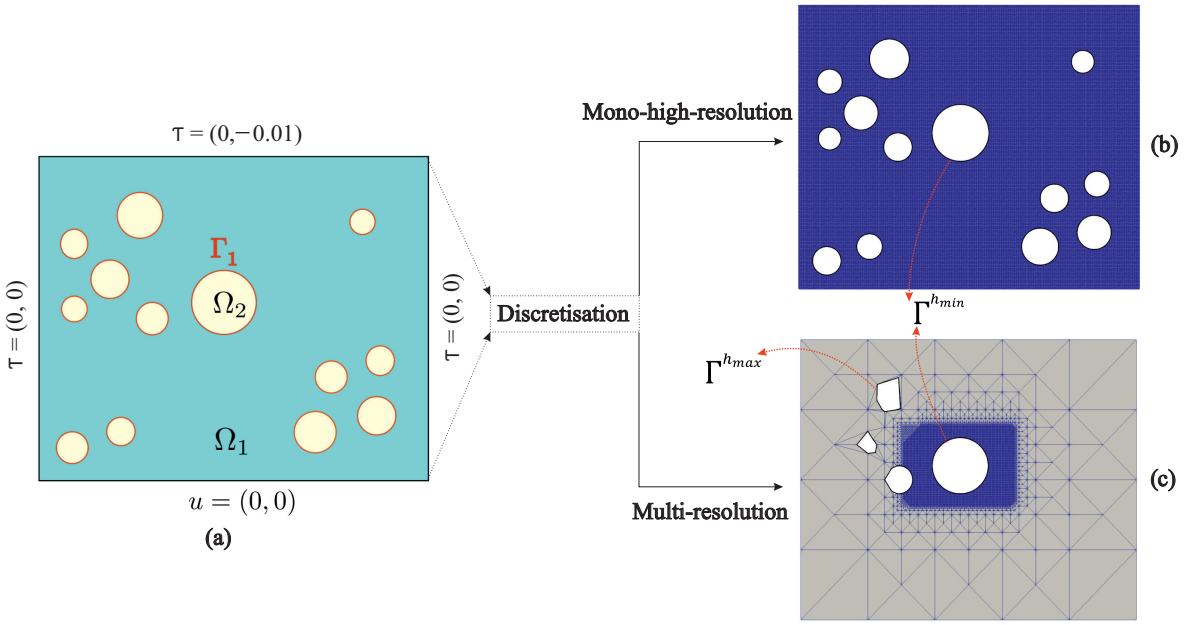

Figure 3.2: (a) Schematic depiction of 2D rectangular domain with a quasi-uniform distribution of micro pores. (b) CutFEM full high resolution discretisation ($h = h_{min} = 0.054$). (c) CutFEM multi-resolution discretisation ($h_{min}/h_{max} = 0.015$).

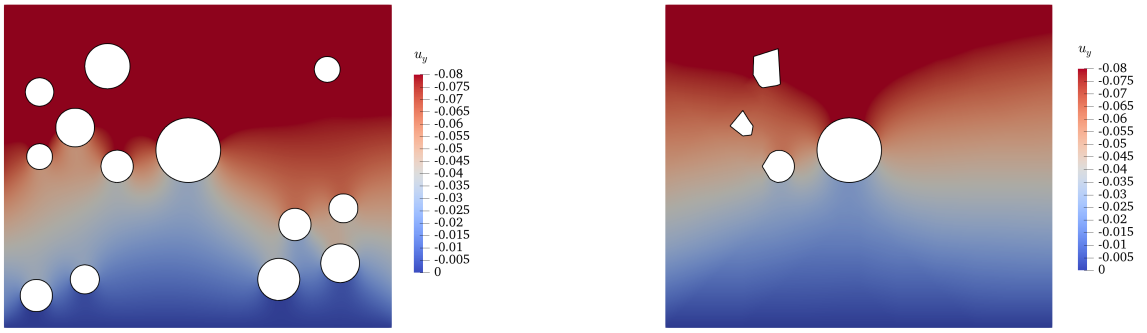

(a) (b)

Figure 3.3: Displacement component u_y for a) uniformly refined background mesh and b) adaptive background mesh.

Hence, we consider the heterogeneous structure shown in Figure 3.2a to carry out a compressive mechanical test. We restrict the displacement at the bottom edge and prescribe the traction $\tau = (0, -0.01)$ along the top edge of the domain. We assume the corresponding mechanical properties as following: $E = 1$ and $\nu = 0.3$.

Here, we define the geometry by a piecewise linear signed distance function over two types of background meshes. As depicted in Figure 3.2b,c, the first background mesh, as a reference model is uniform and fine everywhere; however, the second background mesh is fine only in regions of interest and coarse elsewhere, and the corresponding adaptive mesh refinement scale is $s = 1/4$. The zero level set function Γ^h represents the pore interfaces which intersect the background mesh arbitrarily. For both mesh configurations, the mesh size is defined as $h = h_x = h_y$ with $h_{min} = 0.005$.

We perform a mechanical compression test and consider the model with the uniform fine mesh as a reference. As shown in Figure 3.2c, using the signed distance function in the coarse domain leads to the random appearance of geometrical artefacts. The comparison of the displacement field component u_y in Figure 3.3 shows that the response in the fine mesh region of CutFEM is acceptable; however, in the coarse mesh region, the geometrical artefacts impose unrealistic additional stiffness.

3.1.3 Outline of the chapter

The remainder of the chapter is structured as follows: Section 3.2 introduces the governing equations of the concurrent multiscale method with a smoothed micro-macro interface. In this section, we first define our domain partitioning approach and then present the strong and weak forms of the equations for the concurrent multiscale model. Then, in section 3.3, we derive the discretised formulations, where the microscale model is discretised with CutFEM and the macroscale model with FEM.

In the last section (3.4), we present the numerical results of the concurrent multiscale framework. We first test the performance of the proposed smooth mixing approach in a simplified multiscale problem, with micropores distributed locally in the domain, thus, homogenisation is not essential outside of the ROI. Then, we demonstrate the efficacy and robustness of our smoothed concurrent multiscale framework for 2D and 3D elasticity problems that require a homogenised model outside of the ROI. In our 2D simulations, we use an analytical signed distance function to define the geometry. In contrast, in our 3D case study, we use a mesh surface derived from micro-CT image data to describe the geometry of a trabecular bone with a complex microstructure.

3.2 Governing equations of the concurrent multiscale method with smoothed micro-macro model

3.2.1 Domain partitioning

Let Ω be the computational domain of a micro porous heterogeneous medium comprised of a matrix subdomain Ω_1 and a pore subdomain Ω_2, as defined in the introduction (section 3.1.2) and illustrated in Figure 3.1.

In this section, we define the microscale zoom region $\widehat{\Omega}_z$ for our multiscale analysis

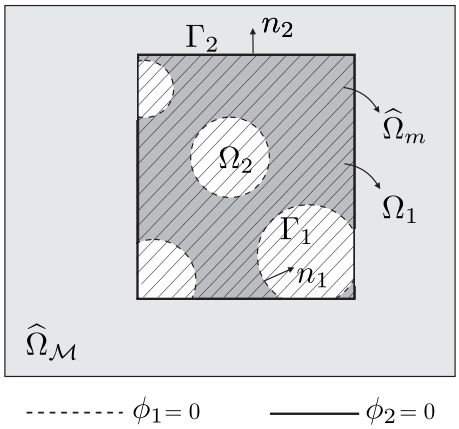

Figure 3.4: Domain partitioning for the smoothed concurrent multiscale method: computational domain Ω is partitioned into macro subdomain $\widehat{\Omega}_{\mathcal{M}}$ and micro subdomain $\widehat{\Omega}_z$ ($\Omega = \widehat{\Omega}_{\mathcal{M}} \cup \widehat{\Omega}_z$). Here, $\widehat{\Omega}_m = \widehat{\Omega}_z \setminus \Omega_2$ denotes the porous micro domain.

by a continuous level set function ϕ_2 given by

$$\phi_2(x) = \begin{cases} > 0 & x \in \widehat{\Omega}_{\mathcal{M}}, \\ = 0 & x \in \Gamma_2, \\ < 0 & x \in \widehat{\Omega}_z, \end{cases} \tag{3.10}$$

whose zero isoline defines the boundary of the zoom. The macro domain, denoted by $\widehat{\Omega}_{\mathcal{M}}$, is the domain outside of the zoom. For an illustration see Figure 3.4, with $\widehat{\Omega}_z$ shown as the shaded area. Furthermore, the normal vector on the interface Γ_2 pointing from $\widehat{\Omega}_z$ to $\widehat{\Omega}_{\mathcal{M}}$ is given by

$$n_2 = \frac{\nabla \phi_2(x)}{\|\nabla \phi_2(x)\|}. \tag{3.11}$$

Furthermore, let $\widehat{\Omega}_m = \widehat{\Omega}_z \setminus \Omega_2 = \widehat{\Omega}_z \cap \Omega_1$, denote the microscale region without the pores. The porous microscale domain can be expressed by a combination of the two level set functions

$$\widehat{\Omega}_m = \{x \in \Omega : \phi_1(x) < 0 \text{ and } \phi_2(x) < 0\}. \tag{3.12}$$

3.2.2 The boundary-value problem

Let us consider linear elastic behaviour for the macro domain $\widehat{\Omega}_{\mathcal{M}}$ and the porous micro domain $\widehat{\Omega}_m$. In our multi-model, we are seeking the deformation field $u : \widehat{\Omega}_{\mathcal{M}} \times \widehat{\Omega}_m \to \mathbb{R}^d \times \mathbb{R}^d$ which satisfies

$$\operatorname{div} \sigma_{\mathcal{M}} + f = 0 \qquad \text{in } \widehat{\Omega}_{\mathcal{M}}, \tag{3.13a}$$

$$\operatorname{div} \sigma_m + f = 0 \qquad \text{in } \widehat{\Omega}_m, \tag{3.13b}$$

where

$$\sigma_{\mathcal{M}}(u) := D_{\mathcal{M}} : \nabla_s u \tag{3.14a}$$

$$\sigma_m(u) := D_m : \nabla_s u \tag{3.14b}$$

The boundary of the background domain Ω is partitioned into $\partial\Omega_u$ and $\partial\Omega_t$ ($\partial\Omega = \partial\Omega_t \cup \partial\Omega_u$), where $\partial\Omega_u$ is the part where the body is clamped and $\partial\Omega_t$ is the part where traction t is applied with $\partial\Omega_t \cap \partial\Omega_u = \emptyset$.

In the expressions above, f is the volume source term, $\nabla_s . = \frac{1}{2}(\nabla . + (\nabla .)^T)$ is the symmetric gradient operator, and $D \in (\mathbb{R}^d)^4$ is the fourth order Hooke tensor of isotropic linear elastic material defined previously in equation 3.5.

On the zooming interface, Γ_2, between micro and macro model, the traction is required to satisfy the following coupling condition

$$\sigma_m \cdot n_2 = \sigma_{\mathcal{M}} \cdot n_2 \qquad \text{on} \qquad \Gamma_2. \tag{3.15}$$

Integrating governing equations (3.13a)-(3.13b) over the given domains, i.e. macro domain $\widehat{\Omega}_{\mathcal{M}}$ and micro domain $\widehat{\Omega}_m$, the weak form of the multiscale elasticity problem is given as follows. We seek a displacement field $u : \widehat{\Omega}_{\mathcal{M}} \times \widehat{\Omega}_m \to \mathbb{R}^d \times \mathbb{R}^d$,

$u \in H^1(\Omega_{\mathcal{M}}) \times H^1(\Omega_m)$, satisfying

$$\int_{\widehat{\Omega}_{\mathcal{M}}} \sigma_{\mathcal{M}}(u) : \nabla_s v \, dx + \int_{\widehat{\Omega}_m} \sigma_m(u) : \nabla_s v \, dx = \int_{\widehat{\Omega}_{\mathcal{M}}} f \cdot v \, dx + \int_{\widehat{\Omega}_m} f \cdot v \, dx + \int_{\partial\Omega_t} \tau \cdot v \, dx \,, \tag{3.16}$$

for all test functions $v : \widehat{\Omega}_{\mathcal{M}} \times \widehat{\Omega}_m \to \mathbb{R}^d \times \mathbb{R}^d$, $v \in H^1_0(\Omega_{\mathcal{M}}) \times H^1_0(\Omega_m)$ which satisfy the homogeneous Dirichlet boundary condition

$$v = 0 \qquad \text{on} \quad \partial\Omega_u. \tag{3.17}$$

3.3 Discretisation for smoothed concurrent multiscale problems

In this Section, we introduce a CutFEM-based approximation scheme of the multiscale elasticity problem proposed in Section 3.2 using a novel smoothed cut finite element approach. The arbitrary intersection of the porous domain by the sharp zooming interface, Γ_2, can result in bad conditioning for the assembled system matrix. To alleviate this problem, we introduce a mixing strategy between the macroscale and microscale regions. In this smoothed approach, we create an overlap between the two models. We refer to the overlapping domain as "*transition domain*", as highlighted in Figure 3.5a in yellow.

For mixing purposes, we extend the macro and micro domains defined in the previous Section into the transition region. First we extend the macro domain by $\Omega_{\mathcal{M}} := \widehat{\Omega}_{\mathcal{M}} \cup \Omega_T$. Then we extend the micro domain inside zoom to $\Omega_m := \widehat{\Omega}_m \cup \Omega_T$, where Ω_T is the transition domain. In this framework, $\Omega_{\mathcal{M}}$ and Ω_m are overlapping in the transition domain. The transition domain is determined by the level set function ϕ_2, which is the signed distance function to Γ_2. We set the width of the transition region to 2ϵ, which is given by the signed distance from $-\epsilon$ to $+\epsilon$. We define a smooth weight function α for the mixing, as shown in Figure 3.5b, and express it in

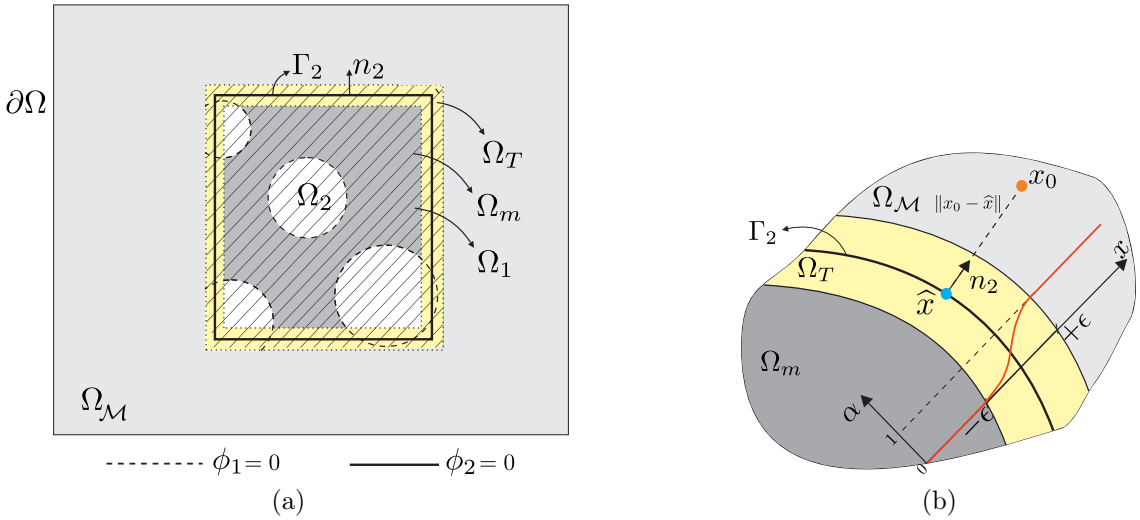

Figure 3.5: Transition domain in the smoothed multiscale method (a) and the distance dependent weight function, α, in the transition domain (b).

terms of ϕ_2 by

$$\alpha(x) = \begin{cases} 0 & \text{if } \phi_2(x) \leq -\epsilon, \\ \mathcal{S} & \text{if } -\epsilon < \phi_2(x) < \epsilon, \\ 1 & \text{if } \phi_2(x) \geq \epsilon. \end{cases} \tag{3.18}$$

In the previous expression, $\mathcal{S}$ is a smooth function varying from 0 to 1 inside the transition zone, and as shown in Figure 3.5b, $-\epsilon$ and $+\epsilon$ are the lower and upper bounds of Ω_T inside micro and macro domains, respectively. We will blend and mix the macro and micro models using the weights α and $1 - \alpha$.

3.3.1 Multiscale finite element space

Here we discretise the weak form (3.16) of the multiscale model, which locally modifies a global problem by using only one mesh, unlike other similar methods such as the Arlequin method [16] and multi-mesh CutFEM [60] that superimpose a high resolution mesh onto a coarse background mesh. In our framework, we introduce triangulation $\mathcal{T}$ for the background domain Ω and then define the corresponding

finite element space of continuous linear function as

$$\mathcal{Q}_h := \{w \in \mathcal{C}^0(\Omega) : w|_K \in \mathcal{P}^1(K)\,, \forall K \in \mathcal{T}\}, \tag{3.19}$$

where the corresponding smoothed multiscale model physical domains, $\Omega^h_{\mathcal{M}}$ and Ω^h_m are approximated as

$$\Omega^h_{\mathcal{M}} = \{x \in \Omega | \phi^h_2(x) \geq -\epsilon\}, \tag{3.20}$$

$$\Omega^h_m = \{x \in \Omega | \phi^h_1(x) \leq 0 \;\text{ and }\; \phi^h_2(x) \leq \epsilon\}. \tag{3.21}$$

Furthermore, we approximate the transition domain Ω^h_T as

$$\Omega^h_T = \{x \in \Omega | -\epsilon \leq \phi^h_2(x) \leq \epsilon\}. \tag{3.22}$$

In (3.20) and (3.21), $\phi^h_1(x) \in \mathcal{Q}_h$ is the piecewise linear approximation of the level set function ϕ_1 and $\phi^h_2(x) \in \mathcal{Q}_h$ is the piecewise linear approximation of level set function ϕ_2. By using these level set functions, we define the position of the microscale features and pores over a single fixed mesh arbitrarily (in a nonconforming manner). Now we can present the approximate interface Γ^h_1

$$\Gamma^h_1 = \{x \in \Omega^h_{\mathcal{M}} \,|\, \phi^h_1(x) = 0\}. \tag{3.23}$$

The pores with arbitrary geometries can have non-zero intersection with either macro or micro domains, where all the elements of $\mathcal{T}$ intersected by Γ^h_1 will be grouped in set

$$T^h_1 := \{K \in \mathcal{T} : K \cap \Gamma^h_1 \neq \emptyset\}, \tag{3.24}$$

where the corresponding domain is defined as $T^H_1 = \bigcup_{K \in T^h_1} K$.
Furthermore, let T^H_p denote the set of all elements, which are fully inside the pores, i.e. $\phi^h_1 > 0$ in all vertices of the element.

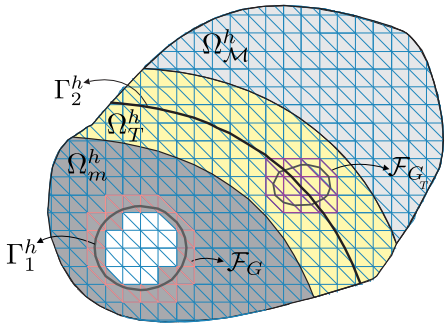

Figure 3.6: Schematic presentation of the discretised domain for the smoothed multiscale method.

3.3.2 Fictitious domain

First, we define a set of all elements in the background mesh $\mathcal{T}$ which have a non-zero intersection with $\Omega^h_{\mathcal{M}}$ or Ω^h_m

$$\mathcal{T}_h := \{K \in \mathcal{T} : K \cap (\Omega^h_{\mathcal{M}} \cup \Omega^h_m) \neq \emptyset\}. \tag{3.25}$$

Note that, this fictitious domain mesh consists of all elements in the background mesh except for the elements fully inside the pores outside of the transition region (elements shown in white in Figure 3.6). The domain associated with this set of elements is called fictitious domain and is denoted by $\Omega_{\mathcal{T}} := \bigcup_{K \in (\Omega^h_{\mathcal{M}} \cup \Omega^h_m)} K$.

Notably, all elements inside the pores in the transition region are contained in the fictitious domain mesh. These elements are not integrated over in the micro domain and therefore yield a zero contribution in the system matrix. Therefore, these elements rely mainly on the stiffness of the macro domain. However, if almost the full weight is on the micro domain, i.e. $\alpha \approx 0$, in the transition region there is very little contribution from the macro domain inside the pores and this yields ill-conditioning.

In addition to this source of ill-conditioning, we can obtain ill-conditioned matrix entries through the integration of elements which lie almost entirely in the pores in the micro region and therefore contain very little material from the micro domain.

We address these two sources of ill-conditioning by introducing two ghost penalty regularisation terms. The first one is used for the elements intersected by Γ^h_1 in the

microscale region Ω_m^h, and is applied to the elements edges (shown in red in Figure 3.6) given by

$$\mathcal{F}_G := \{F = K \cap K' : K \in \mathcal{T}_h \text{ and } K' \in \mathcal{T}_h,\, F \cap T_1^H \neq \emptyset\}. \tag{3.26}$$

The second ghost penalty regularisation term is applied to the edges of elements in the transition region Ω_T^h that are intersected by Γ_1^h or are inside the pores. These ghost penalty terms extend the solution of the micro domain into the pores. It gives the elements in the pores a stiffness, which alleviates ill-conditioning, while maintaining the consistency and accuracy of the solution (i.e. terms vanish with optimal rate with mesh refinement and continuity of the solution). The corresponding edges are shown schematically in Figure 3.6 in purple and are defined as

$$\mathcal{F}_{G_T} := \{F = K \cap K' : K \in \mathcal{T}_h \text{ and } K' \in \mathcal{T}_h,\, F \cap (T_1^H \cup T_2^H) \neq \emptyset\}, \tag{3.27}$$

where T_2^H is the domain related to the set of all elements of $\mathcal{T}$ intersected by pores in the transition domain defined as $T_2^H = \bigcup_{K \in T_2^h} K$, where the set of elements T_2^h is given by,

$$T_2^h := \{K \in \mathcal{T} : K \cap \Omega_T^h \neq \emptyset \text{ and } (K \in T_1^H \text{ or } K \in T_p^H)\}. \tag{3.28}$$

In this contribution, since we use one adapted background mesh for the multiscale problem, the displacement field is continuous throughout the whole domain. For its discretistion, we choose the vector-valued continuous piecewise linear space

$$\mathcal{U}^h := \{u \in \mathcal{C}^0(\Omega_\mathcal{T}) : u|_K \in \mathcal{P}^{s,1}(K) \;\; \forall K \in \mathcal{T}_h\}, \tag{3.29}$$

where s denotes the spatial dimension, $s = 2, 3$.

3.3.3 Stabilised multiscale formulation

The mixed finite element formulation for the proposed multiscale method is the following: find $u^h \in \mathcal{U}^h$, such that

$$a_{\mathcal{M}}(u^h, v^h) + a_m(u^h, v^h) = l_{\mathcal{M}}(v^h) + l_m(v^h) \tag{3.30}$$

for any $v^h \in \mathcal{U}^h$ satisfying homogeneous Dirichlet boundary conditions. The bilinear form $a_{\mathcal{M}}$ and linear form $l_{\mathcal{M}}$ of the macro model are given by

$$a_{\mathcal{M}}(u^h, v^h) = \int_{\Omega^h_{\mathcal{M}}} \alpha^h D_{\mathcal{M}} \nabla_s u^h \nabla_s v^h \; dx, \tag{3.31}$$

$$l_{\mathcal{M}}(v^h) = \int_{\Omega^h_{\mathcal{M}}} \alpha^h f \cdot v^h \; dx + \int_{\partial\Omega^h_t} \alpha^h \tau \cdot v^h \, ds. \tag{3.32}$$

where α^h is the discretised form of weight function α. In the previous problem statement, the regularised bilinear form a_m is defined for the micro scale model as

$$\begin{aligned} a_m(u^h, v^h) = \int_{\Omega^h_m} (1-\alpha^h) D_m \nabla_s u^h \nabla_s v^h \; dx + \\ \sum_{F \in \mathcal{F}_G} \left(\int_F \frac{(1-\alpha^h)\beta h}{E_m} [\![D_m \nabla_s u^h]\!] [\![D_m \nabla_s v^h]\!] \; dS \right). \end{aligned} \tag{3.33}$$

Here, the second term, called ghost-penalty, ensures a uniformly bounded condition number for the system matrix and $[\![x]\!]$ denotes the normal jump of quantity x over the facet F, and β denotes the Ghost Penalty stabilization parameter that needs to be large enough to guarantee the coerciveness of bilinear form a_m [5, 7] on the fictitious domain. The linear form of the microscale model is given by

$$l_m(v^h) = \int_{\Omega^h_m} (1-\alpha^h) f \cdot v^h \; dx. \tag{3.34}$$

3.4 Numerical results

This section has two objectives: (1) to verify the applicability of the proposed smooth mixing framework, (2) to demonstrate the capability of the proposed smoothed concurrent multiscale framework for 2D and 3D linear elasticity problems. For the first objective, we choose a heterogeneous structure with a local distribution of micro pores, which is a simplified case due to it's homogeneous microstructure outside of the ROI. For the second objective, we adopt more complex heterogeneous structures (2D and 3D) where due to the distribution of micro pore over the entire domain, homogenisation outside of the ROI is required to improve the accuracy of results.

3.4.1 Smooth mixing approach adopted for a 2D locally porous medium

Here, we investigate the performance of the proposed smooth mixing approach in a 2D locally porous medium, shown schematically in Figure 3.7. This structure is a simple case for multiscale modelling, as homogenisation is not essential in the coarse domain due to the local distribution of micro pores.

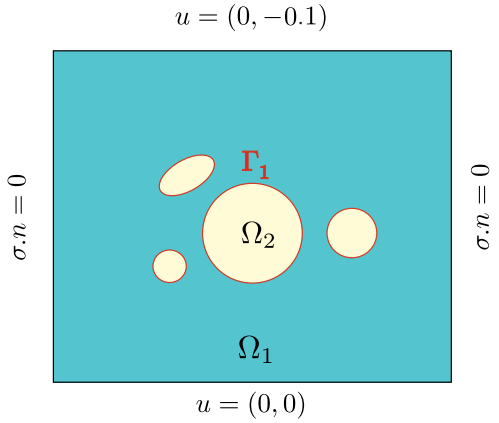

Figure 3.7: Schematic presentation of 2D rectangular domain with locally distributed pores.

We define the rectangular domain as $\Omega = [0, 12] \times [0, 10]$, comprised of matrix domain $\Omega_1 = \Omega \backslash \Omega_2$ and pore domain Ω_2. We block the displacement at the bottom

edge and insert displacement $u = (0, -0.1)$ along the top edge of the domain. Then, we set the macro and microscale mechanical properties to $E_{\mathcal{M}} = E_m = 1$ and $\nu_{\mathcal{M}} = \nu_m = 0.3$.

We test three structured background meshes consisting of one uniform and two adaptively refined meshes generated independently of the pore and zoom interfaces. We employ linear Langrangian elements, with a uniform background mesh size $h = h_x = h_y$ and the regularisation parameter set to $\beta = 0.005$. The corresponding discretisations of the physical domain Ω_1 are shown in Figure 3.8. The zero level set functions of Γ_1^h (shown as black lines) and Γ_2^h (shown as red line) represent the micro pore and the zooming regions, respectively. The corresponding discretised domains in Figure 3.8 show the arbitrary intersection of the interfaces with the elements, where the zooming interface determines the middle of the transition region Ω_T and the mesh is refined inside the zoom.

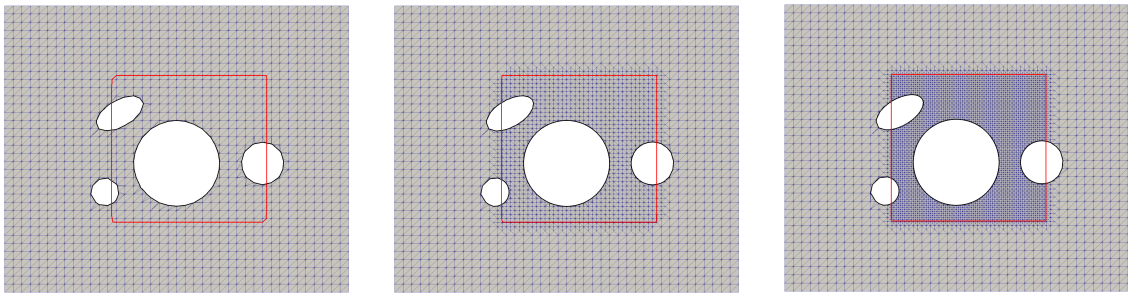

(a) (b) (c)

Figure 3.8: Computational mesh for the physical domain of the 2D model with locally distributed pores a) uniform meshing, b) adaptive meshing type-1, c) adaptive meshing type-2.

In this thesis, we choose the following smooth weight function to mix the two models inside transition region Ω_T,

$$\mathcal{S} = \frac{1}{2}(1 + \sin(\frac{\pi}{2\epsilon}\phi(x))). \tag{3.35}$$

Here, the function $\mathcal{S}$ needs to possess infinite differentiability (C^∞) when attempting to utilise small blending lengths. The reason for this requirement is that a higher degree of smoothness ensures a more gradual transition between the mul-

tiscale and homogenised regions, minimising any abrupt changes or artifacts in the solution. While functions with lower smoothness properties, such as C^1 or C^2, may be sufficient in certain cases, employing a C^∞ function offers greater flexibility and control over the blending process. It allows for a smoother transition, resulting in improved accuracy and reduced numerical errors associated with the blending effects.

Figure 3.9 illustrates how the scalar function α_h is distributed in the discretised physical domain with different mixing lengths. Note that our multiscale mixing approach operates over a single mesh, and its mixing length is defined in a mesh-independent manner. The displacement field component u_y for two smooth mixing lengths $2\epsilon = 0.1, 1$ and the finest adaptive mesh with $h_{min} = 0.2$ are shown in Figure 3.10c, d. We choose standard FEM and unfitted CutFEM as reference models and present the corresponding u_y in Figure 3.10a, b. As expected, we find that our CutFEM displacement field converges to the FEM displacement field, verifying our single-scale unfitted method. For the smoothed multiscale model, u_y inside the zoom is similar to the corresponding references and exhibits smooth behaviour in the transition domain Ω_T.

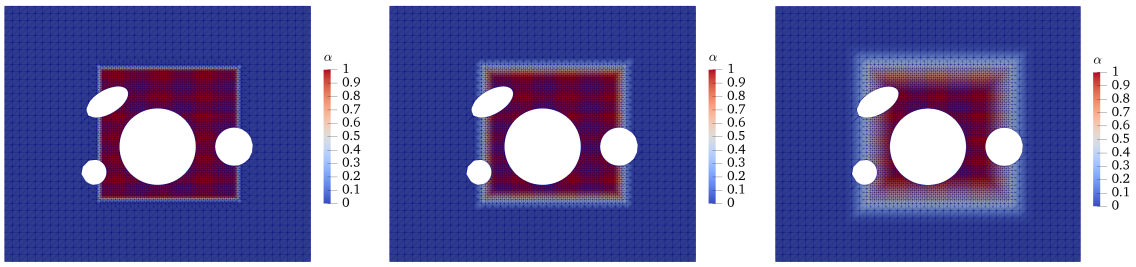

Figure 3.9: Smoothing weight function α contour over finest adaptive mesh, a) $\epsilon = 0.1$, b) $\epsilon = 0.4$ and c) $\epsilon = 1$.

The energy distribution inside Ω_T is the average of the FEM macroscale and the CutFEM microscale model. Next, we will investigate how the mixing approach via the weight function (3.35) impacts the stress field in the physical and the fictitious

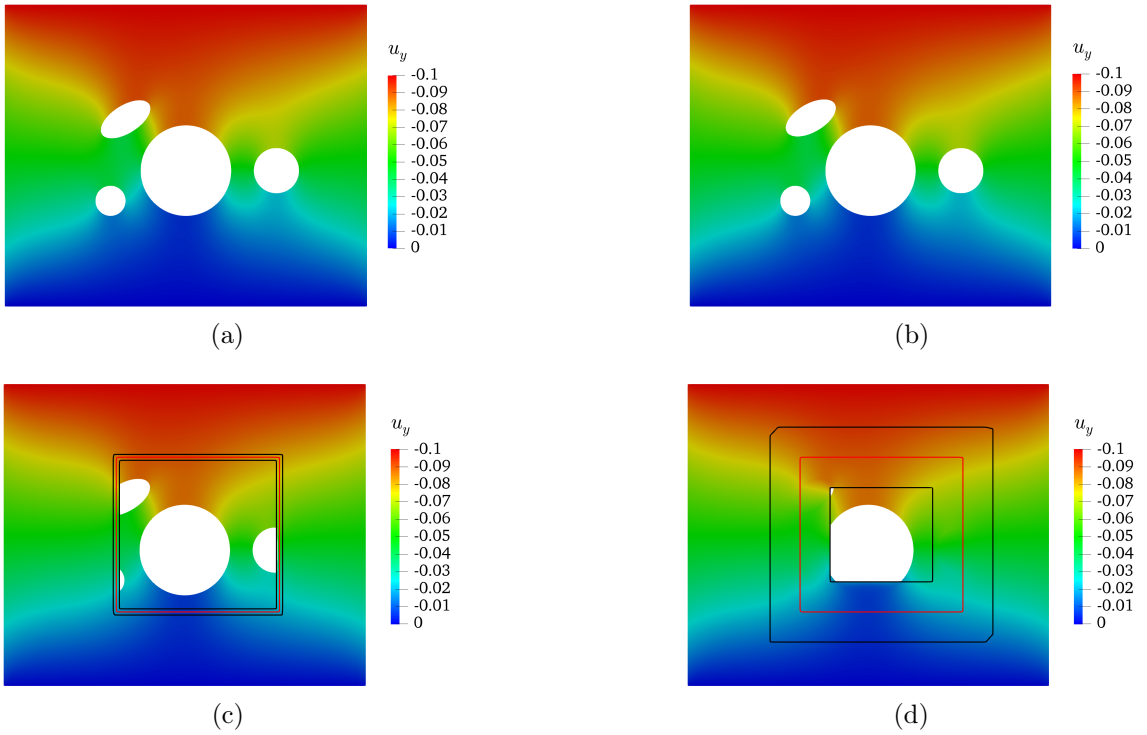

Figure 3.10: Displacement component u_y contours for different methods: a) FEM, b) CutFEM, c) smoothed multiscale model with $2\epsilon = 0.1$, d) smoothed multiscale model with $2\epsilon = 1$.

domains. The stress field is given by

$$\sigma_{\text{mix}}(x) = \begin{cases} \sigma_m & \text{if } x \text{ in } \Omega_m \backslash \Omega_T, \\ \sigma_{\mathcal{M}} & \text{if } x \text{ in } \Omega_{\mathcal{M}} \backslash \Omega_T, \\ (1 - \alpha^h(x))\sigma_m + \alpha^h(x)\sigma_{\mathcal{M}} & \text{if } x \text{ in } \Omega_T. \end{cases} \tag{3.36}$$

As shown in Figure 3.11a,b, the stress component σ_{yy} in CutFEM converges to its FEM counterpart. We compute σ_{mix} given in (3.36) for two smoothing lengths over the physical and fictitious domains in Figure 3.11c-3.11f. Our results show that σ_{mix} in Ω_T is smooth and without oscillations.

For the purpose of quantitative comparison, we evaluate the σ_{yy} at two distinct points within the zoom region and compare them to the corresponding values obtained from the reference model. The first point, denoted as A and located at

coordinates (6,6.4), resides inside the zoom area and aligns with the larger circular pore. The second point, referred to as B and positioned at coordinates (7.9,4.5), is also within the zoom region and lies exactly between the larger and smaller circular pores.

At point A, the values of the mixed stress component, $\sigma_{mix,yy}$, for the smoothed multiscale model with 2ϵ set to 0.1 and 1, are -2.8×10^{-4} and -4.0×10^{-4} respectively. In comparison, the corresponding value of σ_{yy} for the full FEM (serving as the reference model) is -3.05×10^{-4}. The comparison of these results reveals a more satisfactory level of agreement for the sharp smoothing length ($2\epsilon = 0.1$), while the wider smoothing length results are adversely affected by the blending effects of the homogenized model. A similar quantitative comparison is performed for point B. The computed $\sigma_{mix,yy}$ values, with 2ϵ equal to 0.1 and 1, are -0.0245 and -0.0232 respectively, with the corresponding reference value being -0.0261. The results at point B exhibit a satisfactory agreement for both smoothing lengths. The higher errors observed for 2ϵ in both cases can be attributed to the smoothing effects within the transition region. Overall, the quantitative comparisons yield satisfactory results, confirming the accuracy of our approach in capturing the desired response.

To enhance the stability of our multiscale framework, in the microscale model, we regularise the elements inside the porous domain in addition to the intersected elements by Γ_1^h. Then we compute the condition number of the multiscale system matrix to investigate the stability by using SLEPc [190] which finds the ratio of the maximum to the minimum eigenvalue of the system matrix (i.e. $\lambda_{max}/\lambda_{min}$). We use a sequence of uniform and adaptive meshes with different mixing lengths and then compare them with the CutFEM reference model. In Figure 3.12a, we find that the behaviour of our smoothed approach with different mixing lengths is well conditioned and similar to the standard CutFEM approach. In Figure 3.12b, we investigate the impact of extending the ghost-penalty regularisation to the inside of the pores (in addition to the cut elements by the pore interfaces) on the condition number of the multiscale system matrix. As expected, this technique improves the condition number effectively. Also, we find that the corresponding behaviour with respect to mesh refinement for our smoothed approach is proportional to h^{-2} for

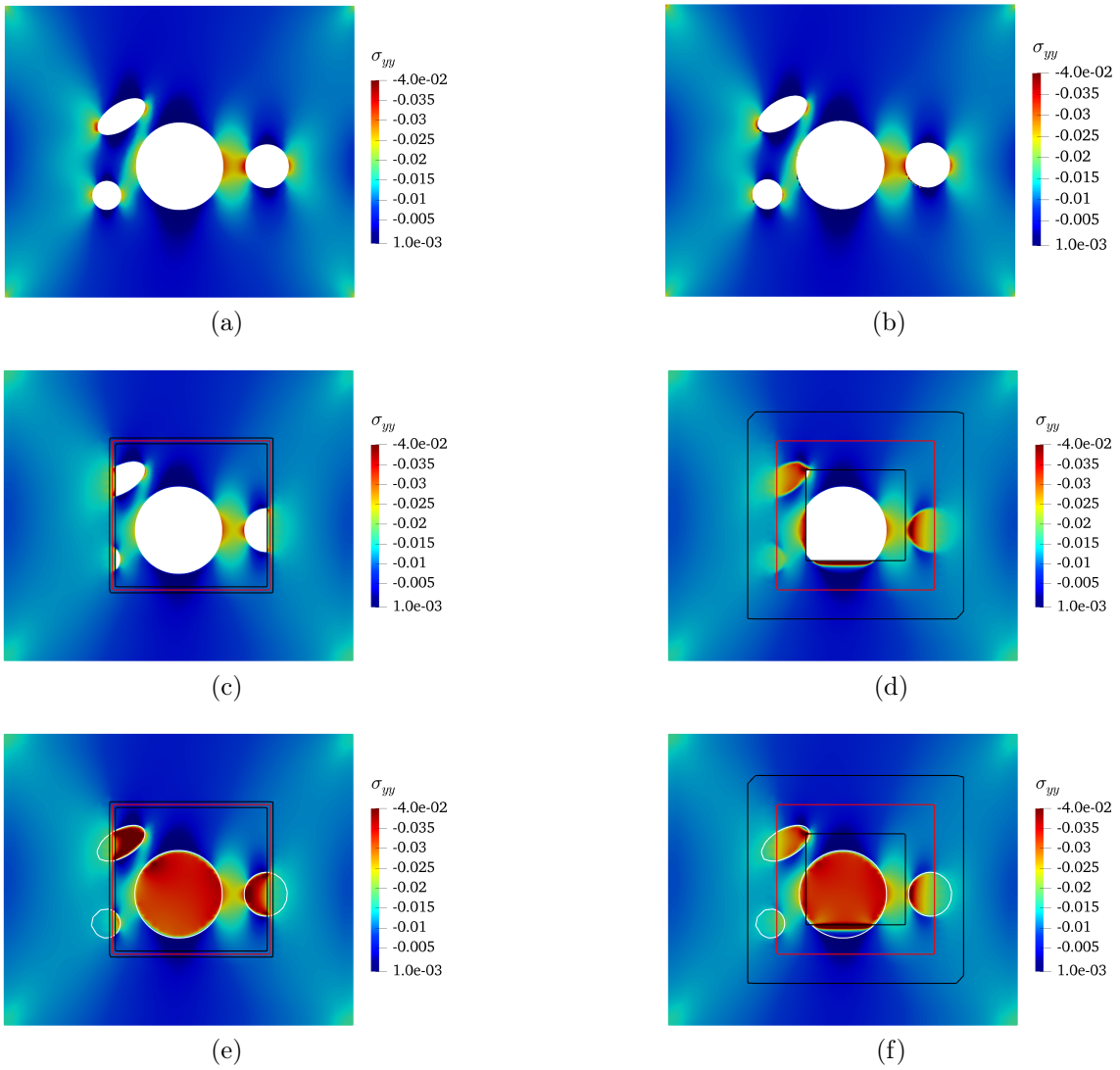

Figure 3.11: Stress component σ_{yy} contours, a) FEM model, b) CutFEM model, c) smoothed multiscale model in physical domain with $2\epsilon = 0.1$, d) smoothed multiscale model in physical domain with $2\epsilon = 1$, e) smoothed multiscale model in fictitious domain with $2\epsilon = 0.1$, f) smoothed multiscale model in fictitious domain with $2\epsilon = 1$.

both regularisation approaches, which are very close to the "pure" CutFEM results.

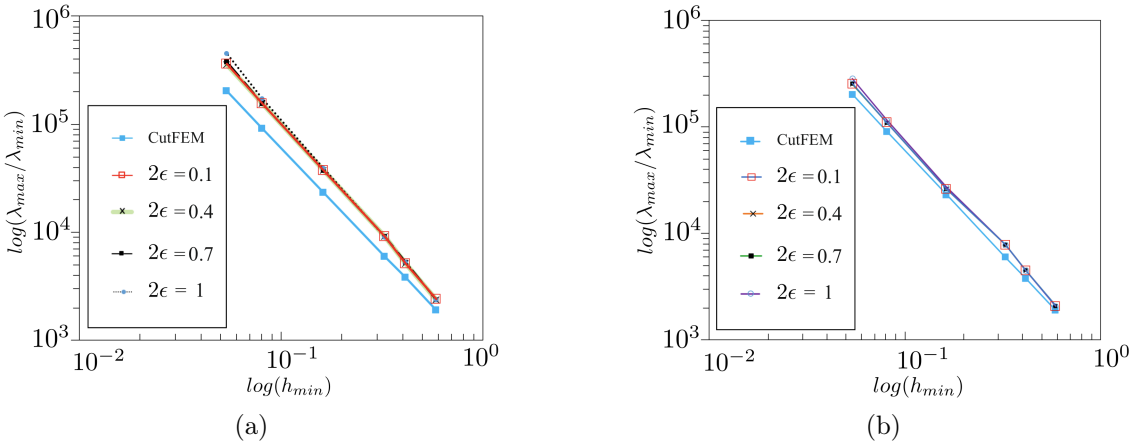

Figure 3.12: The condition number of the system matrix versus mesh size, for different mixing lengths: a) ghost penalty regularisation is applied to cut elements only, b) ghost penalty regularisation is applied to every element inside the porous domain in addition to cut elements. In both cases, the regularisation parameter is chosen as $\beta = 0.005$.

3.4.2 The smoothed multiscale method for a 2D quasi-uniform porous medium

In this section, we consider the quasi-uniform porous domain given in Figure 3.2 for our smoothed multiscale analysis. As discussed in section 4.1, structures with uniform heterogeneity require homogenisation in the coarse domain to avoid geometrical artefacts which yield unrealistic stiffness and stress singularities. Hence, here, we replace the signed distance function in the coarse domain with a homogenised domain and use the smooth mixing approach to couple the fine and coarse scale domains.

In our smoothed multiscale framework, we construct the homogenised model by using the modified Mori-Tanaka technique (MMTT) approach [191] to reproduce the effects of micropores in the homogenised macro model. Employing the MMTT homogenisation approach for $\Omega_{\mathcal{M}}$ with n circular pores of different radii, the effective Young's modulus will be computed as follows.

$$E^i_{\mathcal{M}} = (1 - \bar{\phi}_i) E^{i-1}_{\mathcal{M}} (\bar{\phi}_i L_i + (1 - \bar{\phi}_i) I)^{-1}, \quad i = 1, ..., n, \tag{3.37}$$

where $E^i_{\mathcal{M}}$ and $E^{i-1}_{\mathcal{M}}$ are the homogenised Young's modulus with inclusion of i^{th} and $(i-1)^{th}$ circular pores, respectively, and $\bar{\phi}_i$ is the i^{th} porosity parameter defined as

$$\bar{\phi}_i = V^i_v / V_t, \tag{3.38}$$

where V^i_v is the void volume with i number of pores and V_t is the total volume. L_i is the Eshelby parameter given for circular inclusions in [192]. To calculate the effective elastic modulus of a domain with n pores, we add the inclusions one by one, and in each step number i; we update Equation 3.37. For more details regarding the MMTT, see [191].

3.4.2.1 The smoothed multiscale with one arbitrary zoom

Here, we use the smoothed multiscale framework with one zoom and compare it with the equivalent adaptive CutFEM approach discussed in Section 4.1. The zooming interface is projected over the background mesh and shown with a red line in Figure 3.13. The material properties and boundary conditions are the same as in the adaptive CutFEM model from Section 4.1. To compute the homogenised material properties, we consider the pores in the entire domain Ω. We use Equation 3.37 for this purpose and then calculate the corresponding effective Young's modulus as $E_{\mathcal{M}} = 0.78$.

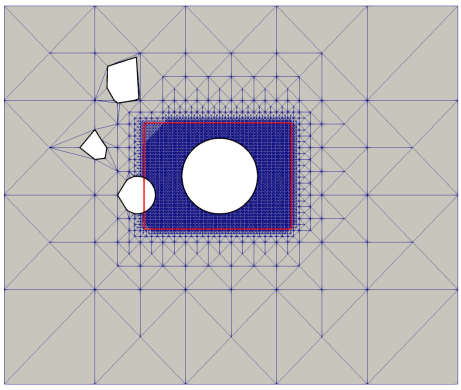

Figure 3.13: Background mesh with projected pores and zooming interfaces of the smoothed multiscale method.

We test two length sizes for the transition region, $2\epsilon = 0.2, 0.8$. The displacement field component u_y for both ϵ is shown in Figure 3.14. When compared to the full microscale model as a reference, shown in Figure 3.3a, the smoothed multiscale method with homogenisation is much closer to the reference solution in comparison to the adaptive CutFEM approach, shown in Figure 3.3b. Therefore, using homogenised models in the coarse domains is necessary when the signed distance functions fail to detect the microstructure precisely.

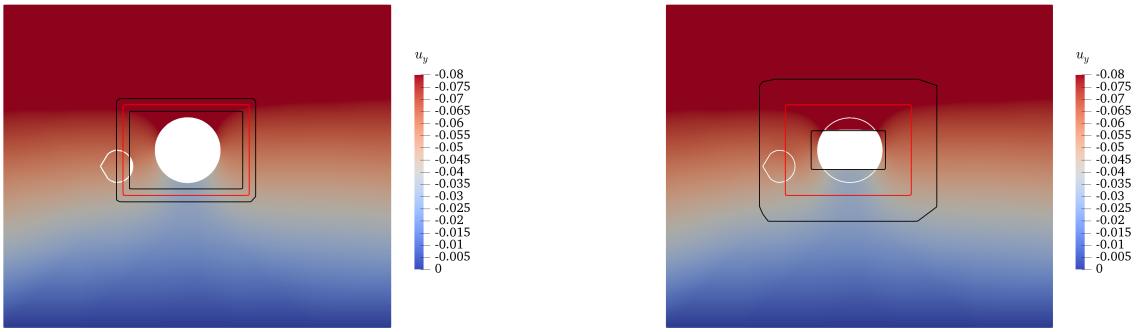

(a) (b)

Figure 3.14: Displacement component u_y for a) smoothed multiscale, $2\epsilon = 0.2$, and b) smoothed multiscale, $2\epsilon = 0.8$.

3.4.2.2 The smoothed multiscale with two arbitrary zooms

Next, we investigate the efficiency of our smoothed multiscale approach for the same quasi-uniform porous domain (see Figure 3.2a) using two separate zooms. The displacement at the bottom edge is blocked and $u = (0, -0.1)$ is applied along the top edge of the domain. We consider the following microscale material properties: $E_m = 1$ and $\nu_m = 0.3$, while for the macro scale, we derive effective material properties by using homogenisation Equation 3.37. Like in the previous Section, we compute the effective Young's modulus based on the pores in the entire domain Ω as $E_{\mathcal{M}} = 0.78$.

For this example, we employ the same background meshes as for the locally porous domain (Figure 3.7) and show the corresponding discretised domain and generated interfaces in Figure 3.15. The smooth indicator function with three lengths

is computed for the finest adaptive mesh in Figure 3.16. In Figures 3.15 and 3.16, we observe the independency of the microstructure, zooming geometry and mixing length to the computational mesh, which creates a straightforward preprocessing pipeline and saves mesh regeneration costs.

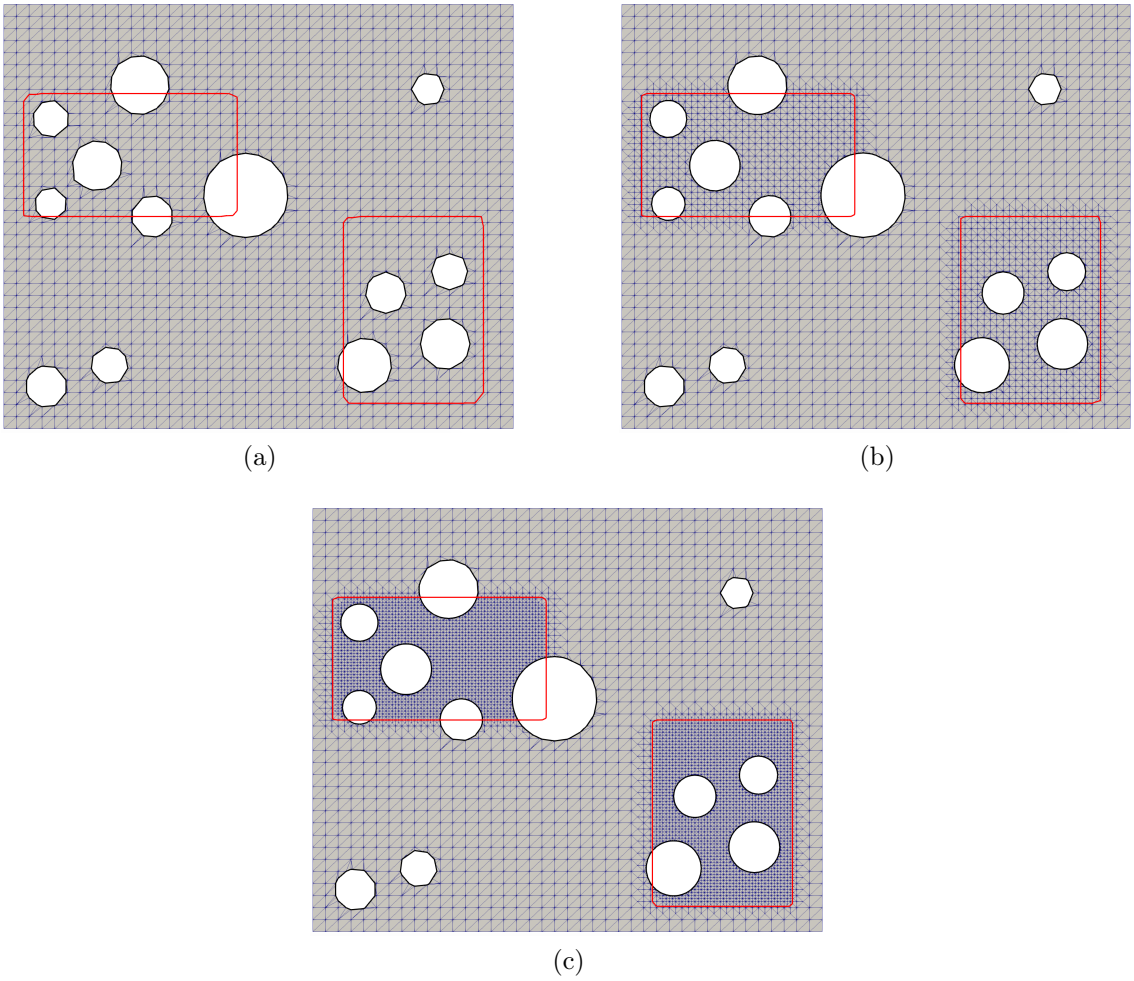

(a) (b)

(c)

Figure 3.15: Computational mesh for physical domain of 2D model with quasi-uniform distributed pores, a) uniform meshing, b) adaptive meshing type 1, c) adaptive meshing type 2.

We compute displacement field component u_y for two smoothing lengths $2\epsilon = \{0.1, 1\}$, and show the corresponding results over the physical and the fictitious domains in Figure 3.17c-f. The results prove a high relevance of the multiscale

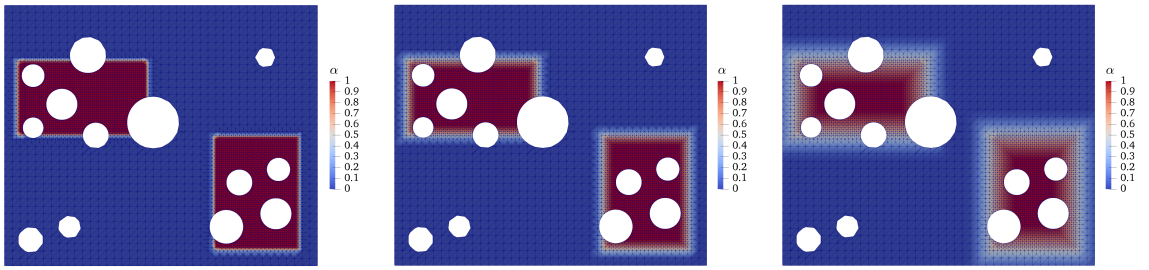

(a) (b) (c)

Figure 3.16: Smooth weight function field α_h over finest adaptive mesh with a) $\epsilon = 0.1$ b) $\epsilon = 0.4$ c) $\epsilon = 1$.

framework in the microscale domain to the corresponding reference models (depicted in Figure 3.17a,b). In the transition regions, u_y as a global response is smooth for both mixing lengths and outside the zooms (homogenised domain) the trend is similar to the references.

Next, we inspect the distribution of the smoothed stress field for two zooming problems. The results obtained for stress field component σ_{yy} for two smoothing lengths and over physical and fictitious domains are given in Figure 3.18. The comparison with reference models (see Figure 3.18) shows that the stress does not suffer from any oscillations neither in cut elements nor in the transition area. The ghost penalty regularisation, which extends the solution from the physical domain to the fictitious domain alleviates the oscillations successfully while ensuring an accurate stress solution.

The condition number of the multiscale system matrix for different mesh configurations and smoothing lengths are compared with the counterpart CutFEM microscale model in Figure 3.19a. The comparison shows that our multiscale assembled matrix is well-conditioned under various smoothing lengths and mesh sizes and converges proportional to h^{-2} that is similar to the CutFEM convergence.

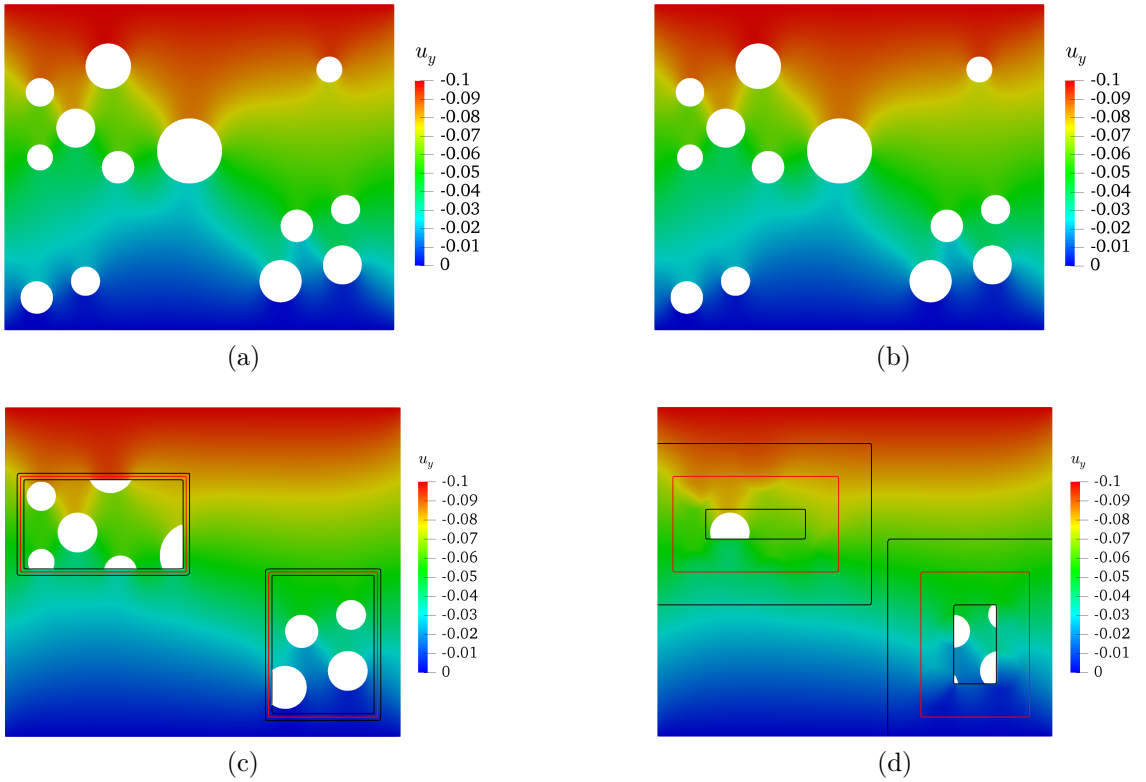

Figure 3.17: Displacement field component u_y, a) FEM model, b) CutFEM model, c) smoothed multiscale model with $\epsilon = 0.1$, d) smoothed multiscale model with $\epsilon = 1$.

3.4.3 3D smoothed multiscale modelling of trabecular bone

This numerical example illustrates the efficacy of the proposed smoothed multiscale framework in 3D simulations. We use a 3D bone sample with a trabecular microstructure which is transferred directly from a micro-CT medical image. The corresponding 3D reconstructed micro-CT image is presented in Figure 3.20. We use the 3D reconstructed image to compute a surface mesh (STL mesh data) which will be converted into a level set function. For more information on the digital pipeline that we have used to convert STL mesh data into a level set function, see [55]. Using our proposed zooming technique, we select the zoom region and apply the mixing scheme to the bone as shown in Figure 3.21. The red and black lines represent the zoom surface and the upper/lower bounds of the mixing regions, respectively. The

bone microstructure is defined by the zero level set function Γ_1^h and the corresponding surface meshing and the CutFEM cell subtesselation are depicted in Figures 3.21a and 3.21b, respectively.

We employ the MMTT to compute the macroscale effective material properties. The mixing approach uses the level-set-based indicator function α_h, defined in Equation (3.35), as shown in Figure 3.22. For the homogenisation, we obtain the volume fractions of trabecular bone from [193], where the bone volume fraction is reported as $B_v = 0.192$. Assuming the microscale properties as $E_m = 1$ and $\nu_m = 0.3$, we derive the homogenised properties as $E_{\mathcal{M}} = 0.15$ and $\nu_{\mathcal{M}} = 0.3$.

We perform a compression test for a full microscale FEM (as reference) and the smoothed multiscale method with one zooming region in an arbitrary location. The displacement field component u_y of these computations is shown in Figure 3.23. For the smoothed multiscale approach, the 3D simulations are carried out for two different smoothing lengths ($2\epsilon = 0.01, 0.1$) to study the mixing technique's stability for both sharp and wide transition regions. The comparison between full microscale and multiscale results shows that our level-set-based multiscale method can be successfully applied for 3D complex problems, in a mesh independent manner, and the mixing technique is stable for both types of transition regions.

To further investigate the accuracy of numerical results, we show the variation of stress component σ_{yy} for two smoothing lengths in Figure 3.24. The results show that the response inside the zoom is consistent with the corresponding FEM reference model.

We also study the condition number of the 3D smoothed multiscale system matrix for different smoothing lengths and element sizes. The results in Figure 3.25 show that the condition numbers stay stable for various smoothing lengths and mesh sizes.

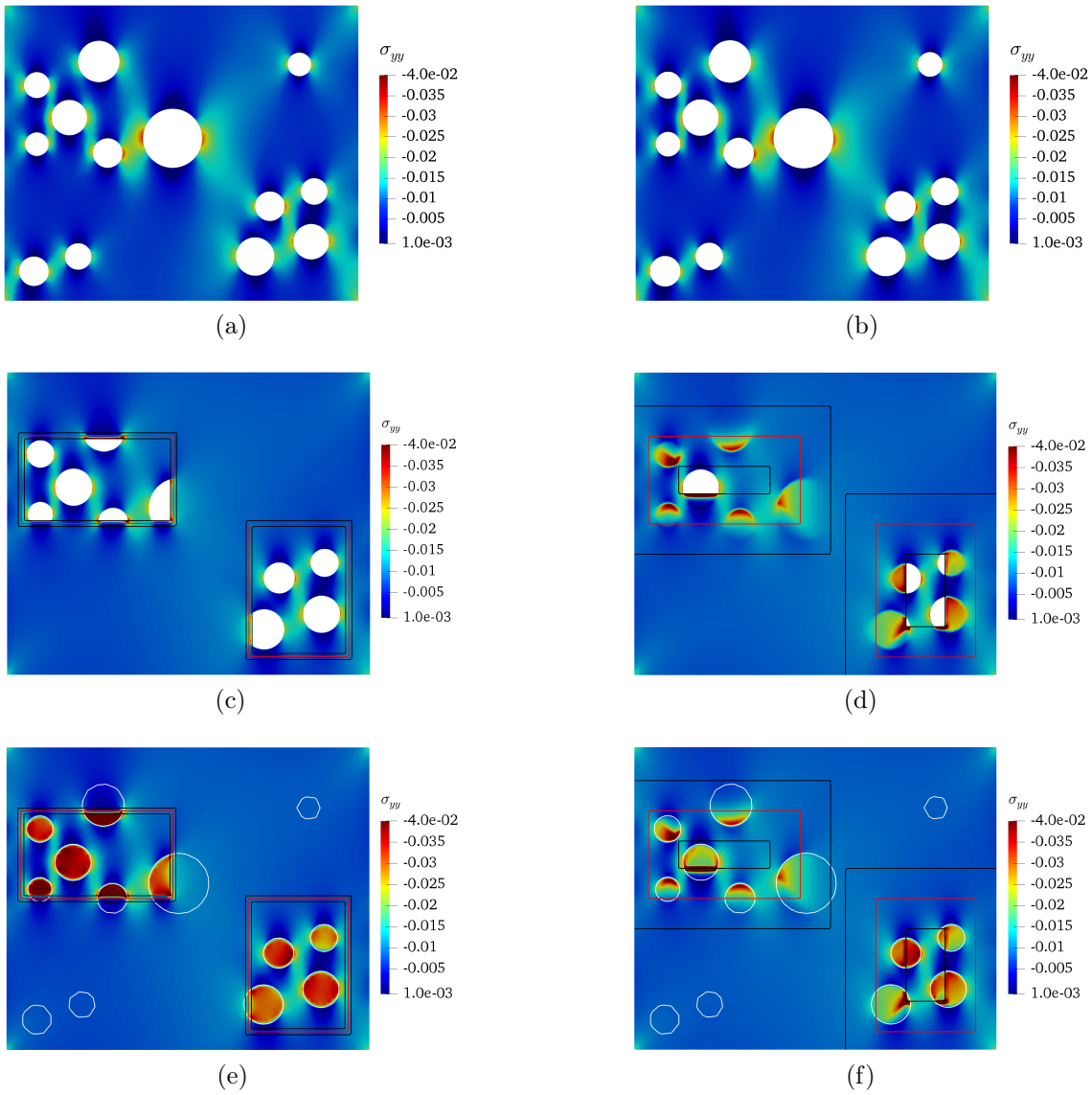

Figure 3.18: Stress component σ_{yy} contours, a) FEM model, b) CutFEM model, c) physical domain for the smoothed multiscale model with $\epsilon = 0.1$, d) physical domain for the smoothed multiscale model with $\epsilon = 1$, e) fictitious domain for the smoothed multiscale model with $\epsilon = 0.1$ and f) fictitious domain for the smoothed multiscale model with $\epsilon = 1$.

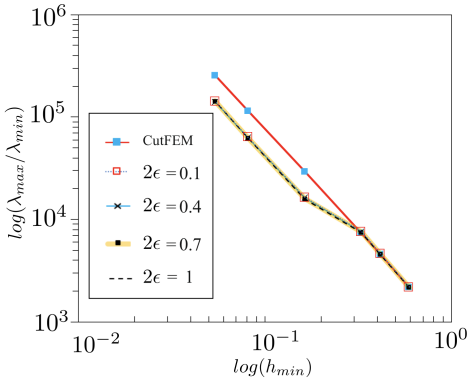

Figure 3.19: Condition numbers for CutFEM model and smoothed multiscale method for different smoothing lengths and mesh configurations. The regularisation parameter is chosen as $\beta = 0.005$.

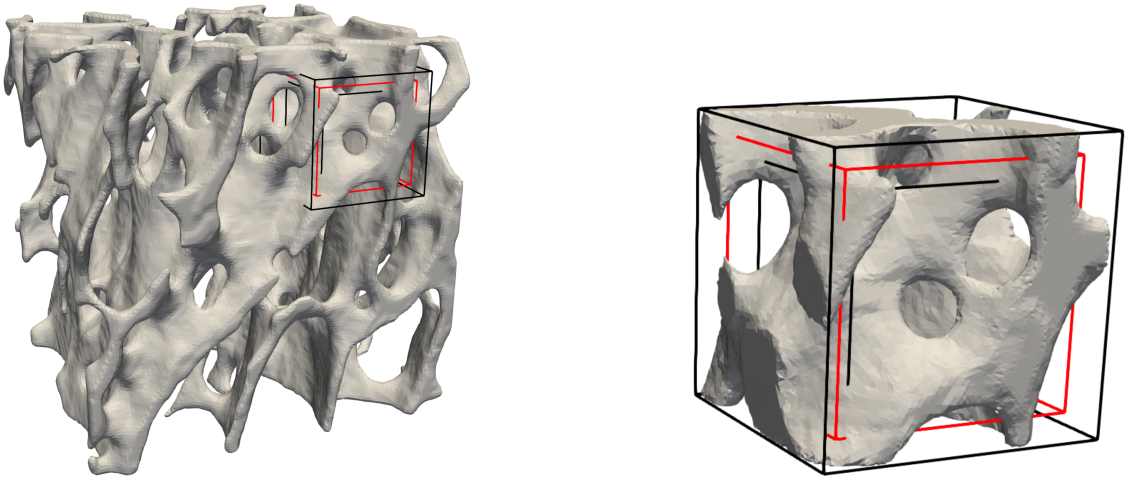

(a) (b)

Figure 3.20: 3D trabecular bone with zoom: (a) Micro-CT image 3D reconstruction, (b) CutFEM interface.

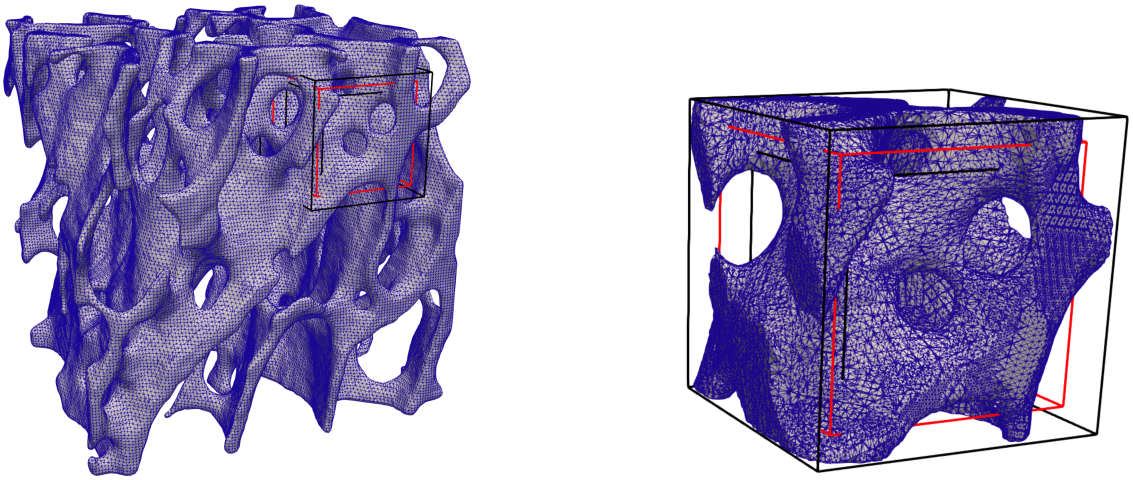

(a) (b)

Figure 3.21: 3-D trabecular bone mesh with zoom: (a) surface mesh of micro-CT image, (b) CutFEM surface subtesselation for $h = 0.036$.

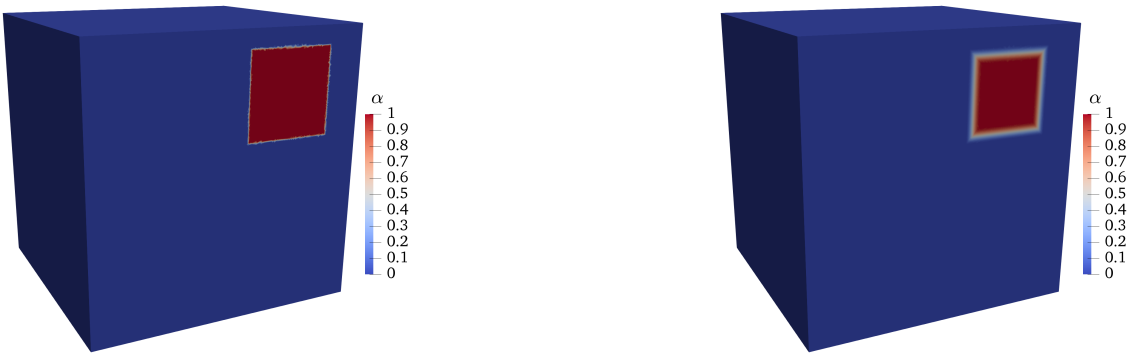

(a) (b)

Figure 3.22: Smoothing weight function α_h used for the 3D bone example with a) $2\epsilon = 0.01$ and b) $2\epsilon = 0.1$.

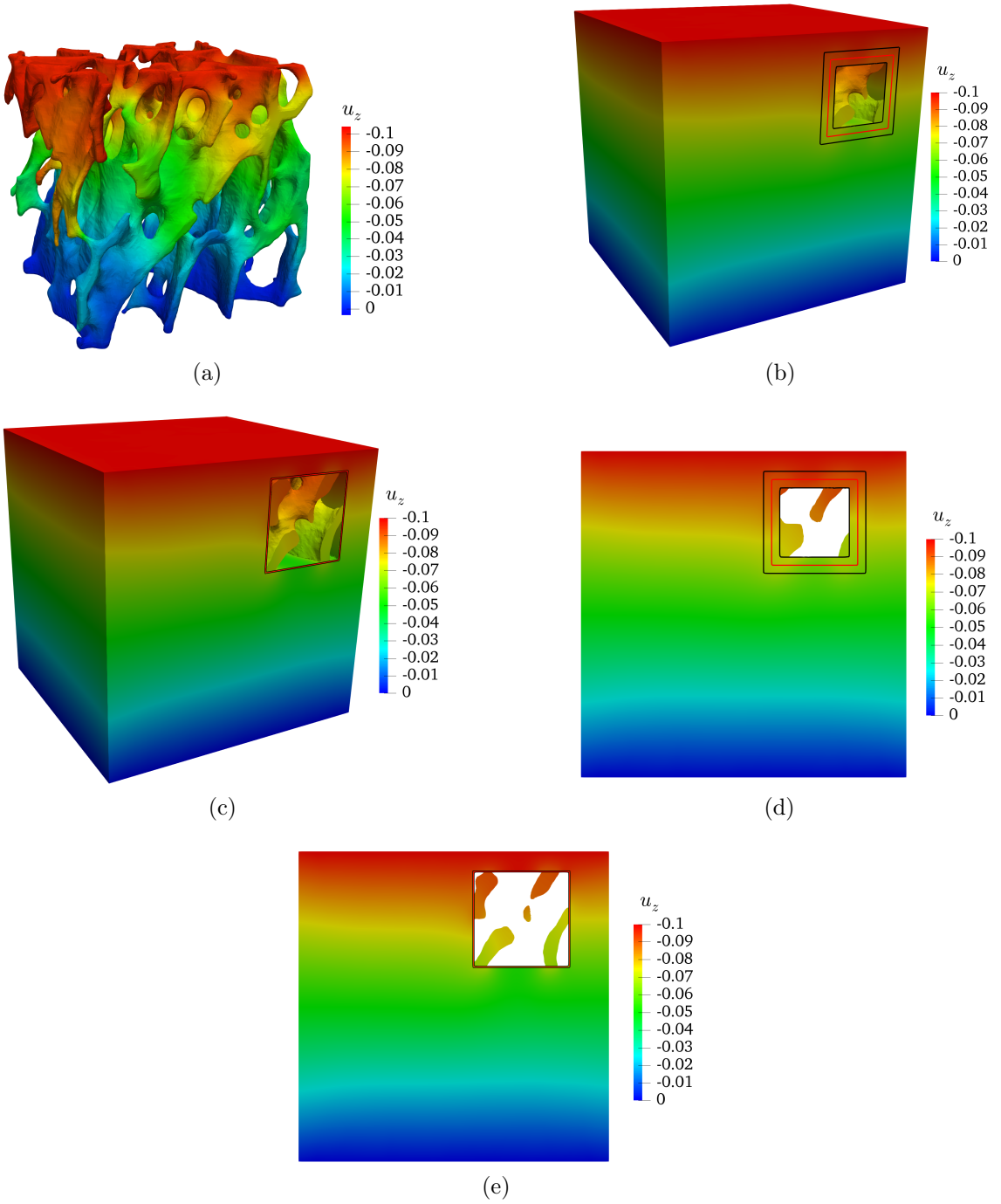

Figure 3.23: 3D and 2D representations of FEM and smoothed multiscale displacement field component u_y, a) 3D FEM reference model, b) $2\epsilon = 0.1$, c) $2\epsilon = 0.01$, d) $2\epsilon = 0.1$ and e) $2\epsilon = 0.01$.

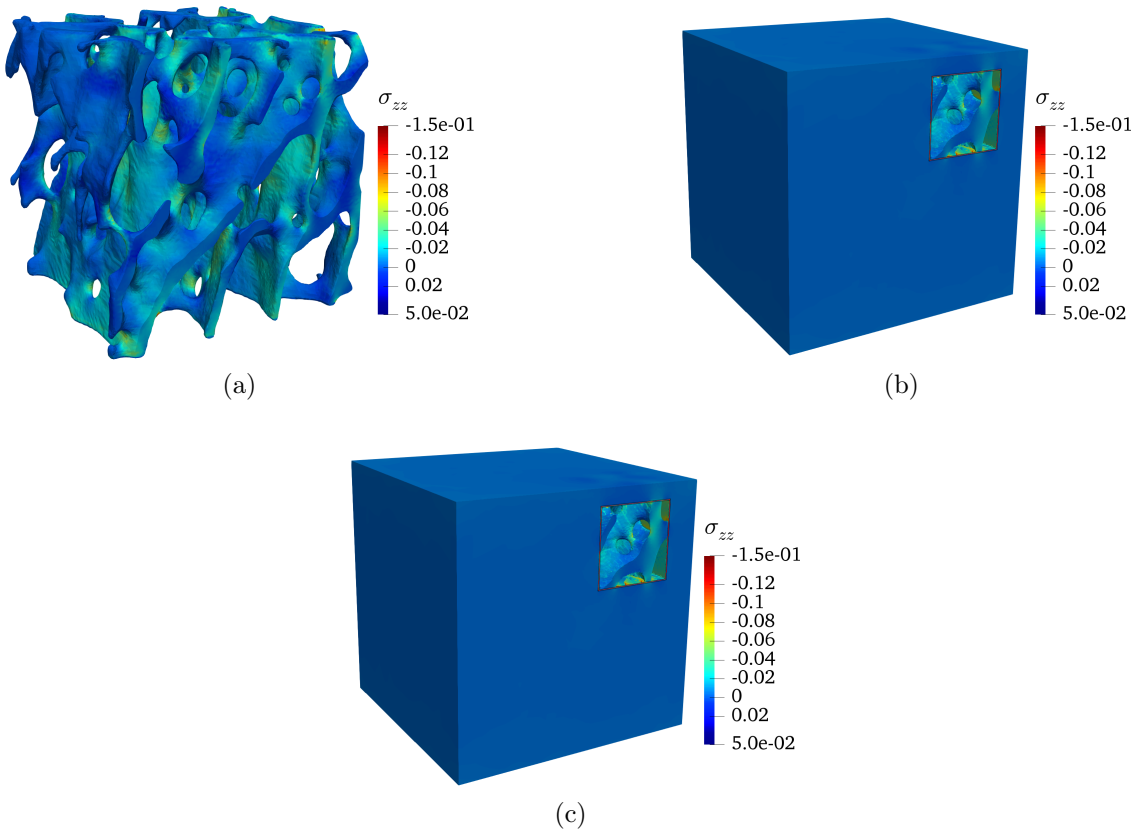

Figure 3.24: Stress component σ_{yy}, a) FEM with $h = 0.036$, b) smoothed multiscale model-A with $h_{min} = 0.036$, $\epsilon = 0.01$ and only cut elements regularised, and c) smoothed multiscale model-B with $h_{min} = 0.036$, $\epsilon = 0.01$, cut and porous elements are regularised.

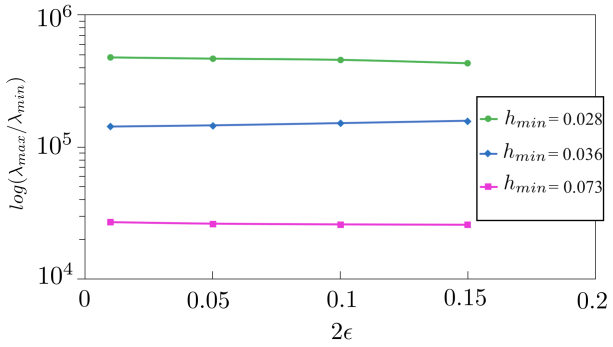

Figure 3.25: Condition numbers for smoothed multiscale models with various mesh sizes and smoothing lengths.

3.5 Conclusion

In this chapter, a framework was proposed to construct an unfitted concurrent multiscale model for heterogeneous structures. In our methodology, we proposed a mixing strategy using a single background mesh to couple micro and macro scale models. Unlike domain decomposition methods where an interface condition is required between macro and microscale models, the interface constraint is not needed in our mixing technique.

We demonstrated the validity of our smoothed concurrent multiscale framework for linear elasticity in 2D and 3D. We first tested the idea of a functional description of the whole heterogeneous structure by projecting it onto a fixed background mesh which is fine in ROI and coarse outside. The projection of the functional description onto an adapted background mesh was carried out successfully by CutFEM, where the geometry was approximated by a piecewise linear signed distance function in each background mesh element. We showed that the accuracy of results in the fine regions is acceptable. However, the very coarse elements outside of the ROI give rise to the random appearance of geometrical artefacts in the coarse region, yielding stress singularities. Next, we tested the same problem within the concurrent multiscale framework where an equivalent homogenised domain was adopted in the coarse region. The results showed that employing the multiscale approach improves the results in the coarse domain. We extended our framework to 3D elasticity problems, where a given surface mesh of trabecular bone was used to define the microscale geometry. The obtained results show a good agreement with the corresponding reference model in terms of global and local responses. Moreover, the corresponding multiscale system matrix remains well-conditioned under various transition region sizes.

Chapter 4

CutFEM-based multiscale techniques for phase field fracture problems

4.1 Introduction

4.1.1 Motivation and objectives

The phase field method has shown two outstanding advantages over discrete crack models. First, it can reproduce arbitrary cracks geometry without using enrichment techniques or explicit functions. Second, it is straightforward to implement, particularly when one desires to simulate complex fracturing processes. However, compared with discrete crack models, the phase field method suffers from demanding extremely refined meshes in the regions where the crack happens to resolve high damage gradients and maintain accuracy. This is due to the length-scale-based regularisation of the phase field method that regularises steep damage gradient within bands. As discussed in chapter 2, several techniques are available to reduce the computational costs of the phase field methods, including adaptive meshing and multiscale modelling. In this chapter, we focus on multiscale techniques to address the issue.

The chapter is divided into two parts: the first part discusses the extension of the concurrent multiscale method developed in chapter 3 for phase field problems, while in the second part, further investigations are carried out for the homogenisation of

phase field models. The second part of the chapter extends the recent homogenisation framework based on inverse problem analysis by [186] to study the effects of different factors on homogenisation, such as the mesh-size, microstructure and error functional.

4.1.2 Introduction of the phase field approximation for quasi-static brittle fractures

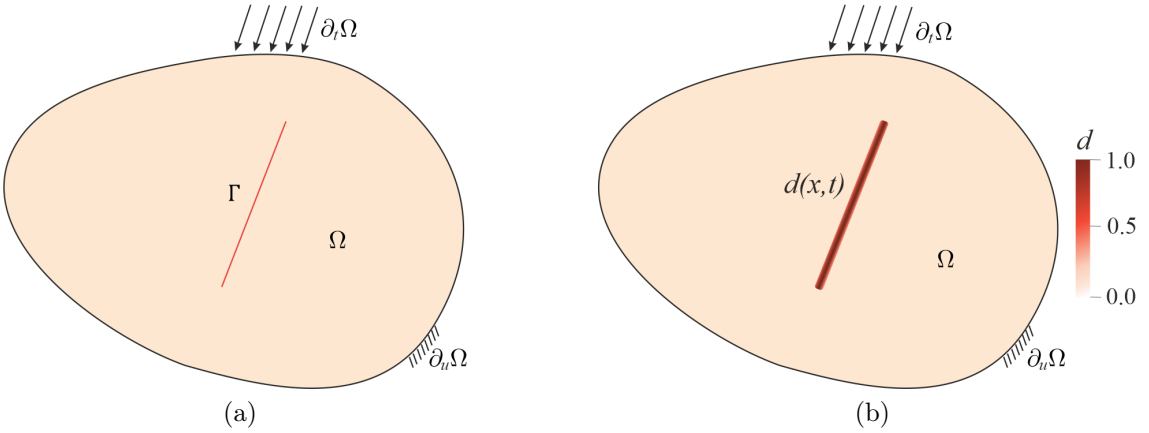

Figure 4.1: Schematic presentation of fracture problems: original discrete problem (a) and phase field approximation (b).

Here, we cover the fundamental formulations of the phase field approach for brittle fracturing that will be extended for multiscale techniques in the following sections.

Let Ω be an arbitrary domain, shown in Figure 4.1a, including a pre-existing crack Γ with corresponding crack surfaces. Within the framework of thermodynamics, the variation of the total energy Π is a function of the elastic strain energy density Ψ and the energy W necessary for the formation of two new surfaces. We propose the variation of the total energy in the absence of external forces as follows:

$$\frac{d\Pi}{dA} = \frac{d\Psi}{dA} + \frac{dW}{dA} = 0 \tag{4.1}$$

where the second term is defined in terms of the critical energy release rate g and is

a positive parameter. [120, 121] represented the previous equation in a variational form as follows

$$\Pi = \int_{\Omega} \Psi(\varepsilon) dV + \int_{\Gamma} g d\Gamma \tag{4.2}$$

here, the crack surface Γ is unknown, which imposes difficulties in the calculation of the second term of equation. In the phase field approach, we approximate the sharp geometry of discontinuity in a diffusive manner (see Figure 4.1.b). We define the phase field variable $d \in [0, 1]$, with $d = 0$ as the undamaged region, and $d = 1$ as a full damaged region. The diffusive approximation involves regions owning the following property: $0 \leq d \leq 1$. The phase field approach replaces the second term of equation 4.2 integrated over surface Γ with a term that is integrated over the all computational domain Ω. Thus, equation 4.2 can be rewritten as

$$\Pi_d = \int_{\Omega} \Psi_d(\varepsilon, d) dV + \int_{\Omega} \Gamma_d(d, \nabla d) dV \tag{4.3}$$

where $\Psi_d(\varepsilon, d)$ is the damaged/cracked solid strain energy function and defined as follows

$$\Psi_d(\varepsilon, d) = (1 - d)^2 \Psi(\varepsilon) \tag{4.4}$$

where $(1 - d)^2$ is the degradation function applied to the $\Psi(\varepsilon)$, which is denoted as

$$\Psi(\varepsilon) = \frac{1}{2}\lambda(\mathrm{tr}(\varepsilon))^2 + \mu(\varepsilon : \varepsilon) \tag{4.5}$$

where λ and μ are the Lame's constants.

In equation 4.3, the term Γ_d is defined as the crack density function and given by

$$\Gamma_d(d, \nabla d) = \frac{1}{2\ell} d^2 + \frac{\ell}{2} |\nabla d|^2 \tag{4.6}$$

Here, ℓ is the length scale parameter representing the width of the phase field region. This equation plays a critical role in modelling of crack propagation, which is contingent upon the phase field d and its spatial gradient ∇d.

According to the phase field algorithm, we minimise the total energy (4.3) with respect to the displacement field u and phase field d. Equation 4.3 can be written as a coupled system of equations where we look for displacement field u and phase field d,

$$\nabla \cdot \sigma_d(u,d) = 0\,, \qquad \text{where} \;\; \sigma_d(u,d) = (1-d)^2\sigma(u) \tag{4.7}$$

$$g\big(\frac{d}{\ell} - \ell\Delta d\big) + 2(1-d)\bar{\mathcal{H}} = 0 \tag{4.8}$$

Here, equation 4.7 is the linear momentum equilibrium equation for the cracked body Ω and equation 4.8 refers to the corresponding phase field equation. In above equations (4.7 and 4.8), σ denotes the Cauchy stress tensor and Δd indicates the Laplacian operator. For a traction τ, the natural boundary conditions readily follow as

$$(1-d)^2\sigma \cdot n = \tau \qquad \text{on} \qquad \partial\Omega \tag{4.9a}$$

$$\nabla d \cdot n = 0 \qquad \text{on} \qquad \partial\Omega \tag{4.9b}$$

where n denotes the outward normal to the boundary $\partial\Omega$.

In equation 4.8, the condition of $\big(\frac{d}{\ell} - \ell\Delta d\big) \geq 0$ must always be satisfied that makes the phase field model thermodynamically consistent. Moreover, the term $\bar{\mathcal{H}}$ refers to the history field function which is a positive parameter related to the crack driving force and needs to be updated at each time step when the crack grows. We define $\bar{\mathcal{H}}$ as follows:

$$\bar{\mathcal{H}} = \max_{t\in[0,T]} \; \Psi^+(\varepsilon(t)) \tag{4.10}$$

$\Psi^+(\varepsilon)$ in equation above is given by

$$\Psi^+(\varepsilon) = \frac{1}{2}K\langle \mathrm{tr}(\varepsilon)\rangle_+^2 + \mu(\varepsilon^{\mathrm{dev}} : \varepsilon^{\mathrm{dev}}) \tag{4.11}$$

where $\langle a \rangle_+ = \frac{1}{2}(a + |a|)$ and K is the bulk modulus.

4.2 Concurrent multiscale governing equations for phase field fractures

In this section, we apply the concurrent multiscale method proposed in the previous chapter for the phase field brittle fracturing. Within our concurrent multiscale context, we will use a fixed single background mesh for the discretisation of the domain and let the phase fields evolve over micro and macroscale regions in a fully mesh-independent fashion. In the following, we will define the related domain partitioning and derive the strong and weak forms of governing equations and the discretised formulation.

4.2.1 Domain partitioning

The domain partitioning for the concurrent multiscale phase field model is carried out similarly to the previous chapter, using genuine microstructure inside the zooms and a homogenised model elsewhere.

Following the previous chapter notation, we define a heterogeneous material with computational domain Ω that has a matrix subdomain Ω_1 and a pore subdomain Ω_2. The corresponding boundary of Ω is denoted by $\partial\Omega$ which is given as $\partial\Omega = \partial_t\Omega \cup \partial_u\Omega$ and $\partial_t\Omega \cap \partial_u\Omega = \emptyset$. The corresponding homogenised domain for the heterogeneous domain Ω is denoted by Ω_3 and shown in Figure 4.2b.

Now, we separate the computational domain into two subdomains, including the microscale region $\widehat{\Omega}_m$ and the macroscale homogenised region $\widehat{\Omega}_{\mathcal{M}}$. A schematic presentation of the subdomains is shown in Figure 4.2c, where the phase field fracture has occurred over both subdomains.

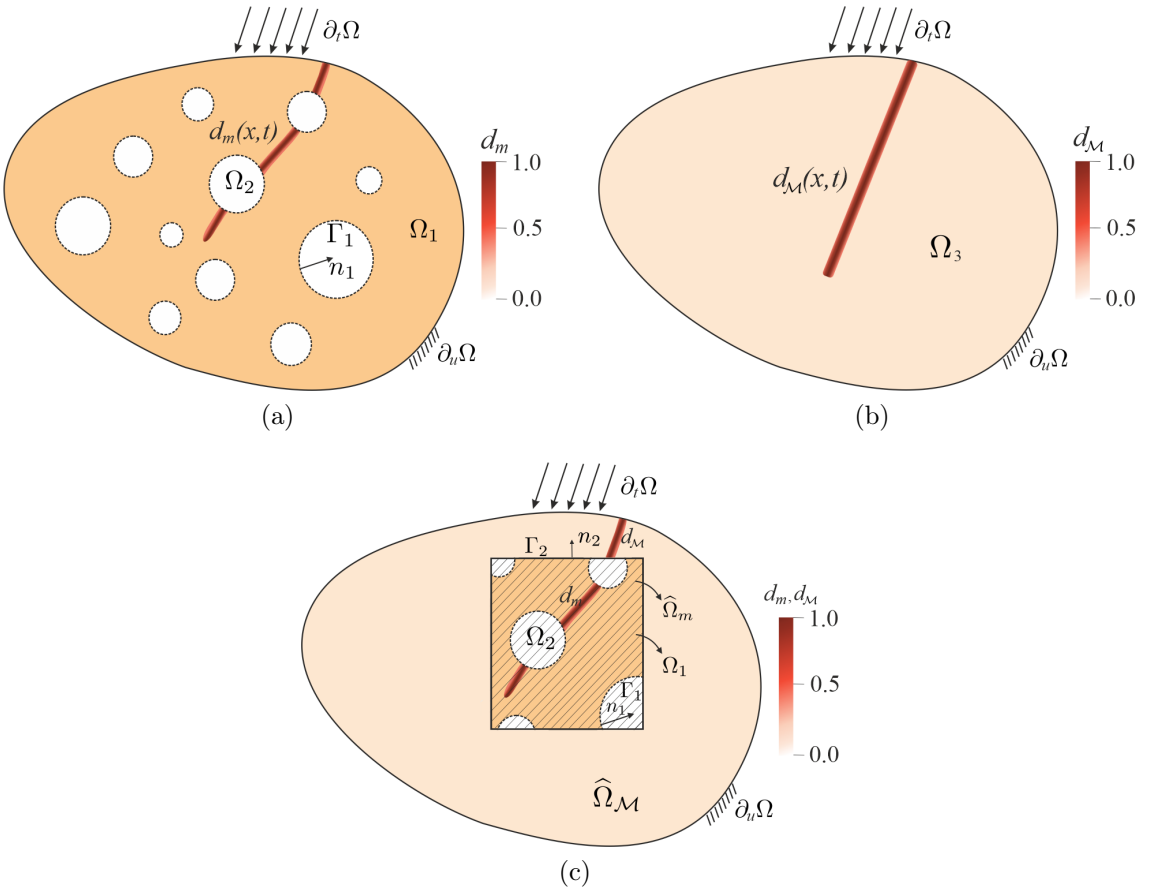

Figure 4.2: Schematic presentation of the phase field fracturing and the corresponding domain partitioning: heterogeneous domain Ω comprised of matrix subdomain Ω_1 and pore subdomain Ω_2 (a), homogeneous domain Ω_3 (b) and partition of domain Ω into macro homogenised subdomain $\widehat{\Omega}_{\mathcal{M}}$ and micro heterogeneous subdomain $\widehat{\Omega}_m$.

4.2.2 Field equations: strong and weak forms

This section presents the strong and weak forms of the governing equations for the phase field fracture problems in the context of the proposed concurrent multiscale framework in chapter 3.

4.2.2.1 Multiscale phase field problem: strong form

We look for displacement field $u : \widehat{\Omega}_{\mathcal{M}} \times \widehat{\Omega}_m \to \mathbb{R}^d \times \mathbb{R}^d$ and phase fields $d_m : \Omega \to \mathbb{R}^d$ and $d_{\mathcal{M}} : \Omega_3 \to \mathbb{R}^d$ satisfying the following equilibrium equations. The corresponding linear momentum equilibrium equation for the cracked heterogeneous structure is defined as follows:

$$\nabla \cdot \sigma_{d,m}(u, d_m) = 0 \qquad \text{in } \widehat{\Omega}_m \tag{4.12a}$$

$$\nabla \cdot \sigma_{d,\mathcal{M}}(u, d_{\mathcal{M}}) = 0 \qquad \text{in } \widehat{\Omega}_{\mathcal{M}} \tag{4.12b}$$

where

$$\sigma_{d,m}(u, d_m) = (1 - d_m)^2 \sigma_m(u), \qquad \sigma_m(u) := D_m : \nabla_s u \tag{4.13a}$$

$$\sigma_{d,\mathcal{M}}(u, d_{\mathcal{M}}) = (1 - d_{\mathcal{M}})^2 \sigma_{\mathcal{M}}(u), \qquad \sigma_{\mathcal{M}}(u) := D_{\mathcal{M}} : \nabla_s u \tag{4.13b}$$

The corresponding micro and macroscale phase field equations are given respectively as,

$$g_m\big(\frac{d_m}{\ell_m} - \ell_m \Delta d_m\big) + 2(1 - d_m)\mathcal{H}_m = 0 \qquad \text{in } \Omega \tag{4.14}$$

$$g_{\mathcal{M}}\big(\frac{d_{\mathcal{M}}}{\ell_{\mathcal{M}}} - \ell_{\mathcal{M}} \Delta d_{\mathcal{M}}\big) + 2(1 - d_{\mathcal{M}})\mathcal{H}_{\mathcal{M}} = 0 \qquad \text{in } \Omega_3 \tag{4.15}$$

In above-mentioned equations, the subscripts m and $\mathcal{M}$ denote the micro and macroscale, respectively. The corresponding parameters are defined as follows: g is the critical energy release rate, ℓ is the length scale parameter and $\mathcal{H}$ is the history field function.

4.2.2.2 Multiscale phase field problem: weak form

Now, we derive the weak form of momentum balance equation 4.7 by integrating over the micro and macroscale subdomains. Like the concurrent multiscale elasticity problem introduced in the previous chapter, we look for the continuous displacement

field $u : \widehat{\Omega}_m \times \widehat{\Omega}_{\mathcal{M}} \to \mathbb{R}^d \times \mathbb{R}^d$ and $u \in H^1(\widehat{\Omega}_m) \times H^1(\widehat{\Omega}_{\mathcal{M}})$ (H^1 denotes the Sobolev space of order one), satisfying

$$\int_{\widehat{\Omega}_m} \sigma_{d,m}(u, d_m) : \nabla_s v \, dx + \int_{\widehat{\Omega}_{\mathcal{M}}} \sigma_{d,\mathcal{M}}(u, d_{\mathcal{M}}) : \nabla_s v \, dx = \int_{\widehat{\Omega}_m} f_b \cdot v \, dx + \int_{\widehat{\Omega}_{\mathcal{M}}} f_b \cdot v \, dx + \int_{\partial\Omega_t} \tau \cdot v \, dx \,, \tag{4.16}$$

for all test functions $v : \widehat{\Omega}_m \times \widehat{\Omega}_{\mathcal{M}} \to \mathbb{R}^d \times \mathbb{R}^d$, $v \in H^1_0(\widehat{\Omega}_m) \times H^1_0(\widehat{\Omega}_{\mathcal{M}})$ which satisfy the homogeneous Dirichlet boundary condition $v = 0 \quad \text{on} \quad \partial\Omega_u$. In the previous equation, the term f_b denotes the body force acting over the macro and microscale model.

The weak form of the phase field equations are also derived by integrating equations 4.15 and 4.14 over Ω and Ω_3 as following: We look for microscale phase field $d_m : \Omega \to \mathbb{R}^d$, $d \in H^1(\Omega)$ and macroscale phase field $d_{\mathcal{M}} : \Omega_3 \to \mathbb{R}^d$, $d \in H^1(\Omega_3)$ that satisfy the following equations, respectively

$$\int_{\Omega} g_m \left(\frac{d_m}{\ell_m} - \ell_m \Delta d_m \right) q + 2(1 - d_m)\mathcal{H}_m q, dx = 0 \quad , \quad \forall q \in H^1_0(\Omega) \tag{4.17}$$

$$\int_{\Omega_3} g_{\mathcal{M}} \left(\frac{d_{\mathcal{M}}}{\ell_{\mathcal{M}}} - \ell_{\mathcal{M}} \Delta d_{\mathcal{M}} \right) q + 2(1 - d_{\mathcal{M}})\mathcal{H}_{\mathcal{M}} q, dx = 0 \quad , \quad \forall q \in H^1_0(\Omega_3) \tag{4.18}$$

where $\nabla d_{\mathcal{M}} \cdot n = 0$ and $\nabla d_m \cdot n = 0$ over $\partial\Omega$, and $d_{\mathcal{M}} = d_m = 1$ over Γ.

4.2.3 Discretised formulations

In the discretisation stage, like in chapter 3, we introduce a transition region Ω_T for coupling micro and macroscale models, as shown with a yellow colour in Figure 4.3. Herein, since we solve a coupled problem, we mix both of the solution fields in the transition region, i.e. phase fields (d_m and $d_{\mathcal{M}}$) and stress fields (σ_m and $\sigma_{\mathcal{M}}$).

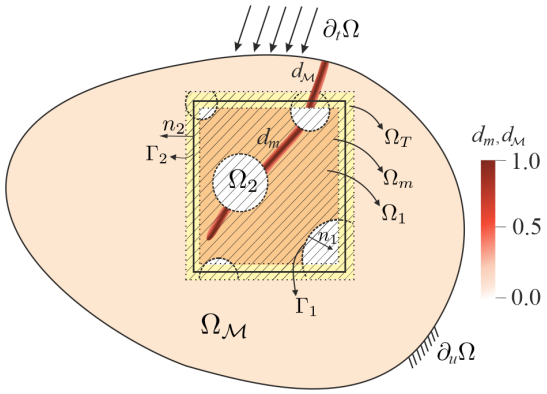

Figure 4.3: Schematic presentation of the phase field fracturing in the context of concurrent multiscale analysis

For the concurrent multiscale phase field problem, we use the multiscale finite element space and the fictitious domain proposed in sections 3.3.1 and 3.3.2 of chapter 3. In that case, we represent the vector-valued and scalar-valued continuous piecewise linear spaces required to discretise displacement field and phase fields respectively, as:

$$\mathcal{U}^h := \{u \in \mathcal{C}^0(\Omega_{\mathcal{T}}) : u|_K \in \mathcal{P}^{s,1}(K) \quad \forall K \in \mathcal{T}_h\}, \tag{4.19}$$

and

$$\mathcal{D}^h := \{d \in \mathcal{C}^0(\Omega_{\mathcal{T}}) : u|_K \in \mathcal{P}^{s,1}(K) \quad \forall K \in \mathcal{T}_h\}, \tag{4.20}$$

where s denotes the spatial dimension, $s = 2$.

The mixed (smoothed) finite element formulation for the proposed multiscale phase field method is as following: find $u^h \in \mathcal{U}^h$, such that

$$a^u_{\mathcal{M}}(u^h, v^h) + a^u_m(u^h, v^h) + s^u_m(u^h, v^h) = l^u_{\mathcal{M}}(v^h) + l^u_m(v^h) \tag{4.21}$$

In Equation 4.21, we add the ghost penalty regularisation term s^u_m for stabilisation of cut elements. The corresponding discretised macro and micro bilinear forms are

given respectively as following:

$$a^u_{\mathcal{M}} = \int_{\Omega^h_{\mathcal{M}}} \alpha^h (1 - d^h_{\mathcal{M}})^2 D_{\mathcal{M}} \nabla_s u^h \nabla_s v^h dx \tag{4.22}$$

$$a^u_m = \int_{\Omega^h_m} (1 - \alpha^h)(1 - d^h_m)^2 D_m \nabla_s u^h \nabla_s v^h dx \tag{4.23}$$

$$s^u_m = \sum_{\Gamma \in \mathcal{F}_G} \left(\int_\Gamma \frac{(1 - \alpha^h)\beta h}{E_m} (1 - d^h_m)^2 [\![D_m \nabla_s u^h]\!] [\![D_m \nabla_s v^h]\!] d\Gamma \right) \tag{4.24}$$

and the discretised linear forms are also defined as

$$l^u_{\mathcal{M}} = \int_{\Omega^h_{\mathcal{M}}} \alpha^h f_b \cdot v^h dx \tag{4.25}$$

$$l^u_m = \int_{\Omega^h_m} (1 - \alpha^h) f_b \cdot v^h dx \tag{4.26}$$

In equation 4.24, the term $\beta > 0$ and represents the ghost penalty stabilisation parameter.

As discussed in the previous section, the macroscale and microscale phase fields are solved separately, over the entire computational domain. We discretise the microscale phase field equation (4.17) as following: find $d^h_m \in \mathcal{D}^h$ such that

$$a^d_m(d^h_m, q^h) + s^d_m(d^h_m, q^h) = l^d_m(q^h) \tag{4.27}$$

In the above equation, the stabilisation term s^d_m is added on the edges of the cut elements accounting the jump of stress in the normal direction, to ensure the stability of these elements. Also, the bilinear form is defined as

$$a^d_m(d^h_m, q) = \int_{\Omega^h_m \cup \Omega^h_{\mathcal{M}}} g_m \ell_m \nabla d^h_m \nabla q^h + \left(\frac{g_m}{\ell_m} + 2(1 - \alpha^h) H_m \right) d^h_m q^h dx \tag{4.28}$$

with the corresponding stabilisation term given by

$$s_m^d(d_m^h, q^h) = \sum_{\Gamma \in \mathcal{F}_G} \int_\Gamma \bar{\beta} \ell_m h \, [\![D_m \nabla_s d_m^h]\!] \, [\![D_m \nabla_s q^h]\!] \, d\Gamma \tag{4.29}$$

and the linear form presented as

$$l_m^d(q^h) = \int_{\Omega_m^h \cup \Omega_{\mathcal{M}}^h} 2(1-\alpha^h) H_m q^h \, dx \tag{4.30}$$

In equation 4.29, the term $\bar{\beta} > 0$ and represents the stabilisation parameter for the phase field.

For the macroscale phase field equation (4.18), we also find $d_{\mathcal{M}}^h \in \mathcal{D}^h$, such that

$$a_{\mathcal{M}}^d(d_{\mathcal{M}}^h, q^h) = l_{\mathcal{M}}^d(q^h) \tag{4.31}$$

where the bilinear and linear forms are defined respectively as

$$a_{\mathcal{M}}^d(d_{\mathcal{M}}^h, q^h) = \int_{\Omega_{\mathcal{M}}^h \cup \Omega_m^h} g_{\mathcal{M}} \ell_{\mathcal{M}} \nabla d_{\mathcal{M}}^h \nabla q^h + \left(\frac{g_{\mathcal{M}}}{\ell_{\mathcal{M}}} + 2\alpha^h H_{\mathcal{M}} \right) d_{\mathcal{M}}^h q^h \, dx \tag{4.32}$$

$$l_{\mathcal{M}}^d(q^h) = \int_{\Omega_{\mathcal{M}}^h \cup \Omega_m^h} 2\alpha^h H_{\mathcal{M}} q^h dx \tag{4.33}$$

The stabilisation terms, s_m^u and s_m^d defined above, play crucial roles in stabilising the cut elements and enhancing the stability of the concurrent multiscale model. The arbitrary intersection of elements by the interfaces can introduce numerical instabilities and inaccuracies, in particular when the cut is very close to the nodes. These terms help mitigate the mentioned issues by penalising the cut elements. The ghost penalty regularisation terms consist of a summation over the cut faces Γ belonging to the set $\mathcal{F}_G$, which represents the interface between the cut elements and the rest of the mesh.

4.2.4 Numerical examples

In this section, we study two types of problems; (1) we only investigate the performance of the smoothed concurrent multiscale modelling for phase field problems and assume that the macro and microscale phase field parameters are predetermined, while in (2), we assume that we do not have access to the macroscale fracture parameters besides the full microstructure. In the latter case, we construct an inverse problem to identify the unknown macroscale phase field parameters. In the inverse problem, we fit the force-displacement curves of the macroscale homogenised model (with unknown properties) and the concurrent multiscale model (with the arbitrary location of zoom).

4.2.4.1 Validation of the concurrent multiscale method for phase field cracking

Here, we employ the concurrent multiscale method for numerical modelling of periodic porous lattice, shown in Figure 4.4, with available microscale and macroscale mechanical and fracture parameters. The microscale properties are as follows: $E_m = 2.1 \times 10^5, \nu_m = 0.3, g_m = 2.7, \ell_m = 0.04$. The corresponding macroscale homogenised material properties are computed by MTT and considered as $E_{\mathcal{M}} = 0.51 E_m, \nu_{\mathcal{M}} = 0.3$. We also assume that the macroscale fracture parameters are predetermined and given as $g_{\mathcal{M}} = 1.50, \ell_{\mathcal{M}} = 0.04$. Moreover, the radius of micro circular-pores is adopted as $r = 0.02$.

In order to accurately capture the phase field, which demands a fine mesh resolution, we perform mesh refinement in the regions expected to undergo cracking. The meshing is performed using the CutFEM algorithm, where the smallest element size is set to $h_{min} = 0.007$. The selection of mesh refinement areas is guided by prior knowledge obtained from a full fine scale simulation, serving as our reference model. Consequently, the mesh size of the reference model is adopted for the refined regions. Figure 4.5 illustrates the discretised domains for both the full microscale CutFEM and smoothed multiscale models, showcasing the refined mesh configuration.

Figure 4.6 presents the results obtained from the full microscale CutFEM (as a

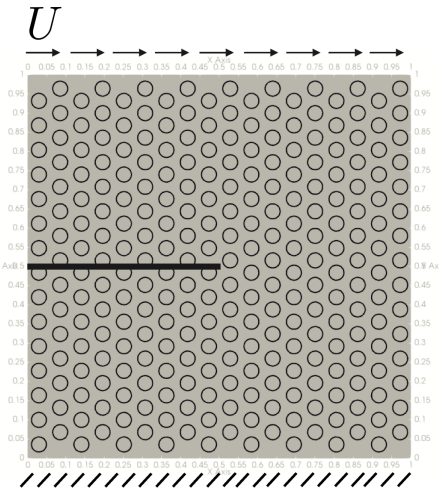

Figure 4.4: Schematic presentation of the heterogeneous structure with periodic micro pores and the corresponding boundary conditions.

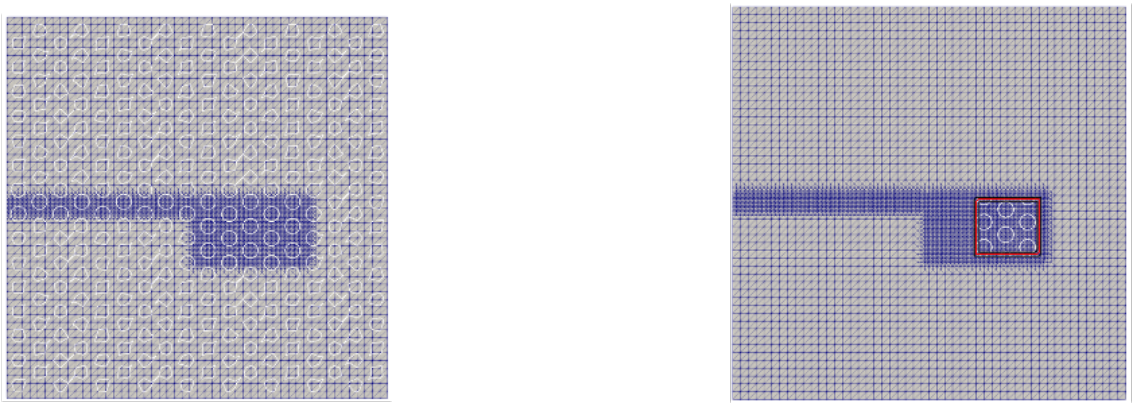

(a) (b)

Figure 4.5: Computational meshes: a) full microscale CutFEM, b) smoothed concurrent multiscale model.

reference model) and the smoothed concurrent multiscale method. The phase field growth path for the multiscale model is in good agreement with the reference model. The force-displacement curve in Figure 4.7 also depicts a similar trend in the global responses between the two models. Moreover, we verify the results by examining the maximum reaction force, which serves as an appropriate indicator for comparing the

ultimate bearing capacity of the two models. We should also mention that the sharp jumps observed in the curves are a result of the micro pores, which lead to sharp unloading behaviours in the softening regime.

Finally, we proceed with a comparison of the computational costs associated with the two models. The full microscale CutFEM requires approximately 22 minutes of computational time, whereas the smoothed multiscale model completes within 19 minutes. This comparison clearly demonstrates the enhanced efficiency of our smoothed multiscale approach in terms of computational costs. However, it is important to note that the advantages of our approach become even more pronounced when considering three-dimensional and larger structures. In such cases, the computations become significantly more affordable, making our smoothed multiscale approach even more appealing.

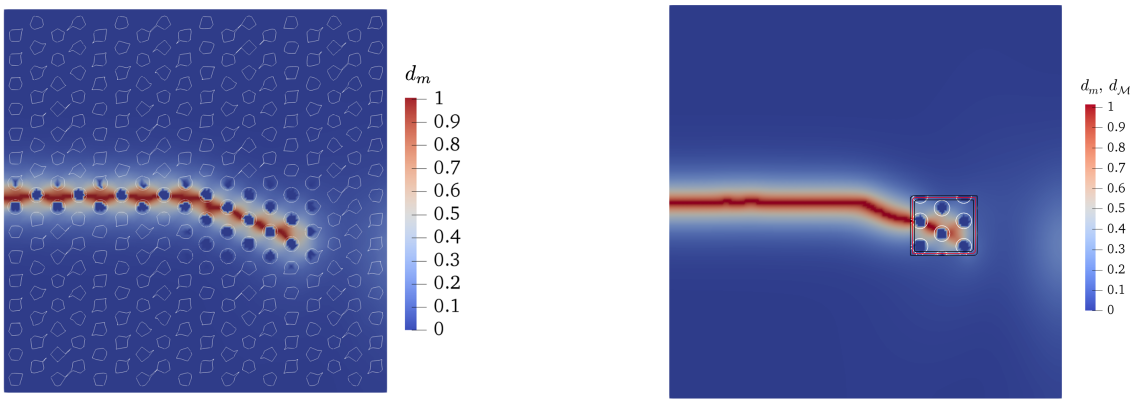

(a) (b)

Figure 4.6: Phase field contour in the last time step: (a) full microscale CutFEM (d_m) and (b) smoothed concurrent multiscale model (d_m and $d_{\mathcal{M}}$).

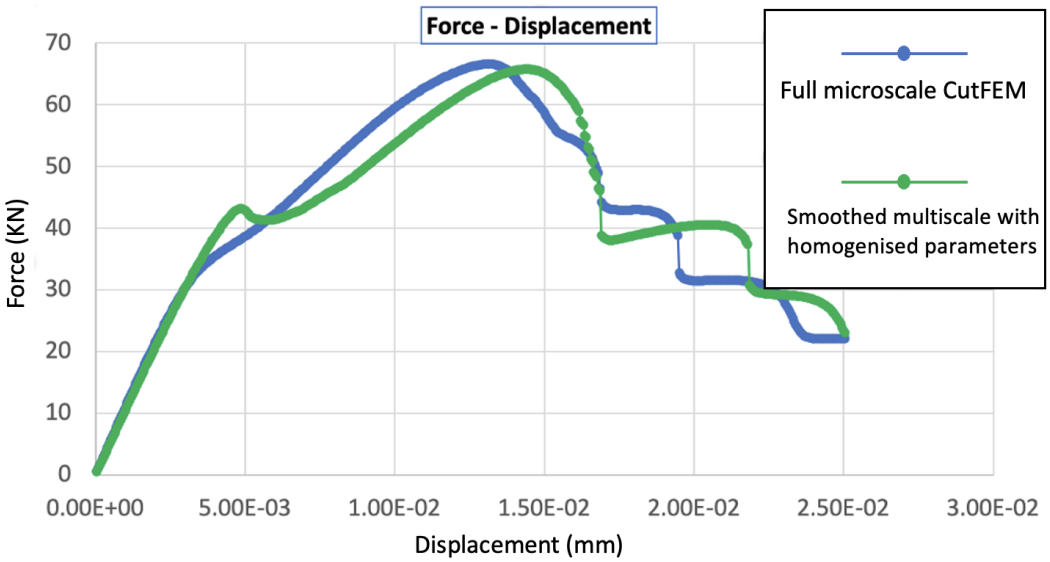

Figure 4.7: Force displacement curve.

4.2.4.2 Identification test for the phase field parameter $g_{\mathcal{M}}$

Here, we intend to identify the fracture parameter $g_{\mathcal{M}}$ for the heterogeneous porous structure in the previous example (shown in Figure 4.4). This way, we can illustrate whether the predetermined parameter has been selected correctly or not. To do so, we follow the work by [186] to construct an inverse problem that aims to fit the force-displacement curves in the full macroscale and full microscale models while finding the optimised value of $g_{\mathcal{M}}^{opt}$. The corresponding computational meshes for the full microscale CutFEM and full macroscale FEM are presented in Figures 4.8a,b, respectively.

The microscale material and fracture properties of the heterogeneous structure are $E_m = 2.1 \times 10^5, \nu_m = 0.3, g_m = 2.7, \ell_m = 0.04$. For the macroscale mechanical properties, we employ MMTT and derive as following: $E_{\mathcal{M}} = 0.51 E_m, \nu_{\mathcal{M}} = 0.3$. The macroscale length parameter is also considered as $\ell_{\mathcal{M}} = 0.04$.

We aim at identifying the optimised value for $g_{\mathcal{M}}$ that minimises the following error functional:

$$J = \frac{1}{2} \int_0^t \left[f_m - f_{\mathcal{M}} \right]^2 dt \tag{4.34}$$

where f is a force defined as an integral of normal traction along the of top edge of structure projected in x direction. We use the BFGS (Broyden Fletcher Goldfarb Shanno) search algorithm [194] for optimisation purposes from SciPy library. The BFGS algorithm is a widely employed method for solving unconstrained optimisation problems. It belongs to the class of quasi-Newton methods, which approximate the Hessian matrix of the error functional without explicitly computing it. Instead, the algorithm estimates the Hessian using gradients of the error functional. To calculate the gradients, the BFGS algorithm utilises finite differences or automatic differentiation techniques. In our implementation, we employed automatic differentiation provided by the SciPy library, which efficiently computes the gradients numerically. This approach avoids the need for manual derivation and coding of gradients, thereby reducing the potential for errors and enhancing computational efficiency.

Figure 4.9 shows the $J - g_{\mathcal{M}}$ curve and the corresponding optimised value is

$g_{\mathcal{M}}^{opt} = 1.52$, while the microscale counterpart value was $g_m = 2.7$. The corresponding phase field contours for the last time step are shown in Figure 4.10a,b, respectively. The results demonstrate the high accuracy of the macroscale phase field in terms of thickness, growth direction and length. Additionally, the force-displacement curves for the full microscale CutFEM and full macroscale FEM models are shown in Figure 4.11. The good agreement between the global responses shows that the derived homogenised value for the $g_{\mathcal{M}}$ is correct. Thus, we conclude that our predetermined value for the $g_{\mathcal{M}}$ in the previous example was accurate.

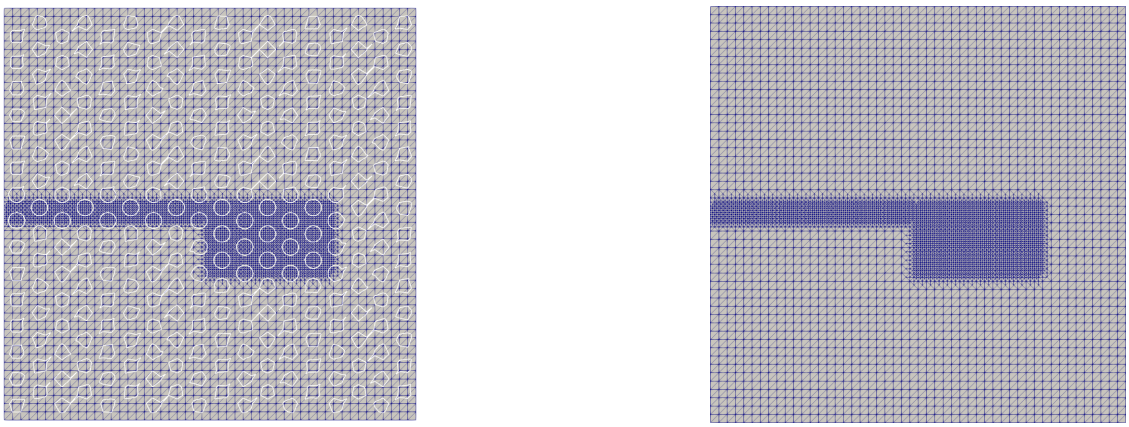

(a) (b)

Figure 4.8: Computational meshes: (a) full microscale CutFEM and (b) full macroscale FEM model.

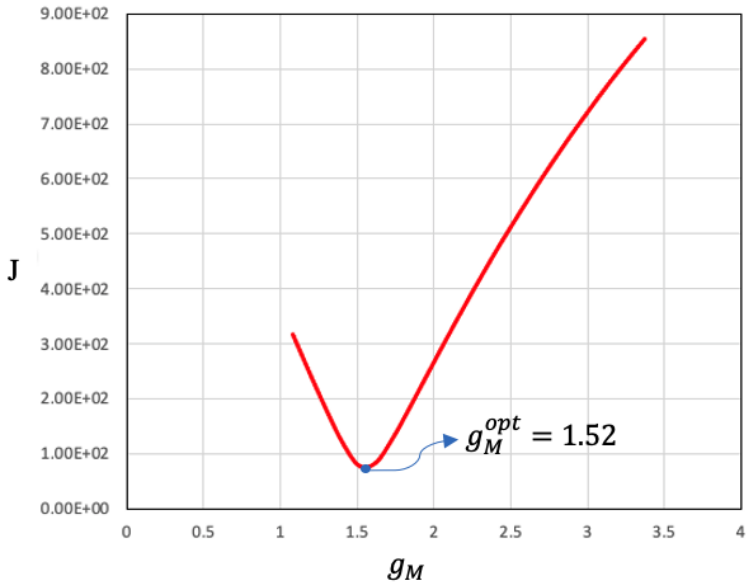

Figure 4.9: $J - g_{\mathcal{M}}$ curve for the periodic porous lattice structure shown in Figure 4.8.

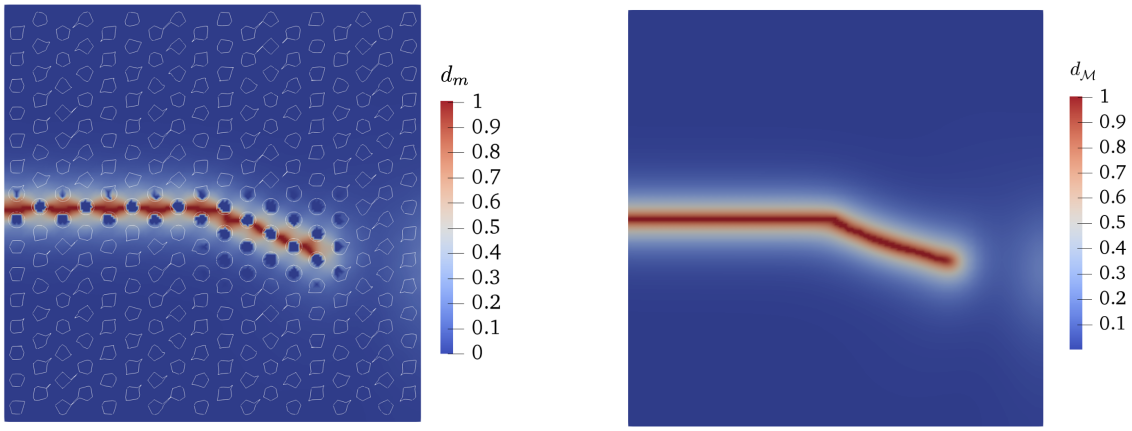

(a) (b)

Figure 4.10: Phase fields: (a) full microscale CutFEM and (b) full macroscale FEM model

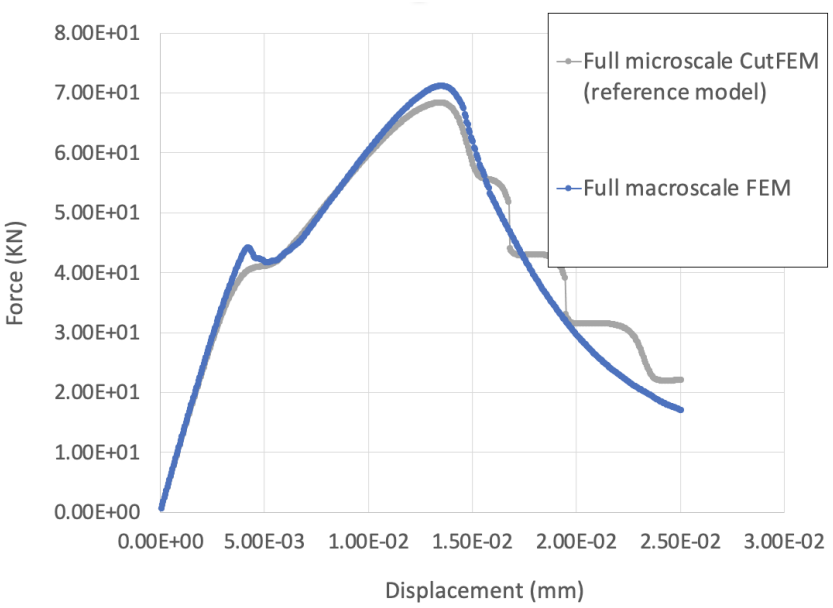

Figure 4.11: Force-displacement curves: (a) full microscale CutFEM and (b) full macroscale FEM.

4.2.5 A new self-consistent identification algorithm for macroscale fracture parameters

When the macroscale phase field parameters are unknown, we follow the homogenisation technique proposed in [186] for identification purposes. However, when we access only a small portion of the microstructure, we can not use the previous methods, which require a full microscale domain as a reference model. Therefore, we here propose a new self-consistent technique using a smoothed concurrent multiscale method as our reference model. In this framework, our inverse problem aims at fitting the force-displacement curve of the homogenised phase field model with the corresponding concurrent multiscale model (as an exact solution). We perform the optimisation problem by minimising the following error functional:

$$J = \frac{1}{2}\int_0^t \left[f_z - f_{\mathcal{M}}\right]^2 dt \tag{4.35}$$

where f_z is the smoothed concurrent multiscale model force, and $f_{\mathcal{M}}$ is the homogenised model force, defined as integrals of normal tractions along the top edge of the structure projected in x direction. Furthermore, the macroscale fracture parameters, e.g. $g_{\mathcal{M}}$ in both models, are unknown. We use the BFGS search algorithm [194] for optimisation purposes from the SciPy library and compare the corresponding result with a direct search method in Figure 4.12.

In our self-consistent approach, we consider the same shear test for a porous lattice in the previous example. A displacement $u_x = 0.025\,mm$ is applied at the top edge of the plate while it is fixed at the bottom, in x and y directions. Unlike $g_{\mathcal{M}}$, the rest material parameters are similar to the previous example.

We perform the optimisation problem for the equation 4.35, where in each iteration $g_{\mathcal{M}}$ is updated for both models, i.e., in full FEM and multiscale model. We calculate the optimised homogenised energy release rate as $g_{\mathcal{M}} = 1.50$. This optimisation problem is based on only one parameter for simplification purposes. However, in the last part of this chapter, we will also study the effects of $\ell_{\mathcal{M}}$ as an optimisation parameter on the results.

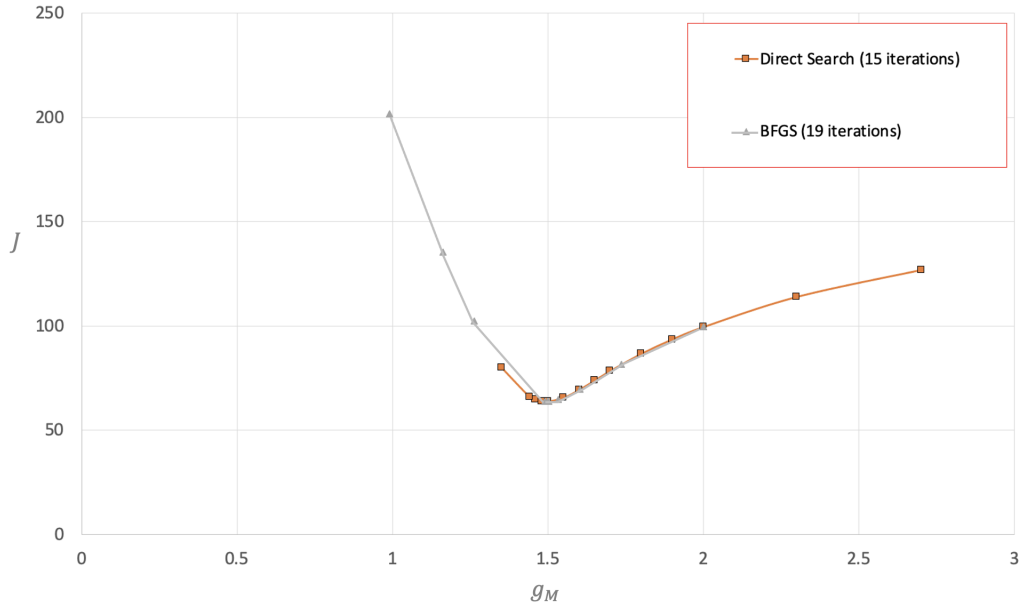

Figure 4.12: $J - g_{\mathcal{M}}$ curve for the self-consistent simulation with two methods: BFGS and direct search methods

The force-displacement curve, as well as the crack path in Figures 4.13 and 4.14 show that we can reproduce suitable results for both macroscale FEM and smoothed multiscale model by only accessing the microscale features inside the zooming region. This self-consistent strategy can be used to predict fracture behaviour, in particular, for large structures where only a small portion of microstructure is accessible. However, the location and geometry of the zooming region in the multiscale model can tremendously affect the accuracy of results and require further considerations in more complex examples. When the zooming region has been selected in a proper way, our new identification approach will leverage the computational efficiency of the smoothed concurrent multiscale method. This is because the full microscale reference model in the conventional identification approach [186] is replaced with the concurrent multiscale model, which requires less computational efforts.

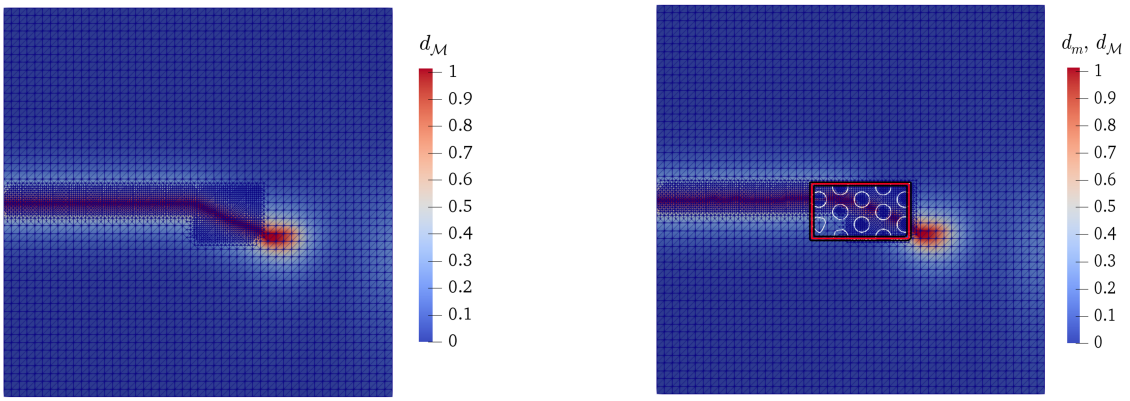

(a) (b)

Figure 4.13: Phase field contours for the last time step: (a) full macroscale FEM and (b) smoothed concurrent multiscale model

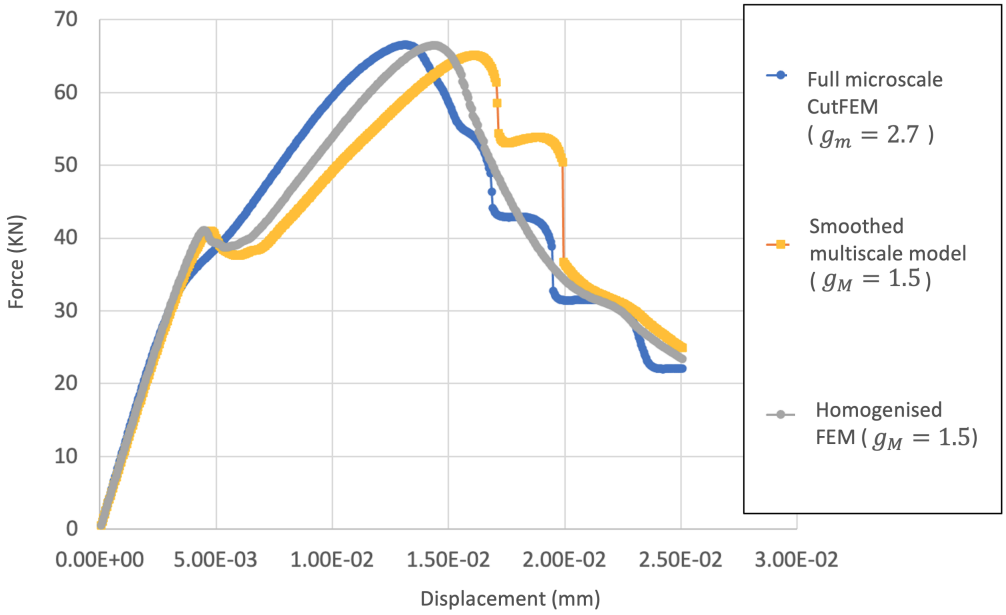

Figure 4.14: Force versus displacement curves for the three models: blue curve represents the full microscale CutFEM model as reference model, yellow curve represents the concurrent multiscale and the grey curve depicts the full macroscale homogenised model.

4.3 Further investigations on the homogenisation of phase field parameters

The homogenisation of fracture properties is not straightforward in comparison to the homogenisation of mechanical properties. This is mainly due to the intrinsic non-linearity of the fracture parameters, which adds more complexity. One common approach for computing the homogenised fracture properties is to use inverse problem frameworks that typically involve minimising a parametric cost function. [186] constructed an inverse problem to study the role of microstructural features, including different types of inclusions, in homogenising the fracture energy release rate parameter. They showed that the parameter is a material-dependent property and can be used for other problems with different settings but featuring the same material.

In this part of the chapter, we perform further investigations following the work by [186] to study the effects of other parameters on the homogenisation of fracture properties (i.e. $g_{\mathcal{M}}$, $\ell_{\mathcal{M}}$). These parameters are as follows:

- Mesh-size: we investigate the effect of mesh coarsening on homogenisation results.
- Boundary conditions: we study the effect of boundary conditions on homogenised fracture parameters.
- Microstructure: we discuss the impact of microstructural parameters onto homogenised fracture parameters.
- Error (Cost) functional: we test various types of error functionals for the homogenisation problem.

Investigations on these four factors will be complementary to the work done by [186], and the corresponding conclusions can be employed directly in the concurrent multiscale framework proposed in the previous section.

4.3.1 Numerical results

In this section, we initially carry out identification tests to capture the unknown homogenised fracture parameters using inverse-problem analysis. Then, we validate the acquired homogenised parameters by testing them on a new problem with new boundary conditions.

4.3.1.1 Effect of mesh coarsening on homogenisation

Identification test. In this section, we investigate and identify the effects of mesh coarsening on the homogenisation of fracture parameters, i.e. $\ell_{\mathcal{M}}$ and $g_{\mathcal{M}}$. A better understanding of the relationship between the macroscale model mesh-size $h_{\mathcal{M}}$ and the homogenised fracture parameters can provide us with new perspectives regarding the properties of the homogenised fracture parameters. This will also allow us to obtain a range of values for the $h_{\mathcal{M}}$ leading to accurate homogenised fracture models. The large value of the $h_{\mathcal{M}}$ will demonstrate to what extent we can perform the mesh coarsening, which can still provide us with an accurate homogenised model.

The geometries and boundary conditions of the heterogeneous microscale and the homogenised macroscale structures with initial cracks are shown in Figure 4.15. The full microscale model, as a reference, is discretised by the CutFEM, as shown in Figure 4.16a. For the homogenised model, we adopt five different meshes with different mesh sizes; see Figure 4.16b-f. The microscale material and fracture properties, besides the macroscale material properties, are the same as in section 4.2.4.1. Here, we aim to determine $\ell_{\mathcal{M}}$ and $g_{\mathcal{M}}$ for each mesh configuration in the homogenised macroscale model. The smallest element size of the mesh in the micro and macro scale subdomains are denoted by $h_{m,min}$ and $h_{\mathcal{M},min}$, respectively.

The inverse problem analysis is carried out between the microscale model and the macroscale model with five different h_{min}. We find optimised values for the unknown $g_{\mathcal{M}}$ and $\ell_{\mathcal{M}}$ by minimising the following error functional:

$$J = \frac{1}{2}\int_0^t \left[f_m - f_{\mathcal{M}}\right]^2 dt \tag{4.36}$$

where f_m is the full microscale model shear force, and $f_{\mathcal{M}}$ is the macroscale shear force along the top edge of the structure. The calculated $g_{\mathcal{M}}$ and $\ell_{\mathcal{M}}$ for the homogenised model for each analysis is reported in table 4.1. The results reveal that the mesh coarsening has slight effects on the value of $g_{\mathcal{M}}$, while for $\ell_{\mathcal{M}}$, a direct dependency on the value of $h_{\mathcal{M},min}$ is obtained.

$h_{\mathcal{M},min}$	$g_{\mathcal{M}}^{opt}$	$\ell_{\mathcal{M}}^{opt}$
0.007 ($=h_{m,min}$)	1.50	0.038
0.014	1.50	0.053
0.028	1.48	0.073
0.035	1.46	0.082
0.047	1.45	0.092

Table 4.1: Optimised values for the $g_{\mathcal{M}}$ and $\ell_{\mathcal{M}}$ of inverse problem analysis between full microscale and full macroscale models.

The corresponding phase fields for each set of optimised $g_{\mathcal{M}}$ and $\ell_{\mathcal{M}}$ besides the reference model are shown in Figure 4.17. It can be seen that by mesh coarsening, the structures become stiffer, and the phase field tends to propagate with less curvature. When we compare the phase field contour of the reference model results with the corresponding macroscale homogenised models, we observe that with a twice coarsening of the mesh, we can still reach acceptable results, which is shown in Figure 4.17c. With further coarsening, the phase field growth path tends to deviate from the correct one, which is not acceptable. Therefore, an acceptable value for the $h_{\mathcal{M}}$ will be within the range of $[h_m - 2h_m]$.

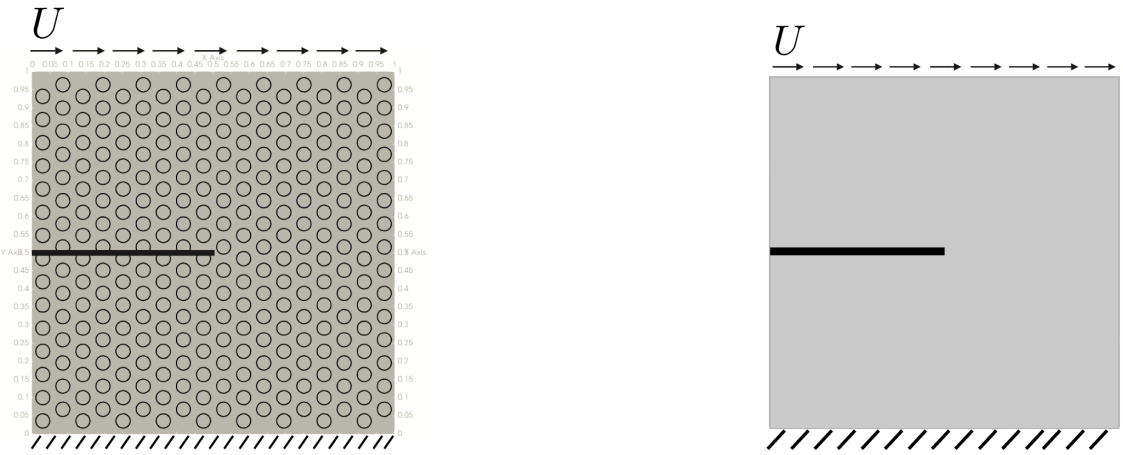

(a) (b)

Figure 4.15: Schematic presentation of geometry and boundary conditions for the identification test models: a) full microscale structure, b) full macroscale homogeneous structure.

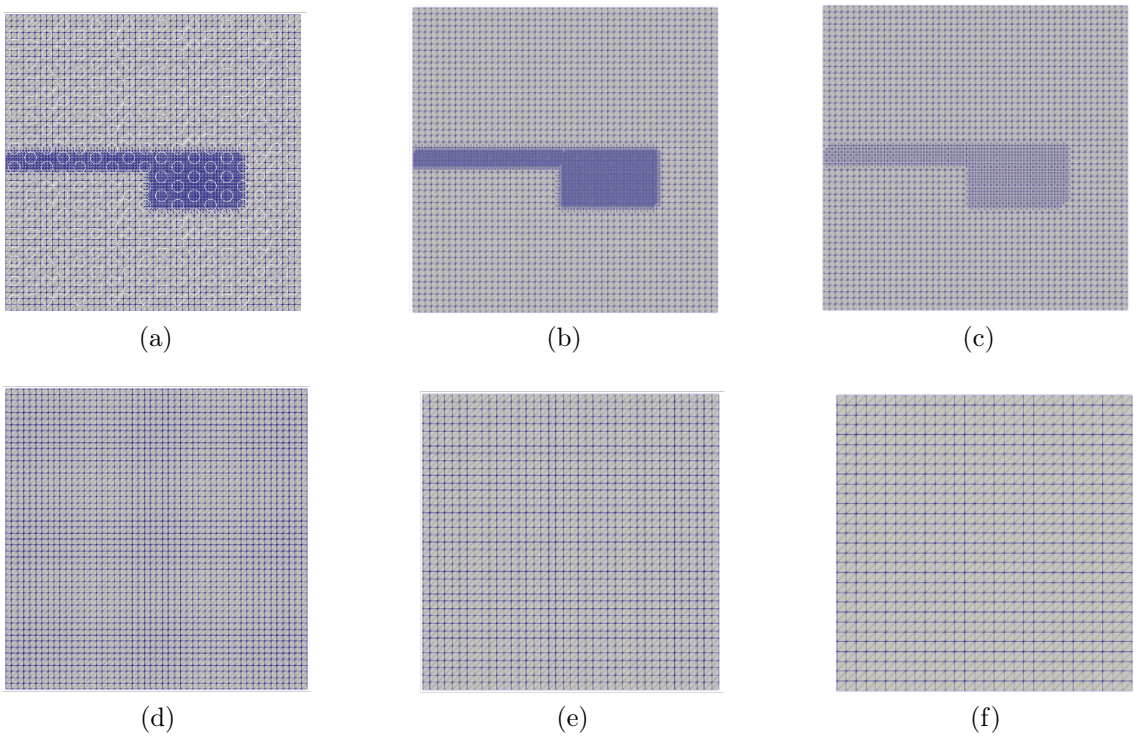

Figure 4.16: Computational meshes: a) Full fine scale CutFEM reference model ($h_{min} = 0.007$), b) Macroscale FEM with $h_{min} = 0.007$, c) Macroscale FEM with $h_{min} = 0.014$, d) Macroscale FEM with $h_{min} = 0.028$, e) Macroscale FEM with $h_{min} = 0.035$ and f) Macroscale FEM with $h_{min} = 0.047$.

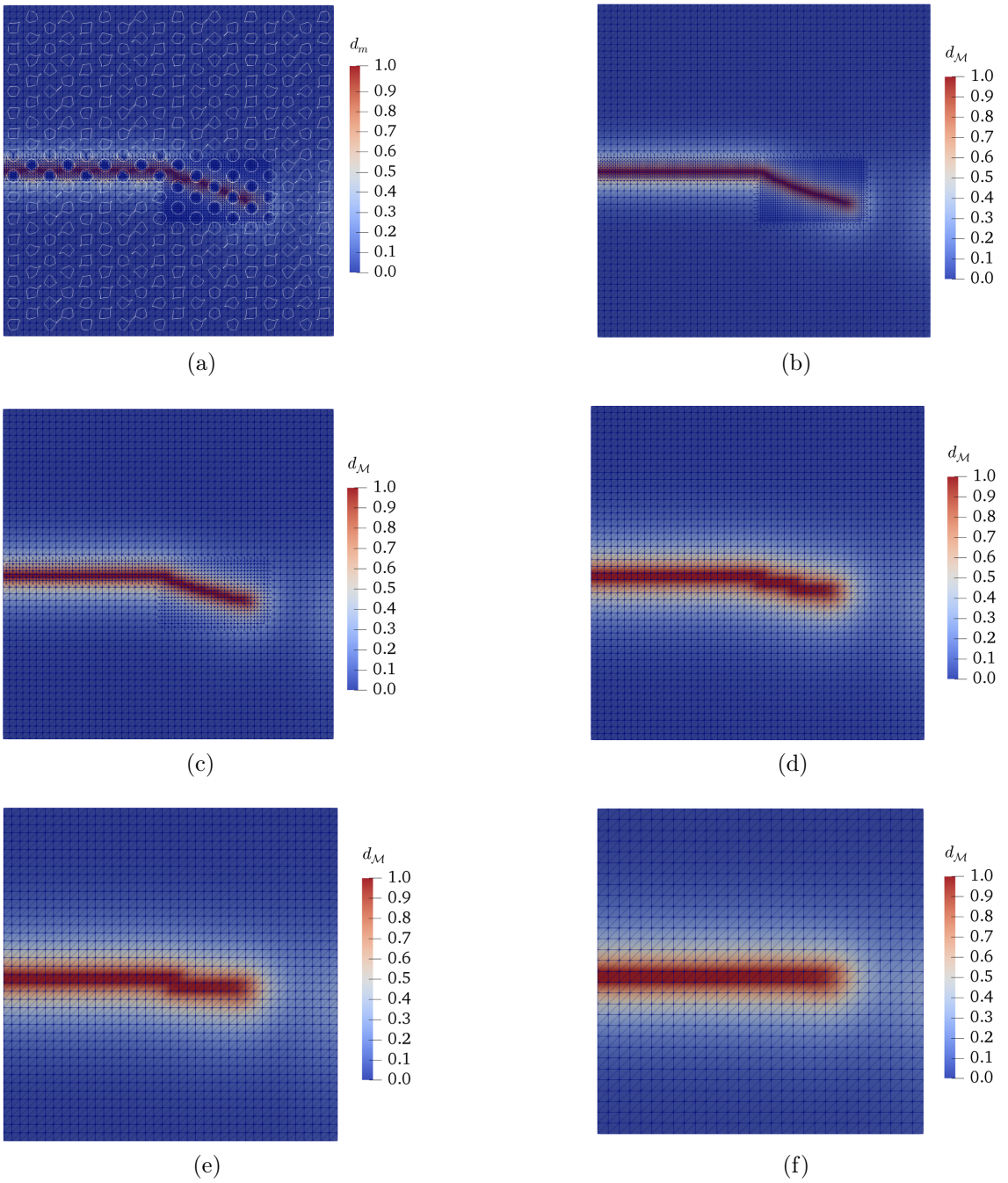

Figure 4.17: Phase field contour for the last time step: a) Full fine scale CutFEM reference model ($h_{min} = 0.007$), b) Macroscale FEM with $h_{min} = 0.007$, c) Macroscale FEM with $h_{min} = 0.014$, d) Macroscale FEM with $h_{min} = 0.028$, e) Macroscale FEM with $h_{min} = 0.035$ and f) Macroscale FEM with $h_{min} = 0.047$.

Validation tests. Previously, we showed that the fracture parameter $\ell_{\mathcal{M}}$ is highly dependent on the macroscale mesh size ($h_{\mathcal{M}}$). However, we intend to carry our further investigations over the relationship between $h_{\mathcal{M}}$ and $\ell_{\mathcal{M}}$ by using the derived values of $g_{\mathcal{M}}^{opt}$ and $\ell_{\mathcal{M}}^{opt}$ in a new problem. This way, we can ensure that our results are general and not problem-dependent. Therefore, here, we use the material and fracture parameters from the previous example in a new problem shown schematically in Figure 4.18a. This example has double initial cracks on each side of the structure and is under tension loading over the top edge. Moreover, we keep the mesh sizes similar to the identification tests (see Figure 4.19).

The mechanical tension tests are done for the reference and homogenised models (shown in Figure 4.18a, b, respectively) with the fracture parameters captured from identification tests. The corresponding phase field results in Figure 4.20b-d show that the inputs $g_{\mathcal{M}}^{opt}$ and $\ell_{\mathcal{M}}^{opt}$ work effectively in the new sample, when they are compared with the corresponding reference result in Figure 4.20a. We also achieve the same level of accuracy in the force-displacement curves that are shown in Figure 4.21. These results show that the derived values for the $g_{\mathcal{M}}^{opt}$ and $\ell_{\mathcal{M}}^{opt}$ from the previous example can be employed for new examples, as long as the microstructure, properties and $h_{\mathcal{M},min}$ (shown with h_{min} in the corresponding Figures) do not change. Thus, we identify the parameters $g_{\mathcal{M}}^{opt}$ and $\ell_{\mathcal{M}}^{opt}$ as "material properties", which is also consistent with results of authors in [186].

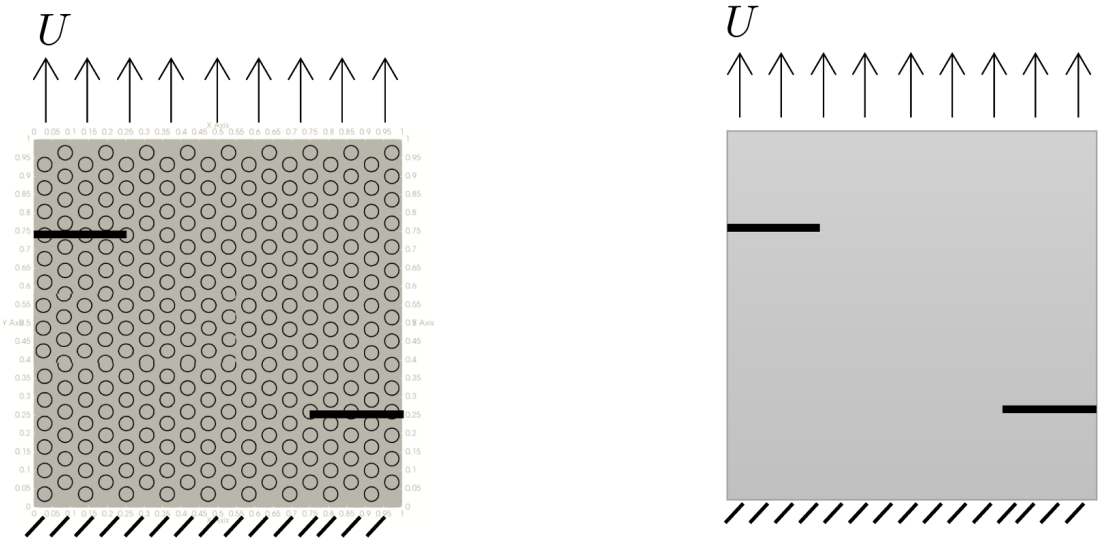

(a) (b)

Figure 4.18: Schematic presentation for the verification test models: a) full microscale heterogeneous structure and b) full macroscale homogeneous structure.

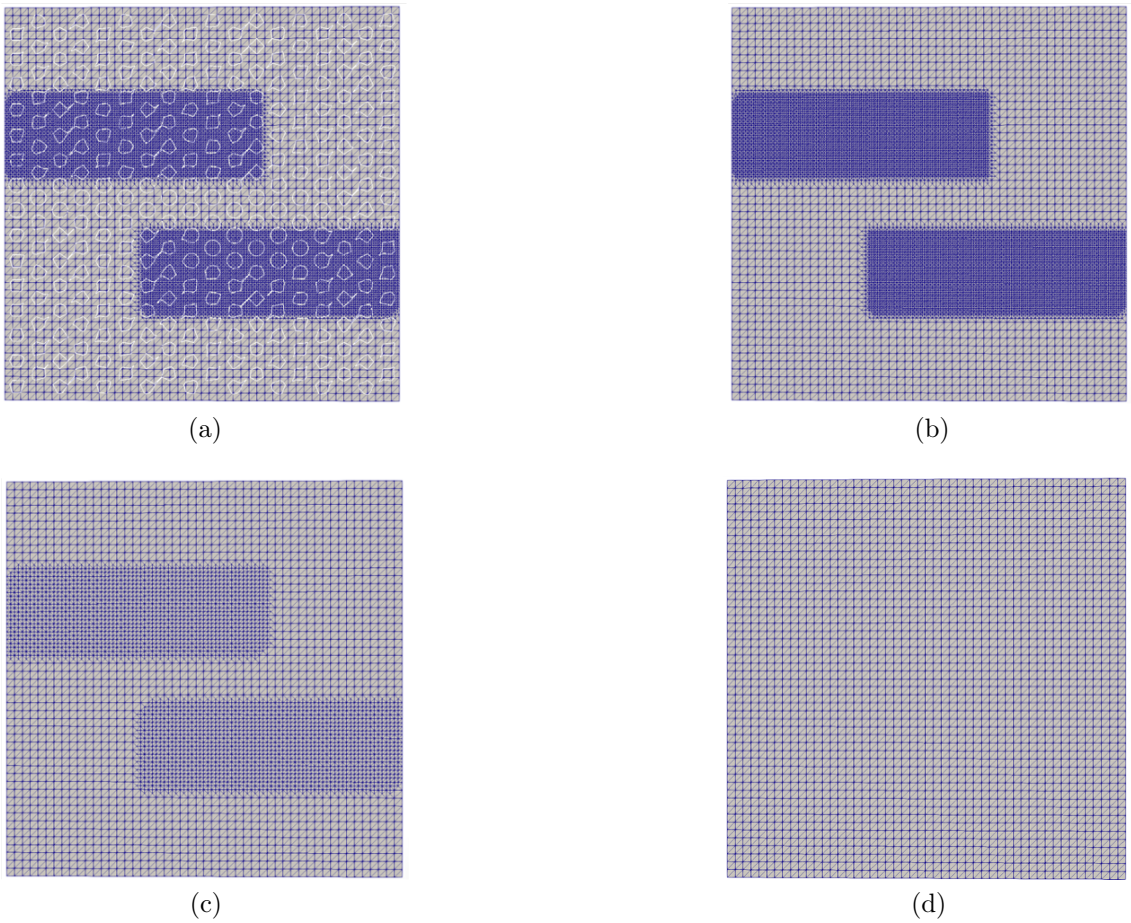

(a) (b)

(c) (d)

Figure 4.19: Computational meshes used for validation tests: a) Full fine scale CutFEM reference model with $h_{min} = 0.007$, b) macroscale FEM with $h_{min} = 0.007$, c) macroscale FEM with $h_{min} = 0.014$ and d) macroscale FEM with $h_{min} = 0.028$.

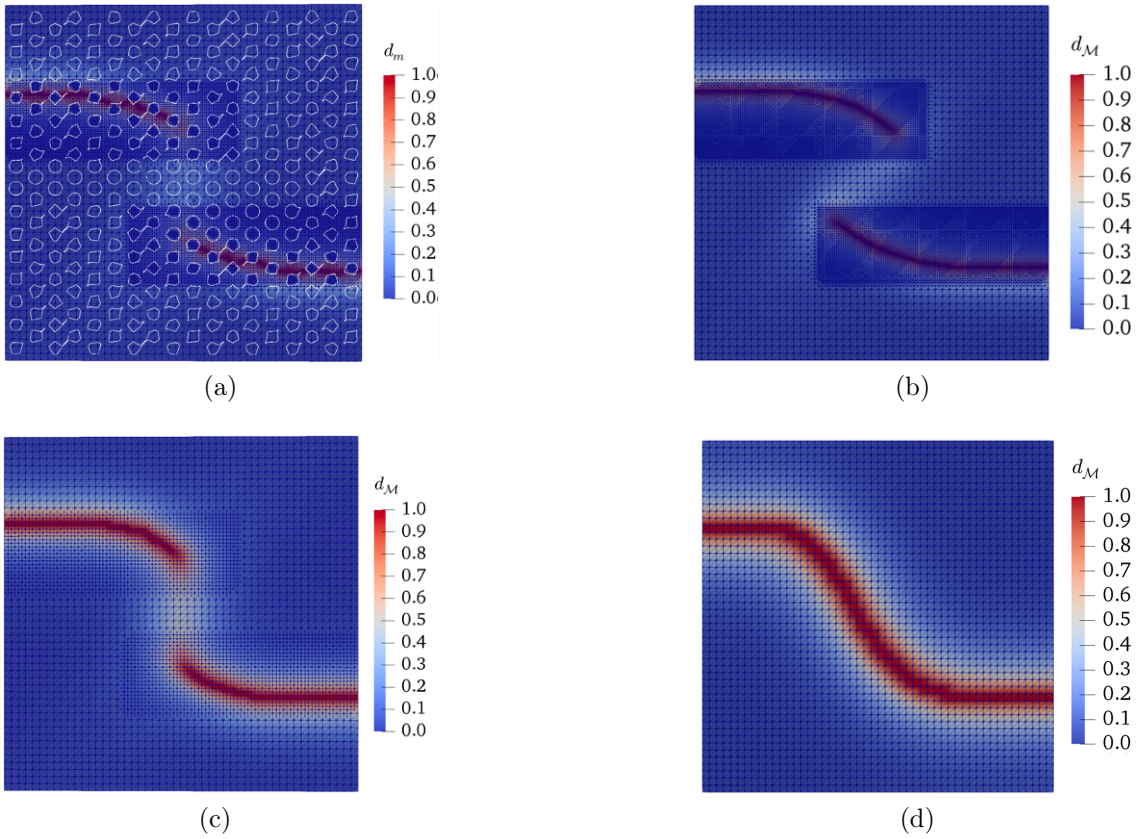

Figure 4.20: Phase field contour for the last time step: a) Full fine scale CutFEM reference model ($h_{min} = 0.007$), b) macroscale FEM with $h_{min} = 0.007$, c) macroscale FEM with $h_{min} = 0.014$ and d) macroscale FEM with $h_{min} = 0.028$.

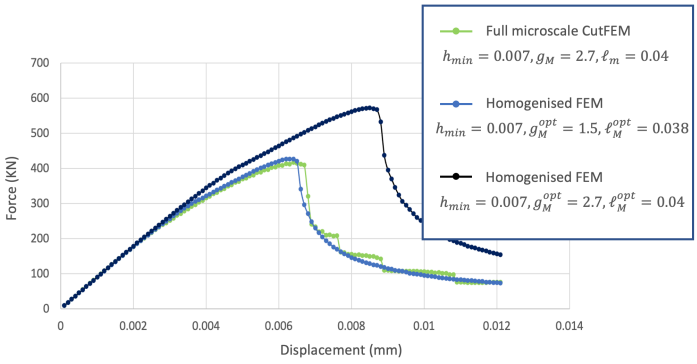

(a)

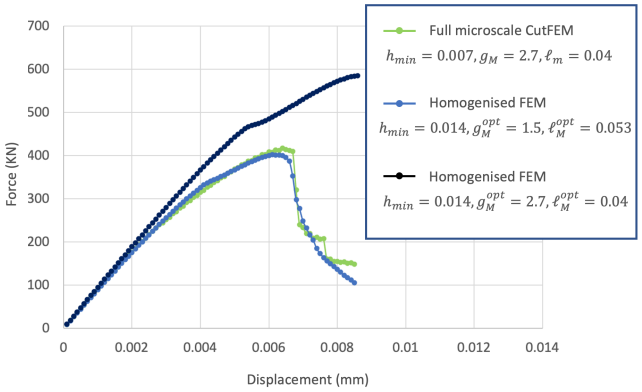

(b)

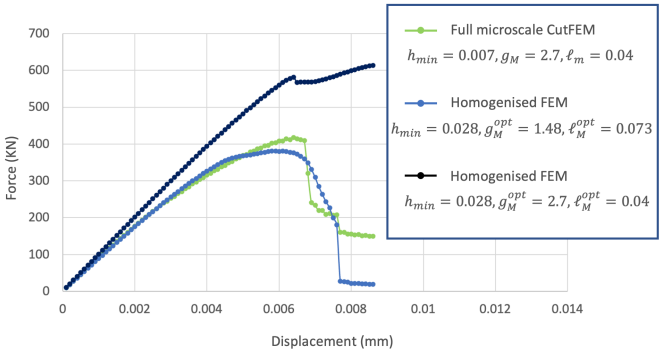

(c)

Figure 4.21: Force-displacement curves of tension tests for different inverse problems analysis carried out between heterogeneous and homogeneous structures. The homogeneous model properties changes as following in each analysis: a) $h_{min} = 0.007$, $g_{\mathcal{M}}^{opt} = 1.50$, $\ell_{\mathcal{M}}^{opt} = 0.038$, b) $h_{min} = 0.014$, $g_{\mathcal{M}}^{opt} = 1.50$, $\ell_{\mathcal{M}}^{opt} = 0.053$ and c) $h_{min} = 0.028$, $g_{\mathcal{M}}^{opt} = 1.48$ and $\ell_{\mathcal{M}}^{opt} = 0.073$.

4.3.1.2 Effect of microstructure on homogenisation

In this section, we investigate the effect of microstructural morphology on the homogenisation of the fracture parameters. The microstructure will change with respect to the pores' size (radius) while the structure's porosity is kept unaltered. The properties and boundary conditions are also the same as in the previous example. The shear test is carried out for three different microstructures that own the following radius of pores: $r_1 = 0.02$, $r_2 = 0.03$ and $r_3 = 0.04$. The corresponding computational meshes for the three microscale models and the homogenised macroscale model are shown in Figure 4.22, where the mesh size is the same for all samples.

The inverse problem analysis for each microscale model is carried out to find the homogenised fracture parameters. We report the corresponding results in table 4.2. The results show that the variation in the pore's size does not affect the $g_{\mathcal{M}}$. On the other hand, $\ell_{\mathcal{M}}$ shows dependency and tends to increase for bigger pores.

The phase fields for the microscale and macroscale models are shown in Figure 4.23. In all three different microstructures, the trend of homogenised phase fields is very similar to the corresponding microscale reference models.

r	$g_{\mathcal{M}}^{opt}$	$\ell_{\mathcal{M}}^{opt}$
0.02	1.50	0.038
0.03	1.51	0.056
0.04	1.54	0.092

Table 4.2: Optimised values for the $g_{\mathcal{M}}$ and $\ell_{\mathcal{M}}$ of inverse problem analysis between full microscale and full macroscale models.

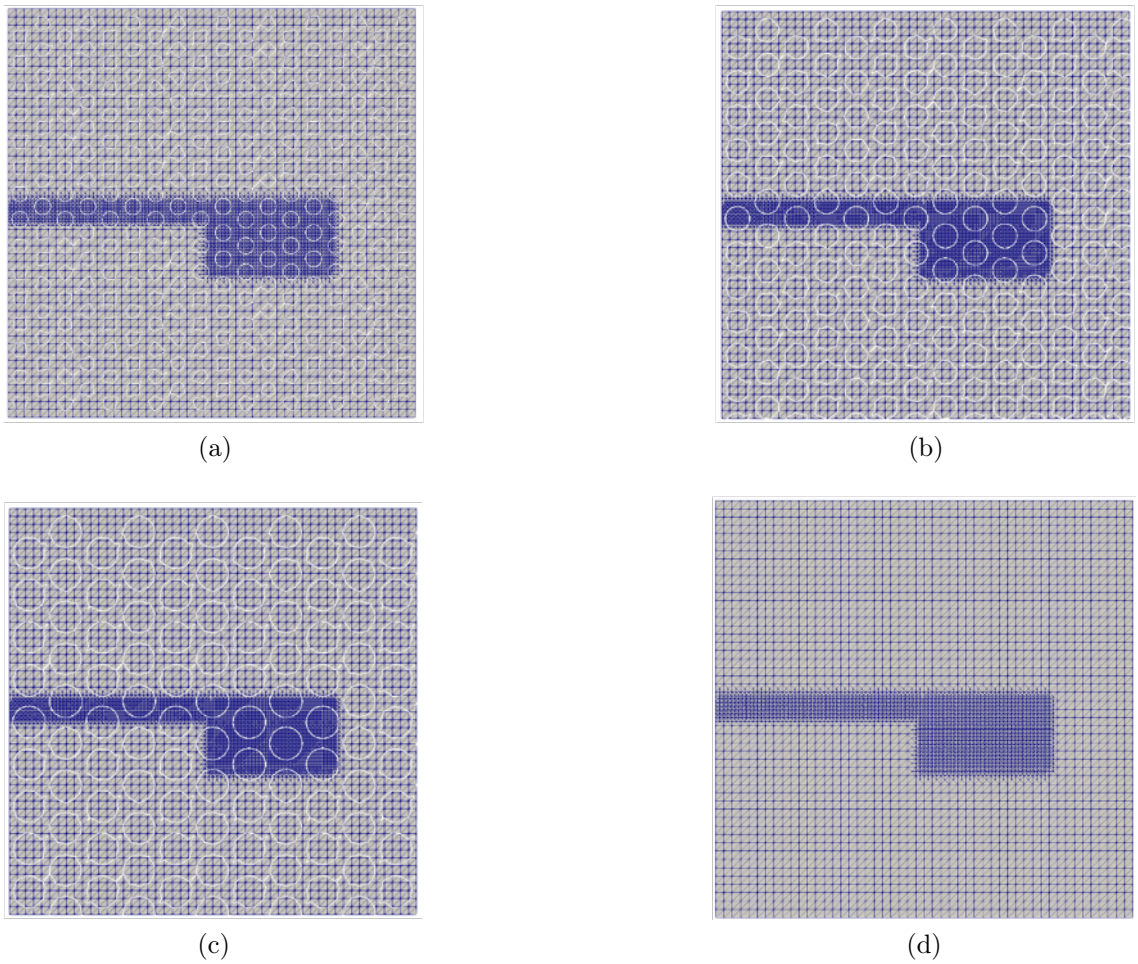

(a) (b)

(c) (d)

Figure 4.22: Computational meshes for heterogeneous and homogeneous structures, with $h_{min} = 0.007$ for all cases: a) heterogeneous structure with $r = 0.02$, b) heterogeneous structure with $r = 0.03$, c) heterogeneous structure with $r = 0.04$ and d) homogeneous structure.

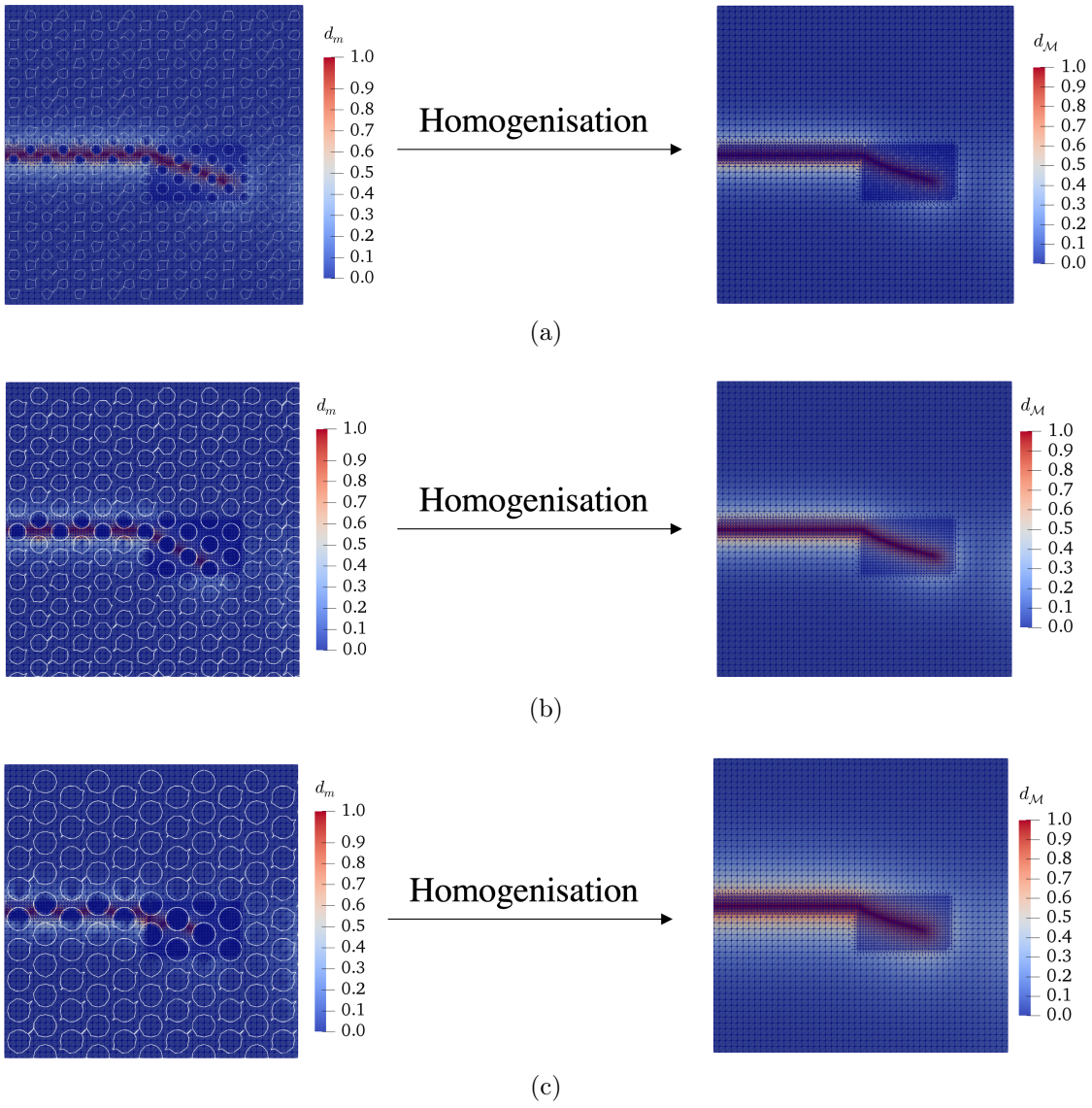

Figure 4.23: Phase fields for heterogeneous and homogenised models: a) $r = 0.02$, b) $r = 0.03$ and c) $r = 0.04$.

4.3.1.3 Effect of optimisation error functional on homogenisation

In the previous examples, the error functional used for the inverse problems was defined as an integral functional during the whole simulation time. However, performing a full-time simulation in each iteration of the inverse problem imposes high computational costs. In this section, the intention is to reduce the mentioned costs by replacing the previous error functional with a new functional that mainly depends on the maximum stress and then investigate if we can reach the same level of accuracy. The new error functional is defined as

$$J = \left[\frac{\sigma_m^{max} - \sigma_{\mathcal{M}}^{max}}{\sigma_m^{max}}\right]^2 + \left[\frac{u_m - u_{\mathcal{M}}}{u_m}\right]^2 \tag{4.37}$$

where σ_m^{max} and $\sigma_{\mathcal{M}}^{max}$ are the maximum stresses for full microscale and homogenised models, respectively. Also, u_m and $u_{\mathcal{M}}$ are the microscale and macroscale displacements corresponding the σ_m^{max} and $\sigma_{\mathcal{M}}^{max}$, respectively.

For identification purposes, the heterogeneous structure introduced in section 4.2.4.1 will be employed here. The same boundary conditions and properties will be used. Moreover, for mesh coarsening purposes, three different types of meshes are adopted for the macroscale model.

The inverse problem analysis with mesh coarsening is carried out, and the corresponding homogenisation results are shown in table 4.3.

$h_{\mathcal{M},min}$	$g_{\mathcal{M}}^{opt}$	$\ell_{\mathcal{M}}^{opt}$
0.007	1.70	0.051
0.014	1.69	0.052
0.028	1.41	0.066
0.035	2.16	0.070

Table 4.3: Optimised values for the $g_{\mathcal{M}}$ and $\ell_{\mathcal{M}}$ of inverse problem analysis between full microscale and full macroscale models.

For each set of optimised values of the $g_{\mathcal{M}}$ and $\ell_{\mathcal{M}}$, the corresponding phase field contour in the last time step of the simulation is reported in Figure 4.24. The results show that the new cost functional can lead to accurate homogenised $g_{\mathcal{M}}$ and $\ell_{\mathcal{M}}$,

which is a more versatile approach in terms of computational costs.

For further analysis, a mesh coarsening for this cost functional is carried out. When the results are compared with the results of section 4.3.1.1, we observe that we can achieve a reasonable range of results up to four times in the mesh coarsening. With the new error functional, the time required for the homogenisation of fracture parameters reduces up to 60%, which is very satisfactory against about 10% compromise in the accuracy. The force-displacement curves for the heterogeneous and homogeneous structures in Figure 4.25 illustrate that the captured optimised values of $g_{\mathcal{M}}$ and $\ell_{\mathcal{M}}$ for different $h_{\mathcal{M},min}$ can also produce accurate global responses.

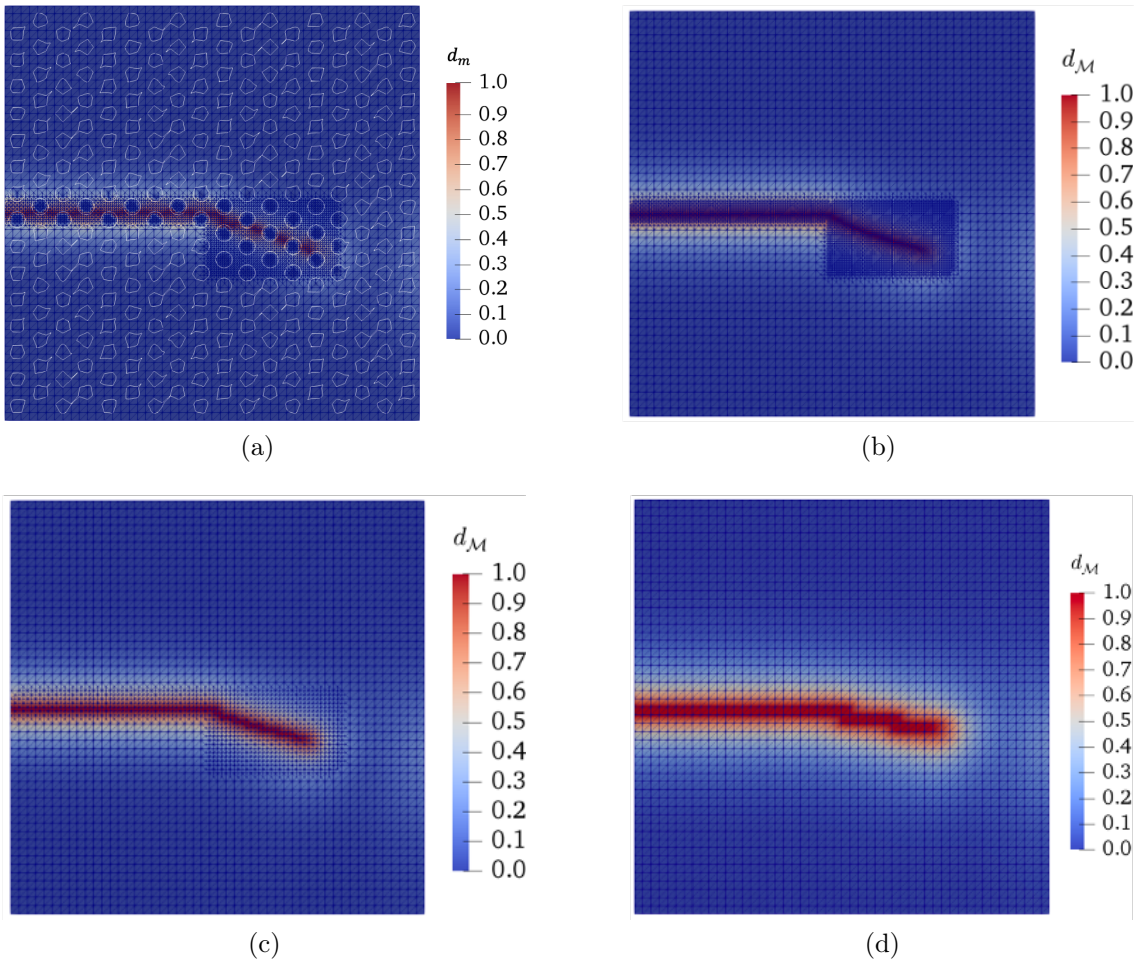

Figure 4.24: Phase field contours for the last time step: a) Full fine scale CutFEM reference model ($h_{min} = 0.007$), b) Macroscale FEM with $h_{min} = 0.007$, c) Macroscale FEM with $h_{min} = 0.014$, d) Macroscale FEM with $h_{min} = 0.028$.

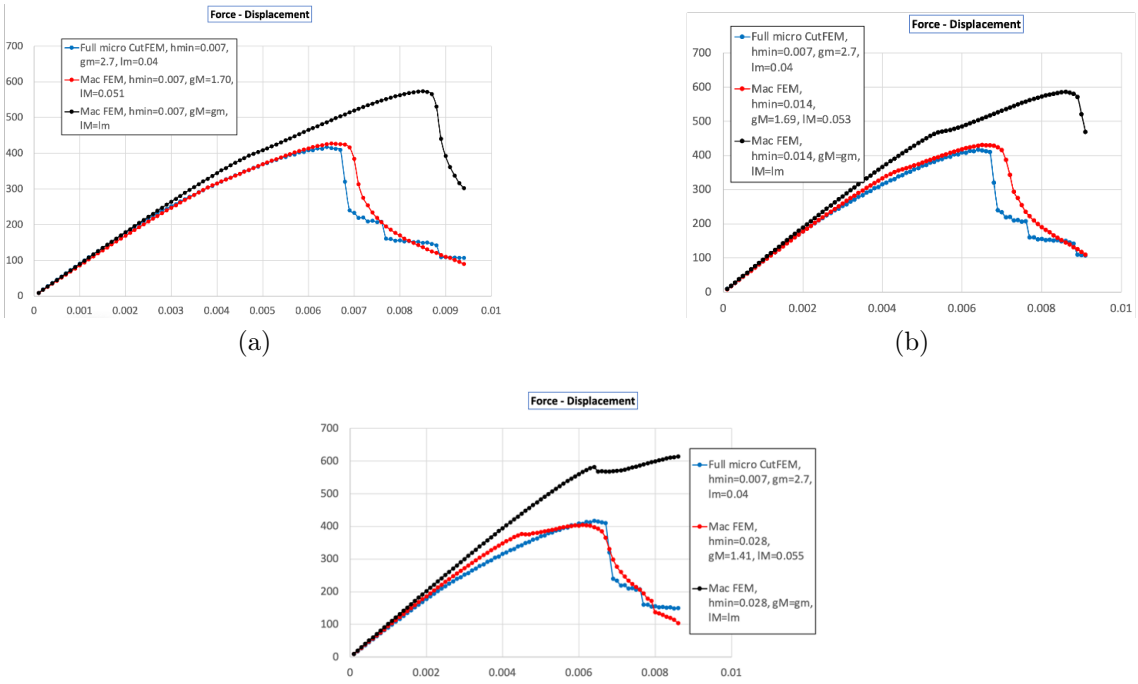

Figure 4.25: Force-displacement curves of shear tests for different inverse problems carried out between heterogeneous and homogeneous structures. The heterogeneous model (as reference) has the following properties for all of the inverse problems: $h_{m,min} = 0.007$, $g_m = 2.7$ and $\ell_m = 0.04$. The homogeneous model properties alters as following in each analysis: a) $h_{\mathcal{M},min} = 0.007$, $g^{opt}_{\mathcal{M}} = 1.7$, $\ell^{opt}_{\mathcal{M}} = 0.051$, b) $h_{\mathcal{M},min} = 0.014$, $g^{opt}_{\mathcal{M}} = 1.69$, $\ell^{opt}_{\mathcal{M}} = 0.053$ and c) $h_{\mathcal{M},min} = 0.028$, $g^{opt}_{\mathcal{M}} = 1.41$ and $\ell^{opt}_{\mathcal{M}} = 0.055$

.

4.4 Conclusion

This chapter explored two different categories of multiscale simulations for phase field problems. In the first category, the smoothed concurrent multiscale framework developed in chapter 3 was extended and validated for phase field problems with predetermined homogenised fracture parameters. The framework was also extended within a new self-consistent approach for predicting macroscale fracture parameters. In the new self-consistent framework, an inverse problem was developed between two models; (i) the concurrent multiscale model (as a reference model) and (ii) the macroscale homogenised model. This framework allowed us to use only a small portion of the microstructure and compute the homogenised values of the $g_{\mathcal{M}}$ and $\ell_{\mathcal{M}}$ within acceptable accuracy. These two frameworks were successfully verified for 2D phase field problems.

In the second part of the chapter, additional investigations on the homogenisation of fracture parameters were carried out following the work by [186]. Here, the effects of various parameters (including mesh-coarsening and types of microstructure and cost functional) over the homogenisation were studied. This investigation shed more light on the properties of homogenised fracture parameters that can be used as an input in domain decomposition methods. The investigations were carried out mainly in two parts: the first part covered the identification tests for the $g_{\mathcal{M}}^{opt}$ and $\ell_{\mathcal{M}}^{opt}$, where an inverse problem analysis between two models of micro and macro scale was carried out. The second part discussed the verification stage using the identified parameters in a new problem and ensuring that they can still reproduce accurate results.

The results of the mesh-coarsening investigation showed that the value of $h_{\mathcal{H}}$ in the homogenised model has a large impact on the value of $\ell_{\mathcal{M}}$ and negligible effect on the value of $g_{\mathcal{M}}$. The results also proved that $g_{\mathcal{M}}$ and $\ell_{\mathcal{M}}$ are material properties and can be used directly in new problems that own different settings or boundary conditions. Regarding the effect of microstructure on the homogenisation values, our results depicted that the changes in the pore's size have no impact on the computed $g_{\mathcal{M}}$. However, it largely affects the value of $\ell_{\mathcal{M}}$, where with an increase in the radius of pores, $\ell_{\mathcal{M}}$ also tends to increase. In the last section, we studied the effect of

optimisation error functional on the homogenisation parameters. We showed that the type of error functional has a huge impact on the computational costs of inverse problems and should be considered carefully. Our new error functional reduced the time required for the homogenisation of fracture parameters up to 60% by only compromising 10% in the accuracy of results, which can be considered satisfactory.

Chapter 5

Unfitted hierarchical multi-resolution analysis based on CutFEM

5.1 Introduction

This chapter deals with another novel concurrent multiscale method based on CutFEM. In this contribution, the microscale and macroscale subdomains are separated over a multi-resolution background mesh with a sharp interface which is not meshed [195]. Like chapter 3, we use CutFEM to discretise inside zoom regions with microscale features and to discretise the macroscale region, which is homogenised. However, unlike chapter 3, where a smooth interface was proposed to separate the two models, we employ a sharp interface and refine the elements inside the zooms hierarchically. We present the microstructure and the zooming interfaces with two sets of level set functions in the context of CutFEM. Then, the interfaces are allowed to intersect the multiresolution background mesh arbitrarily. This gives us an advantage of geometrical flexibility and enables us to (re)locate the zooms in a fully mesh-independent way.

The remainder of this chapter is structured as follows: Section 5.2 discusses the governing equations of the concurrent multiscale method. Herein, we first define the partitioned domain considered for our multiscale simulation framework. Then,

we present the strong and weak forms of equations for the heterogeneous microscale and the homogenised macroscale models. Eventually, we propose our concurrent multiscale framework in the discretisation stage. In this stage, we employ CutFEM to discretise the computational domain and then couple the micro and macro models with the Nitsche technique.

In the last section (section 5.3), we present the numerical results of the concurrent multiscale framework. We verify the performance of the framework with respect to reference models and then test it for more complicated examples with linear elastic and plastic materials.

5.2 Governing equations of the hierarchical multi-scale CutFEM

5.2.1 Computational domain partitioning of multiscale analysis framework

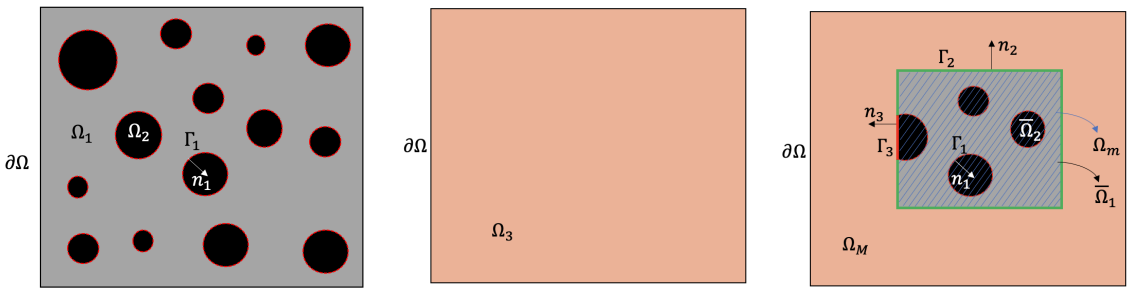

Figure 5.1: Domain partitioning: (a) heterogeneous microscale model, (b) homogeneous macroscale model and (c) multiscale model (the macroscale model enriched with a zoom including microscale model)

Let us consider that we have a two-phase composite material occupying domain Ω with boundary $\partial\Omega$, which consists of a matrix-phase Ω_1 and an inclusion phase Ω_2 (see Figure 5.1a). Here, $\Omega_1 \cup \Omega_2 = \Omega$ and $\Omega_1 \cap \Omega_2 = \emptyset$. The interface between Ω_1 and

Ω_2 is denoted by Γ_1. Furthermore, let us assume that the two-phase composite can be represented by a homogenised material, which we denote by Ω_3 (see Figure 5.1b). Now, let us introduce zooms in the homogenised domain into the two-phase composite material. The zoom regions are denoted by $\Omega_m = \bar{\Omega}_1 \cup \bar{\Omega}_2$, where $\bar{\Omega}_i$, $i = 1, 2$, defines the part of Ω_i that lies inside the zoom regions (microscale domain). And $\Omega_{\mathcal{M}} = \Omega_3 \setminus \Omega_m$ denotes the homogenised region without the zoom regions (macroscale domain). The interface between the matrix phase of the zoom regions and the macroscale domain is denoted by $\Gamma_2 = \bar{\Omega}_1 \cap \Omega_{\mathcal{M}}$ and the interface between the inclusion phase and the macroscale domain is denoted by $\Gamma_3 = \bar{\Omega}_2 \cap \Omega_{\mathcal{M}}$ (see Figure 5.1c).

5.2.2 Heterogeneous elasticity problem: strong form

5.2.2.1 Semi-discrete boundary value problem

The semi-discrete problem of elasticity that we wish to solve is the following. Time interval $\mathcal{I} = [0\, T]$ into N equally spaced time intervals. At discrete times in $\mathcal{I}_{\Delta T} = \{t_1 = \Delta T, t_2 = 2\Delta T, \ldots, t_N = N\Delta T = T\}$, we look for displacement $u^n := \{u_1^n, u_2^n\} : \Omega_1 \times \Omega_2 \to \mathbb{R}^D \times \mathbb{R}^D$ at n^{th} time step satisfying,

$$\forall\, i \in \{1, 2\}, \qquad \operatorname{div} \sigma_i^n(\nabla_s u_i) + f_b^n = 0 \qquad \text{in}\, \Omega_i\,. \tag{5.1}$$

where $\sigma_i^n(\nabla_s u_i^n)$ is the stress tensor, which is a function of strain tensor $\nabla_s u_i^n$, and f_b^n is the corresponding body force.

The boundary conditions of the elasticity problem are

$$\forall\, i \in \{1, 2\}, \qquad u_i^n = u_d^n \qquad \text{over}\ \partial\Omega_u \cap \partial\Omega_i \tag{5.2}$$

and

$$\forall\, i \in \{1, 2\}, \qquad \sigma_i(\nabla_s u_i^n) \cdot n_{\partial\Omega} = \tau^n \qquad \text{over}\ \partial\Omega_t \cap \partial\Omega_i \tag{5.3}$$

where τ^n denotes the traction vector and $n_{\partial\Omega}$ is the outer normal to the boundary. Here, $\partial\Omega = \partial\Omega_t \cup \partial\Omega_u$, $\partial\Omega_t \cap \partial\Omega_u = \emptyset$. The fields f_b^n, u_d^n and t_d^n are given time-discrete

fields.

Linear elasticity If we assume that the two phases of the composite are linear elastic, time-independent and homogeneous, the stress functions σ_i^n may be expressed as

$$\forall\, i \in \{1,2\}, \qquad \sigma_i^n(\nabla_s u_i^n) := D_i : \nabla_s u_i^n \qquad \text{in}\, \Omega_i\,, \tag{5.4}$$

where $\nabla_s\,.\, = \frac{1}{2}(\nabla\,.\, + \nabla^T\,.\,)$ and D_i is the fourth-order Hooke tensor of the material occupying phase i. This tensor may be expressed as a function of the the Lamé coefficients λ_i and μ_i as follows:

$$\forall\, i \in \{1,2\}, \qquad D_i : \nabla_s\,.\, = \lambda_i \mathrm{Tr}(\nabla_s\,.\,)\mathbb{I} + 2\mu_i \nabla_s\,.\,. \tag{5.5}$$

von Mises Plasticity We consider the following von Mises plasticity model. The stress s in the material is given by

$$s = D : (\varepsilon - \varepsilon) \tag{5.6}$$

as a function of the strain ε (*i.e.* the symmetric part of the displacement gradient) and the plastic strain ε_p. The yield surface is defined as

$$f(s_D, q, p) = \sqrt{\frac{3}{2}(s_D - q) : (s_D - q)} - (Y_0 + R(p)) \tag{5.7}$$

where s_D denotes the deviatoric part of σ, p denotes the cumulative plastic strain and q the back stress. In equation above, Y_0 is a constant initial yield parameter, the term $R(p) = \hat{H}\, p$ is the isotropic linear hardening function, where $\hat{H}$ is the corresponding hardening modulus. Moreover, the plasticity flow rules are as follows:

$$\lambda \geq 0\,, \qquad \lambda f(s_D, q, p) = 0\,, \qquad f(s_D, q, p) \leq 0 \tag{5.8}$$

$$\begin{aligned}
\dot{\varepsilon}_p &= \lambda \left(\frac{s_D - q}{\|s_D - q\|} \right) , \\
\dot{q} &= \lambda \left(\bar{H} : \frac{s_D - q}{\|s_D - q\|} \right) , \\
\dot{p} &= \lambda \, .
\end{aligned} \tag{5.9}$$

where λ is the plastic multiplier and $\bar{H}$ is a fourth-order kinematic hardening tensor. In our examples, $\bar{H}$ will be vanishingly small (no kinematic hardening).

Implicit time integration The previous ODE may be discretised in time using an implicit Euler scheme. This leads to the following semi-discrete material law.

$$\begin{aligned}
&\frac{1}{\Delta T} \left(D^{-1} : s^{n+1} - \varepsilon^{n+1} + \varepsilon_p^n \right) + \lambda \frac{s_D^{n+1} - q^{n+1}}{\|s_D^{n+1} - q^{n+1}\|} = 0 \\
&\frac{1}{\Delta T} \left(\bar{H}^{-1} : (q^{n+1} - q^n) \right) + \lambda \frac{s_D^{n+1} - q^{n+1}}{\|s_D^{n+1} - q^{n+1}\|} = 0 \\
&\lambda \geq 0 \qquad \lambda f(s_D^{n+1}, q^{n+1}, p^n + \lambda \Delta T) = 0 \qquad f(s_D^{n+1}, q^{n+1}, p^n + \lambda \Delta T) \leq 0
\end{aligned} \tag{5.10}$$

Given $(\varepsilon^{n+1}, \varepsilon_p^n, q^n, p^n)$, the previous nonlinear system of equation (the last three constraints can be recast as a single nonlinear equality using the Heaviside function) can be solved for $(s^{n+1}, q^{n+1}, \lambda)$ using the usual combination of operator splitting and Newton iterative solution scheme. The update of internal variables is performed according to

$$\begin{aligned}
\varepsilon_p^{n+1} &= \varepsilon_p^n + \lambda \left(\frac{s_D^{n+1} - q^{n+1}}{\|s_D^{n+1} - q^{n+1}\|} \right) \Delta T \\
p^{n+1} &= p^n + \lambda \Delta T
\end{aligned} \tag{5.11}$$

The procedure can therefore be summarised as an (implicitly defined) relationship

$$s^{n+1} = s_{\Delta T} \left(\varepsilon^{n+1}, (\varepsilon_p^n, q^n, p^n); \mu, \Delta T \right) \tag{5.12}$$

where μ is a real-valued vector containing all the parameters of the constitutive law, Y_0, all the free parameters of tensor $\bar{H}$ and that of R.

Semi-discrete implicit stress functions At time $t_n > 0$, for any phase index $i \in \{1, 2\}$ of the composite material, we may replace the elastic constitutive law by the following nonlinear function

$$\sigma_i^n(\nabla_s u_i^n) = s_{\Delta T}\left(\nabla_s u_i^n, \xi_i^{n-1}; \mu_i, \Delta T\right) \tag{5.13}$$

where the field of past internal variables $\xi_i^{n-1} = (\varepsilon_p^{n-1}, q^{n-1}, p^{n-1})$ defined over Ω_i are sequentially and locally updated according to the procedure outlined above. We suppose that at the beginning of the simulation, all the internal variables are null.

5.2.2.2 Macroscale model with homogenised material

Here, we present a homogenised elasticity problem with an equivalent homogenised material for the two-phase composite material defined in the previous section. The corresponding computational domain is shown schematically in Figure 5.1b. Similar to the heterogeneous elasticity problem, we consider a time-dependent problem with time interval $\mathcal{I} = [0\ T]$ divided into N equal time steps. In each time step n, we look for displacement $u_3^n : \Omega_3 \to \mathbb{R}^D$ satisfying the following equilibrium equation

$$\operatorname{div} \sigma_3^n(\nabla_s u_3^n) + f_b^n = 0 \qquad \text{in } \ \Omega_3\,. \tag{5.14}$$

where the corresponding boundary conditions are as follows: $u_3^n = u_d^n$ over $\partial\Omega_u \cap \partial\Omega$ and $\sigma_3 \cdot n_{\partial\Omega} = \tau$ over $\partial\Omega_t \cap \partial\Omega$, where $\partial\Omega = \partial\Omega_t \cup \partial\Omega_u$ and $\partial\Omega_t \cap \partial\Omega_u = \{0\}$.

In Ω_3, we introduce a surrogate material model with slowly varying parameters in space. If the coarse material is elastic and homogeneous, it is characterized by constant tensor D_3 (which may be obtained, for instance, via some form of homogenisation of the composite material), whose action reads as

$$D_3 : \nabla_s\,. = \lambda_3 \mathrm{Tr}(\nabla_s\,.)\mathbb{I} + 2\mu^c \nabla_s\,. \tag{5.15}$$

The resulting stress function is

$$\sigma_3(\nabla_s u_3) := D_3 : \nabla_s u_3 \qquad \text{in } \Omega_3\,. \tag{5.16}$$

If the coarse material is plastic, we define the associated stress update at the n^{th} time increment, $n \in \{1, 2, ..., N\}$, by

$$\sigma_3^n(\nabla_s u_3^n) = s_{\Delta T}\left(\nabla_s u_3^n, \xi_3^{n-1}; \mu_3, \Delta T\right). \tag{5.17}$$

The solution approach for equation above is similar to the approach presented for heterogeneous plasticity problems in the previous section.

5.2.3 Multiresolution problem in weak form

In this section, we are going to introduce the weak formulation of our multiresolution problem. As mentioned above, we split our background domain Ω into two non-overlapping domains: the fine domain Ω_m and the coarse domain $\Omega_{\mathcal{M}}$, as shown in Figure 5.1c.

In the following, we present the weak form of governing equations for the microscale and macroscale problems separately. However, due to the concurrent multiscale modelling, both problems will be solved simultaneously.

5.2.3.1 Microscale model in weak form

Now, the microscale problem of elasticity at time $t_n \in \mathcal{I}_{\Delta T}$ reads: We look for a displacement field $u_m := \{u_1, u_2\} : \bar{\Omega}_1 \times \bar{\Omega}_2 \to \mathbb{R}^D \times \mathbb{R}^D$ satisfying

$$a_m(u_m, v_m) + a_{m,\sharp}(u_m, v_m) = l_m(v_m) \tag{5.18}$$

In the previous variational statement, arbitrary $v_m := \{u_1, u_2\} : \bar{\Omega}_1 \times \bar{\Omega}_2 \to \mathbb{R}^D \times \mathbb{R}^D$ is required to satisfy the homogeneous Dirichlet conditions

$$v_m = 0 \qquad \text{over} \qquad \partial\Omega_{m,u} := \partial\Omega_u \cap \partial\Omega_m \tag{5.19}$$

In Equation 5.18, the bilinear form a_m is defined as,

$$a_m(u_m, v_m) = \int_{\Omega_m} \sigma_m(\nabla_s u_m) : \nabla_s v_m \, dx\,, \tag{5.20}$$

The corresponding linear form l_m is given by,

$$l_m(v_m) = \int_{\Omega_m} f_b \cdot v_m \, dx + \int_{\partial\Omega_{m,t}} \tau \cdot v_m \, dx \,, \tag{5.21}$$

where

$$\Omega_{m,t} = \Omega_m \cap \partial\Omega_t \tag{5.22}$$

The bilinear form $a_{m,\sharp}$ in Equation 5.18 introduces the coupling terms related to the Nitsche's method to glue together the microscale sub-domains, i.e. $\bar{\Omega}_1$ and $\bar{\Omega}_2$, and is expressed as,

$$\begin{aligned} a_{m,\sharp}(u_m, v_m) &= \gamma_1 \hat{w}_1 \int_{\Gamma_1} [\![u_m]\!]_1 \cdot [\![v_m]\!]_1 \, dx \\ &- \int_{\Gamma_1} \{t\}_1 (u_m) \cdot [\![v_m]\!]_1 \, dx \\ &- \int_{\Gamma_1} \{t\}_1 (v_m) \cdot [\![u_m]\!]_1 \, dx \,. \end{aligned} \tag{5.23}$$

where

$$[\![u_m]\!]_1 = u_1 - u_2 \tag{5.24}$$

which denotes the jump in the displacement field across Γ_1. In Equation 5.23, $\gamma_1 > 0$, $\hat{w}_1$ and $\{t\}_1$ are Nitsche related parameters for the microscale model that will be defined in the discretisation stage.

5.2.3.2 Macroscale model in weak form

Now, for the macroscale problem of elasticity at time $t_n \in \mathcal{I}_{\Delta T}$ reads, we look for a displacement field $u_{\mathcal{M}} : \Omega_{\mathcal{M}} \to \mathbb{R}^D$ satisfying

$$a_{\mathcal{M}}(u_{\mathcal{M}}, v_{\mathcal{M}}) + a_{\mathcal{M},\sharp}(u_{\mathcal{M}}, v_{\mathcal{M}}) = l_{\mathcal{M}}(v_{\mathcal{M}}) \tag{5.25}$$

where the trial function $v_{\mathcal{M}} : \Omega_{\mathcal{M}} \to \mathbb{R}^D$ is required to satisfy the homogeneous Dirichlet conditions

$$v_{\mathcal{M}} = 0 \qquad \text{over } \partial\Omega_{\mathcal{M},u} := \partial\Omega_u \cap \partial\Omega_{\mathcal{M}} \tag{5.26}$$

The bilinear form $a_{\mathcal{M}}$ in equation 5.25 is defined as follows,

$$a_{\mathcal{M}}(u_{\mathcal{M}}, v_{\mathcal{M}}) = \int_{\Omega_{\mathcal{M}}} \sigma_{\mathcal{M}}(\nabla_s u_{\mathcal{M}}) : \nabla_s v_{\mathcal{M}} \, dx, \tag{5.27}$$

The corresponding linear form $l_{\mathcal{M}}(u_{\mathcal{M}}, v_{\mathcal{M}})$ is defined as,

$$l_{\mathcal{M}}(v_{\mathcal{M}}) = \int_{\Omega_{\mathcal{M}}} f_b \cdot v_{\mathcal{M}} \, dx + \int_{\partial\Omega_{\mathcal{M},t}} \tau \cdot v_{\mathcal{M}} \, dx \,, \tag{5.28}$$

where

$$\partial\Omega_{\mathcal{M},t} = \Omega_{\mathcal{M}} \cap \partial\Omega_t \tag{5.29}$$

The bilinear form $a_{\mathcal{M},\sharp}(u_{\mathcal{M}}, \delta u_{\mathcal{M}})$ presents the Nitsche's formulation for coupling microscale and macroscale models over two types of interfaces; Γ_2 and Γ_3, which is denoted by

$$a_{\mathcal{M},\sharp}(u_{\mathcal{M}}, v_{\mathcal{M}}) = a_{2,\sharp}(u_{\mathcal{M}}, v_{\mathcal{M}}) + a_{3,\sharp}(u_M, v_{\mathcal{M}}) \tag{5.30}$$

where for $i \in \{2, 3\}$, the Nitsche's formulation over Γ_i reads

$$\begin{aligned} a_{i,\sharp}(u_{\mathcal{M}}, v_{\mathcal{M}}) &= \gamma_i \hat{w}_i \int_{\Gamma_i} [\![u_{\mathcal{M}}]\!]_i \cdot [\![v u_{\mathcal{M}}]\!]_i \, dx \\ &- \int_{\Gamma_i} \{t\}_i (u_{\mathcal{M}}) \cdot [\![v_{\mathcal{M}}]\!]_i \, dx \\ &- \int_{\Gamma_i} \{t\}_i (v_{\mathcal{M}}) \cdot [\![u_{\mathcal{M}}]\!]_i \, dx \,. \end{aligned} \tag{5.31}$$

where $\gamma_i > 0$, $\hat{w}_i$ and $\{t\}_i$ are Nitsche's terms and we have

$$[\![u_{\mathcal{M}}]\!]_i = u_{\mathcal{M}} - u_i \tag{5.32}$$

which denotes the jump in the displacement field across Γ_i.

5.2.4 Level-set-based descriptions of sub-domains and interfaces

In this contribution, we define sub-domains Ω_1 and Ω_2 implicitly via the values of a time-independent continuous level set function $\phi_1 \in \mathcal{C}^0(\Omega)$. More precisely, we suppose that

$$\begin{aligned} \Omega_1 &= \{x \in \Omega \,|\, \phi_1(x) \leq 0\} \\ \Omega_2 &= \{x \in \Omega \,|\, \phi_1(x) > 0\} \end{aligned} \quad . \tag{5.33}$$

Here, we define two sets of level set functions ϕ_1 and ϕ_2 and show how they describe the subdomains and interfaces in our multiresolution setting. The interface that separates the two subdomains is denoted by Γ_1 and given in terms of ϕ_1 by

$$\Gamma_1 = \{x \in \Omega \,|\, \phi_1(x) = 0\} \tag{5.34}$$

In the proposed multiresolution scheme, coarse domain $\Omega_{\mathcal{M}}$ is defined as

$$\Omega_{\mathcal{M}} = \{x \in \Omega \,|\, \phi_2(x) > 0\} \tag{5.35}$$

where $\phi_2 \in \mathcal{C}^0(\Omega)$ is a continuous level set function.

Similarly, fine domain Ω_m is defined as

$$\Omega_m = \{x \in \Omega \,|\, \phi_2(x) \leq 0\} \tag{5.36}$$

where Ω_m is comprised of micro pores (or micro inclusions) and matrix. The subdomain corresponding micro pores or inclusions inside the Ω_m is defined as

$$\bar{\Omega}_1 = \{x \in \Omega \,|\, \phi_1(x) \geq 0, \quad \phi_2(x) \leq 0\} \tag{5.37}$$

The subdomain corresponding matrix inside the Ω_m is defined as

$$\bar{\Omega}_2 = \{x \in \Omega \,|\, \phi_1(x) \leq 0, \quad \phi_2(x) \leq 0 \ \} \tag{5.38}$$

Now, we introduce the interface between different subdomains defined above. The

corresponding interface between coarse and fine domains is expressed by

$$\Gamma_{12} = \{x \in \Omega \,|\, \phi_2(x) = 0\} \tag{5.39}$$

The interface Γ_{12} is comprised of two separate interfaces; $\Gamma_{12} = \Gamma_2 \cup \Gamma_3$, which are defined as

$$\begin{array}{l} \Gamma_2 = \{x \in \Gamma_{12} \,|\, \phi_1(x) > 0\} \\ \Gamma_3 = \{x \in \Gamma_{12} \,|\, \phi_1(x) \leq 0\} \end{array} . \tag{5.40}$$

5.2.5 Discretisation of the multiresolution problem

5.2.5.1 Discretisation of the geometry

Let us introduce a coarse triangulation $\mathcal{T}^H$ of domain Ω. The tessellated domain is denoted by Ω^H. Furthermore, let us introduce the finite element space of continuous piecewise linear functions, *i.e.*

$$\mathcal{Q}^H := \{w \in \mathcal{C}^0(\Omega^H) : w|_K \in \mathcal{P}^1(K)\,, \forall K \in \mathcal{T}^H\} \tag{5.41}$$

We now define the finite element approximation of coarse domain $\Omega_{\mathcal{M}}$ as

$$\Omega^H_{\mathcal{M}} = \{x \in \Omega^H \,|\, \phi^H_2(x) \geq 0\} \tag{5.42}$$

where $\phi^H_2(x) \in \mathcal{Q}^H$ is the coarse nodal interpolant of ϕ_2.

Let us now introduce a hierarchical subtriangulation $\mathcal{T}^h$ of $\mathcal{T}^H$, with $h \ll H$. Due to the hierarchical structure, the union of all triangles of $\mathcal{T}^h$ is the coarse finite element domain $\mathcal{T}^H$. We define space

$$\mathcal{Q}^{(H,h)} := \{w \in \mathcal{C}^0(\Omega^H) : w|_K \in \mathcal{P}^1(K)\,, \forall K \in \mathcal{T}^h\} \tag{5.43}$$

With this definition, domains Ω_1 and Ω_2 are discretised as follows.

$$\begin{array}{l} \Omega_1^{(H,h)} = \{x \in \Omega^H \,|\, \phi^H_2(x) \leq 0,\, \phi^h_1(x) \leq 0\} \\ \Omega_2^{(H,h)} = \{x \in \Omega^H \,|\, \phi^H_2(x) \leq 0,\, \phi^h_1(x) \geq 0\} \end{array} . \tag{5.44}$$

We define the interface between the fine domains as

$$\Gamma_1^{(H,h)} = \{x \in \Omega^H \,|\, \phi_2^H(x) \leq 0,\, \phi_1^{(H,h)}(x) = 0\} \tag{5.45}$$

and the interfaces between the coarse and the fine domains as

$$\begin{aligned} \Gamma_{12}^H &= \{x \in \Omega^H \,|\, \phi_2^H(x) = 0\} \\ \Gamma_2^{(H,h)} &= \{x \in \Gamma_{12}^H \,|\, \phi_1^h(x) \leq 0\} \\ \Gamma_3^{(H,h)} &= \{x \in \Gamma_{12}^H \,|\, \phi_1^h(x) \geq 0\} \end{aligned} \tag{5.46}$$

Notice that finely discretised quantities are parametrised by a pair of mesh characteristics $\mathcal{H} = (H, h)$. This is due to the hierarchical structure of the multiresolution scheme that we have introduced (the coarse domain "overshadows" the composite material). To simplify the notations, the coarse sets and variables that only depend on H will also be written to be dependent on $\mathcal{H}$.

5.2.5.2 Overlapping domain decomposition

For the three different domains of the multiresolution scheme, we need to define appropriate extended domains. Such an extended domain is composed of all the elements that have a non-void intersection with its non-extended counterpart. Hence, the set of all elements of $\mathcal{T}^{\mathcal{H}}$ that have a non-zero intersection with $\Omega_{\mathcal{M}}^{\mathcal{H}}$ is

$$\hat{\mathcal{T}}_{\mathcal{M}}^{\mathcal{H}} := \{K \in \mathcal{T}^{\mathcal{H}} : K \cap \Omega_{\mathcal{M}}^{\mathcal{H}} \neq \emptyset\} \tag{5.47}$$

The fictitious domain domain corresponding to this set is $\hat{\Omega}_{\mathcal{M}}^{\mathcal{H}} := \bigcup_{K \in \hat{\mathcal{T}}_{\mathcal{M}}^{\mathcal{H}}} K$. Similarly for the fine domains,

$$\forall i \in \{1, 2\}, \qquad \hat{\mathcal{T}}_i^{\mathcal{H}} := \{K \in \mathcal{T}^{\mathcal{H}} : K \cap \Omega_i^{\mathcal{H}} \neq \emptyset\} \tag{5.48}$$

The domains corresponding to these sets are denoted by $\hat{\Omega}_i^{\mathcal{H}} := \bigcup_{K \in \hat{\mathcal{T}}_i^{\mathcal{H}}} K$, for $i = 1$ and for $i = 2$.

5.2.5.3 Extended interface FE spaces

We will look for an approximation $u^{\mathcal{H}} = \left(u_1^{\mathcal{H}}, u_2^{\mathcal{H}}, u_3^{\mathcal{H}}\right)$ of the multiresolution elasticity problem in space $\mathcal{U}^{\mathcal{H}} = \mathcal{U}_1^{\mathcal{H}} \times \mathcal{U}_2^{\mathcal{H}} \times \mathcal{U}_3^{\mathcal{H}}$, where

$$\begin{aligned} \mathcal{U}_3^{\mathcal{H}} = \mathcal{U}_{\mathcal{M}}^{\mathcal{H}} &:= \{w \in \mathcal{C}^0(\hat{\Omega}_{\mathcal{M}}^{\mathcal{H}}) : w|_K \in \mathcal{P}^1(K)\, \forall K \in \hat{\mathcal{T}}_{\mathcal{M}}^{\mathcal{H}}\} \\ \forall i \in \{1,2\}, \quad \hat{\mathcal{U}}_i^{\mathcal{H}} &:= \{w \in \mathcal{C}^0(\hat{\Omega}_i^{\mathcal{H}}) : w|_K \in \mathcal{P}^1(K)\, \forall K \in \hat{\mathcal{T}}_i^{\mathcal{H}}\} \end{aligned} \tag{5.49}$$

Notice that $u^{\mathcal{H}}$ is multi-valued in the elements that are cut by the two embedded interfaces. This feature allows us to represent discontinuities at the two interfaces.

The field of internal variables ξ_i^n, for any $n \in [\![0\, N]\!]$ and for any $i \in [\![1\, 3]\!]$, will be defined over the corresponding approximated domain $\Omega_i^{\mathcal{H}}$. These fields do not need to be extended to the fictitious domain.

5.2.5.4 Additional sets

We now define some additional sets, which is required to introduce the stabilisation strategy for our implicit boundary multiresolution formulation.

For stabilisation purpose, let us denote all elements which are intersected by $\Gamma_{12}^{\mathcal{H}}$ by

$$\hat{\mathcal{G}}_{12}^{\mathcal{H}} := \{K \in \mathcal{T}^{\mathcal{H}} \,|\, K \cap \Gamma_{12}^{\mathcal{H}} \neq \emptyset\} \tag{5.50}$$

The domain corresponding to this set is denoted by $\hat{\Gamma}_{12}^{\mathcal{H}} := \bigcup_{K \in \hat{\mathcal{G}}_{12}^{\mathcal{H}}} K$. Similarly for the fine domains, for $i \in \{1,2\}$,

$$\hat{\mathcal{G}}_i^{\mathcal{H}} := \{K \in \mathcal{T}^{\mathcal{H}} \,|\, K \cap \Gamma_i^{\mathcal{H}} \neq \emptyset\} \tag{5.51}$$

and the corresponding domains will be denoted by $\hat{\Gamma}_i^{\mathcal{H}} := \bigcup_{K \in \hat{\mathcal{G}}_i^{\mathcal{H}}} K$. We now define the set of Ghost-Penalty element edges for fictitious domain $\hat{\Omega}_1^{\mathcal{H}}$

$$\hat{\mathcal{F}}_1^G := \{F = K \cap K' : K \in \hat{\mathcal{T}}_1^{\mathcal{H}} \text{ and } K' \in \hat{\mathcal{T}}_1^{\mathcal{H}},\, F \cap \hat{\Gamma}_1^{\mathcal{H}} \neq \emptyset\} \tag{5.52}$$

and for fictitious domain $\hat{\Omega}_i^{\mathcal{H}}$, $i \in \{2,3\}$ as

$$\hat{\mathcal{F}}_i^G := \{F = K \cap K' : K \in \hat{\mathcal{T}}_i^{\mathcal{H}} \text{ and } K' \in \hat{\mathcal{T}}_i^{\mathcal{H}},\, F \cap \hat{\Gamma}_i^{\mathcal{H}} \neq \emptyset\} \tag{5.53}$$

5.2.6 Implicit boundary finite element formulation

The finite element multiresolution formulation is as follows: for any $v^{\mathcal{H}} \in \mathcal{U}^{\mathcal{H}}$ satisfying the homogeneous Dirichlet boundary conditions,

$$a^{\mathcal{H}}(u^{\mathcal{H}}, v^{\mathcal{H}}) + a_\sharp^{\mathcal{H}}(u^{\mathcal{H}}, v^{\mathcal{H}}) + a_\heartsuit^{\mathcal{H}}(u^{\mathcal{H}}, v^{\mathcal{H}}) = l^{\mathcal{H}}(v^{\mathcal{H}})\,. \tag{5.54}$$

In the previous formulation, the bilinear form $a^{\mathcal{H}}$ is defined by

$$a^{\mathcal{H}}(u^{\mathcal{H}}, v^{\mathcal{H}}) = \sum_{i=1}^{3} \int_{\Omega_i^{\mathcal{H}}} \sigma_i(\nabla_s u_i^{\mathcal{H}}) : \nabla_s v_i^{\mathcal{H}}\, dx\,. \tag{5.55}$$

and the linear form $l^{\mathcal{H}}$ is as follows:

$$l^{\mathcal{H}}(v^{\mathcal{H}}) = \sum_{i=1}^{3} \int_{\Omega_i^{\mathcal{H}}} f_b \cdot v_i^{\mathcal{H}}\, dx + \sum_{i=1}^{3} \int_{\partial\Omega_{t,i}^{\mathcal{H}}} \tau \cdot v_i^{\mathcal{H}}\, dx\,, \tag{5.56}$$

Term $a_\sharp^{\mathcal{H}}$ is composed of terms that allows gluing the three domains together, using Nitsche's method. It is further expanded as

$$a_\sharp^{\mathcal{H}}(u^{\mathcal{H}}, v^{\mathcal{H}}) = a_{1,\sharp}^{\mathcal{H}}(u^{\mathcal{H}}, v^{\mathcal{H}}) + a_{2,\sharp}^{\mathcal{H}}(u^{\mathcal{H}}, v^{\mathcal{H}}) + a_{3,\sharp}^{\mathcal{H}}(u^{\mathcal{H}}, v^{\mathcal{H}})\,, \tag{5.57}$$

where the first term is for the interface between matrix and inclusion, while the second and third terms are for the interfaces between the coarse and fine (i.e. matrix

and inclusion, respectively) subdomains. We have that

$$\begin{aligned} a^{\mathcal{H}}_{i,\sharp}(u^{\mathcal{H}}, v^{\mathcal{H}}) &= \gamma_i \hat{w}_i \int_{\Gamma_i^{\mathcal{H}}} [\![u^{\mathcal{H}}]\!]_i \cdot [\![v^{\mathcal{H}}]\!]_i \, dx \\ &- \int_{\Gamma_i^{\mathcal{H}}} \{t\}_i (u^{\mathcal{H}}) \cdot [\![v^{\mathcal{H}}]\!]_i \, dx \\ &- \int_{\Gamma_i^{\mathcal{H}}} \{t\}_i (v^{\mathcal{H}}) \cdot [\![u^{\mathcal{H}}]\!]_i \, dx \, . \end{aligned} \tag{5.58}$$

where

$$\begin{aligned} [\![u^{\mathcal{H}}]\!]_1 &= u_1^{\mathcal{H}} - u_2^{\mathcal{H}} \, , \\ [\![u^{\mathcal{H}}]\!]_2 &= u_1^{\mathcal{H}} - u_3^{\mathcal{H}} \, , \\ [\![u^{\mathcal{H}}]\!]_3 &= u_2^{\mathcal{H}} - u_3^{\mathcal{H}} \, , \end{aligned} \tag{5.59}$$

denotes the jumps in the displacements across $\Gamma_1^{\mathcal{H}}, \Gamma_2^{\mathcal{H}}$ and $\Gamma_3^{\mathcal{H}}$ respectively; and $\{t\}_i$ denotes the following weighted averages

$$\begin{aligned} \{t\}_1 &= w_1^1 \sigma_1(\nabla_s u_1^{\mathcal{H}}) \cdot n_1 + w_1^2 \sigma_2(\nabla_s u_2^{\mathcal{H}}) \cdot n_1 \, , \\ \{t\}_2 &= w_2^1 \sigma_1(\nabla_s u_1^{\mathcal{H}}) \cdot n_2 + w_2^2 \sigma_3(\nabla_s u_3^{\mathcal{H}}) \cdot n_2 \, , \\ \{t\}_3 &= w_3^1 \sigma_2(\nabla_s u_2^{\mathcal{H}}) \cdot n_2 + w_3^2 \sigma_3(\nabla_s u_3^{\mathcal{H}}) \cdot n_2 \, , \end{aligned} \tag{5.60}$$

where $n_1 = -\frac{\nabla \phi_1}{|\nabla \phi_1|}$, $n_2 = -\frac{\nabla \phi_2}{|\nabla \phi_2|}$.

$$\begin{aligned} w_1^1 &= \frac{E_2}{E_1 + E_2}, \quad & w_1^2 &= \frac{E_1}{E_1 + E_2} \\ w_2^1 &= \frac{\frac{E_3}{H}}{\frac{E_1}{h} + \frac{E_3}{H}}, \quad & w_2^2 &= \frac{\frac{E_1}{h}}{\frac{E_1}{h} + \frac{E_3}{H}} \\ w_3^1 &= \frac{\frac{E_3}{H}}{\frac{E_2}{h} + \frac{E_3}{H}}, \quad & w_3^2 &= \frac{\frac{E_2}{h}}{\frac{E_2}{h} + \frac{E_3}{H}} \, . \end{aligned} \tag{5.61}$$

$$\begin{aligned}\hat{w}_1 &= \frac{E_1 E_2}{h(E_1+E_2)},\\ \hat{w}_2 &= \frac{\frac{E_1}{H}\frac{E_3}{h}}{\frac{E_1}{h}+\frac{E_3}{H}},\\ \hat{w}_3 &= \frac{\frac{E_2}{H}\frac{E_3}{h}}{\frac{E_2}{h}+\frac{E_3}{H}}.\end{aligned} \tag{5.62}$$

Finally, $a_{\heartsuit}^{\mathcal{H}}$ is an interior penalty regularisation term that reads as, for $i \in \{1,2,3\}$,

$$a_{\heartsuit}^{\mathcal{H}}(u^{\mathcal{H}}, \delta u^{\mathcal{H}}) = \sum_{F\in\hat{\mathcal{F}}_i^G}\left(\int_F \beta_i \mathcal{H}_i [\![\nabla_s u^{\mathcal{H}}]\!][\![\nabla_s(v^{\mathcal{H}})]\!]\, dx\right). \tag{5.63}$$

where $\beta_i > 0$ is the ghost penalty parameter, and $[\![x]\!]$ is the normal jump of quantity x over the F. As explained in [7, 5], the ghost penalty term extends the coercivity from the physical domain into the discretised domain.

5.3 Numerical Results

This section first verifies the proposed multiscale framework for a simplified multiscale elasticity problem. Then, we adopt von Mises material for the multiscale model and assess it for two types of hard and void micro inclusions. Eventually, we assess the performance of the framework for the zooms that are time-dependent and relocate during the simulation.

5.3.1 Verification test for an elasticity problem in a quasi-uniform porous structure

In this section, the proposed multiresolution framework is assessed for a heterogeneous structure with micropores and then compared with a full microscale FEM model and a smoothed concurrent multiscale method proposed in [189]. We consider the same quasi-uniform porous medium given in [189] which includes circular pores

distributed all over the domain (as depicted in Figure 5.2). The material behaviour is assumed as elastic and isotropic. According to [189], the material properties for matrix are given as $E_1 = 1$ and $\nu_1 = 0.3$, and for the homogenised model are derived by MMTT [192, 191] as following: $E_3 = 0.78$ and $\nu_3 = 0.3$.

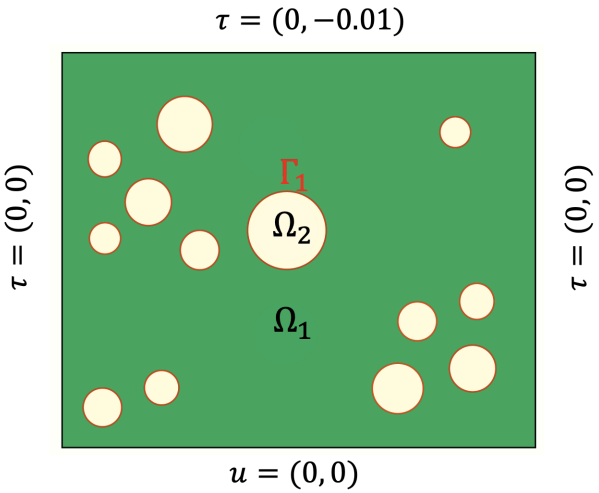

Figure 5.2: Boundary conditions and geometry of a heterogeneous structure with compression test

The computational meshes for the FEM and multiresolution models are shown in Figure 5.3a,b, which contain linear Lagrangian elements with the smallest element size of $h = 0.054$. The element size inside the zoom area is the same as in reference models for verification purposes, while in the coarse region it is set to $H = 0.11$. As shown for the discretised domain in Figure 5.4, the three types interfaces, $\Gamma_1^{(H,h)}$, $\Gamma_2^{(H,h)}$ and $\Gamma_3^{(H,h)}$ intersect the background mesh in an arbitrary fashion. The ghost penalty parameters for the intersected elements are specified as $\beta_1 = \beta_2 = \beta_3 = 0.005$. Additionally, the Nitsche's penalty parameters used to couple the micro and macroscale models are $\gamma_2 = \gamma_3 = 10$.

A compression test is conducted for the heterogeneous structure where the displacements are fixed along the x and y directions on the lower end, and traction $\tau = (0, -0.01)$ is prescribed along the top edge. The FEM displacement component u_y contour is obtained and used as a reference solution, see Figure 5.5a. The same test is carried out for the multiscale model. The corresponding displacement field

(a) (b)

Figure 5.3: Discretised domains; a) FE conforming mesh and b) CutFEM non-conforming mesh.

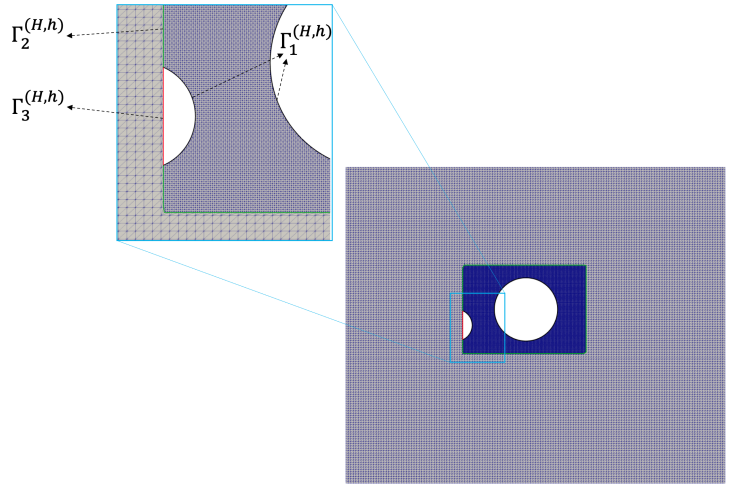

Figure 5.4: Discretised domain for the multiscale CutFEM including $\Gamma_1^{(H,h)}$, $\Gamma_2^{(H,h)}$ and $\Gamma_3^{(H,h)}$. The coarse elements cut with $\Gamma_2^{(H,h)}$ and $\Gamma_3^{(H,h)}$ and the fine elements cut with $\Gamma_1^{(H,h)}$ are shown with their sub-triangules that are used for the integration purpose.

component is shown in Figure 5.5b. When our multiscale model is compared with the FEM and smoothed concurrent multiscale models, a close similarity of u_y is observed inside the zooming region. Outside of the zoom, again, a satisfactory agreement is achieved.

We compute the stress field component σ_{yy} in Figure 5.6. Here again, a good agreement is achieved between the multiscale and reference models. The homogeneous model adopted in the coarse domain of the multiscale model smooth out the

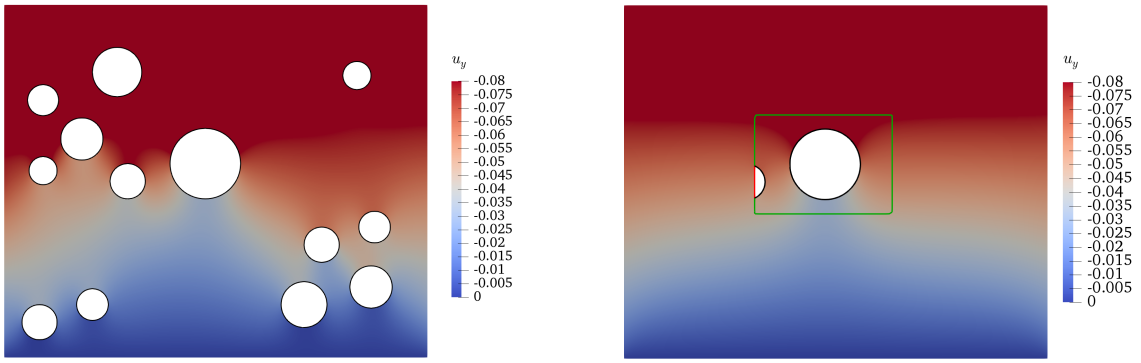

(a) (b)

Figure 5.5: Displacement field component u_y; a) FEM and b) Multiscale CutFEM.

fluctuations produced by the coarse pores, and the overall trend in this domain is captured very well.

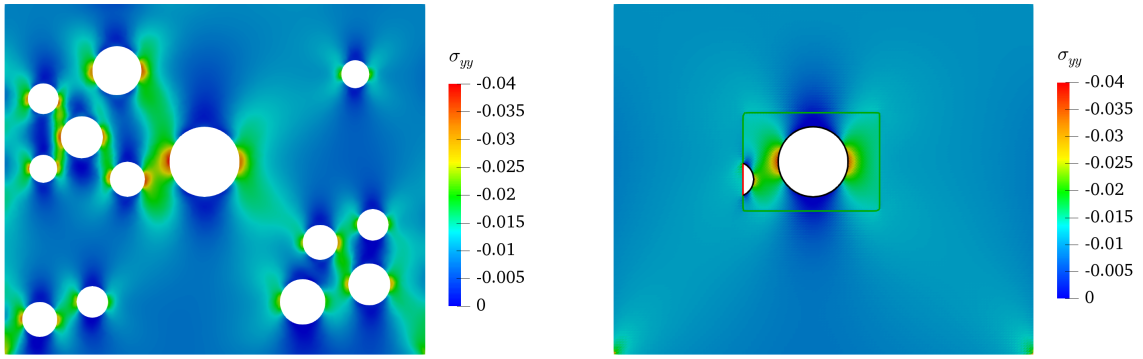

(a) (b)

Figure 5.6: Stress field component σ_{yy}; a) FEM and b) Multiscale CutFEM.

For further investigations, we study the effects of mesh coarsening in the coarse region of the multiresolution framework on the energy norm of the error field. The corresponding mesh layouts for the fine and coarse multiresolution models are depicted in Figures 5.3b and 5.7b, respectively. While the mesh outside the zoom is different for two multiresolution models, the mesh inside is considered the same size. Moreover, as shown in Figure 5.7a, a full fine resolution mesh is used for computation of the error field. We compute the energy norm of the error field with respect to the reference FE model according to the following formulation.

$$\|e\| = \sqrt{\int_{\Omega} \nabla_s e : \nabla_s e \, dx} \,. \tag{5.64}$$

where $e = u_{\text{ref}} - u$. u_{ref} and u denote the displacement for FE and multiresolution models, respectively.

The energy norm of the error fields for the two multiresolution models is computed as shown in Figure 5.8, where $H = 0.11$ for the first multiresolution model and $H = 0.22$ for the second one. The results indicate that the error norm within the zoomed region remains minimal for both models, irrespective of the coarsening of the mesh outside the zoomed area. Furthermore, the analysis suggests that the primary source of error outside the zoomed region can be attributed to the homogenisation approximation rather than the mesh size. This assertion is supported by the observation that the $\|e\|$ remains unaltered in the coarse region despite the mesh coarsening process.

To facilitate a quantitative assessment, a comparative analysis of the computed σ_{yy} values is conducted between the full FEM and the multiscale CutFEM at four distinct locations situated within the zoom region, as depicted in Figure 5.7b. These locations are designated as A(5.7,6.7), B(3.9,5.7), C(4.36,5.15), and D(7.1,5.5), each carrying their unique significance. The corresponding relative absolute errors at these designated points are computed and reported in table 5.1, ranging between 5.5% and 13.4%. Importantly, the observed errors within the zoom region fall well within an acceptable range, with point C displaying the highest deviation and point D demonstrating the lowest deviation. The slight increase in error on the left side of

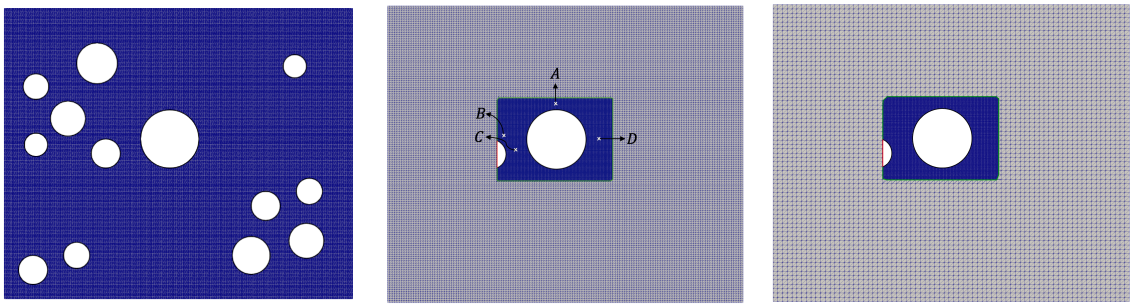

(a) (b) (c)

Figure 5.7: Computational meshes for; a) computing the error field ($h_{min} = 0.054$), b) multiresolution CutFEM with a mesh size $H = 0.11$ in the macroscale region and c) multiresolution CutFEM with a mesh size $H = 0.22$ in the macroscale region. For both multiresolution CutFEM models we have $h = 0.054$. All the cut elements in the multiresolution CutFEM are shown with their integration subtriangles.

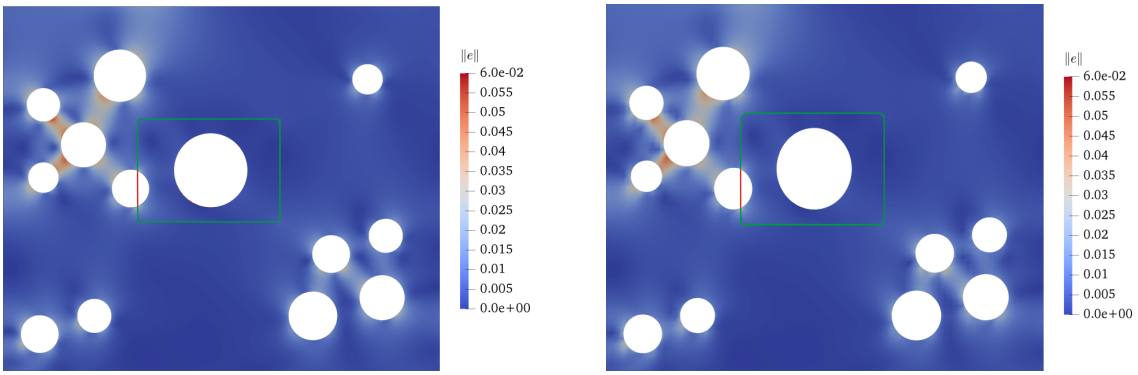

(a) (b)

Figure 5.8: Energy norm of error field $\|e\|$ for multiscale CutFEM with different mesh resolutions in the macroscale region; a) $H = 0.11$ and b) $H = 0.22$. A uniform mesh size of $h = 0.054$ is used for plotting the $\|e\|$.

the zoom can be attributed to the proximity of adjacent pores located just outside the zoom, which introduce certain perturbations within the homogenised model, thereby influencing the solution within the zoom in the heterogeneous models.

σ_{yy}	Point A	Point B	Point C	Point D
Full FEM	0.000170	-0.0125	-0.0252	-0.0215
Multiscale CutFEM	0.000159	-0.0115	-0.0218	-0.0227
Absolute error (σ_{yy})	0.000011	0.001	0.0034	0.0008
Relative absolute error (%) (σ_{yy})	6.47	8	13.4	5.5

Table 5.1: Quantitative comparison of σ_{yy} between the full FEM and multiscale CutFEM at four different locations inside the zoom (A(5.7,6.7), B(3.9,5.7), C(4.36,5.15), and D(7.1,5.5)). The mesh sizes are $h = 0.054$ for both models, and $H = 0.11$ for the macroscale region of the multiscale CutFEM.

5.3.2 S shape heterogeneous structure with elastoplastic behaviour using fixed zooms

In this section, we assess the ability and efficiency of the multiresolution CutFEM in modelling heterogeneous structures with nonlinear material properties and different types of heterogeneities. We consider an S shape heterogeneous structure with a random distribution of heterogeneities. As shown in Figure 5.9, the heterogeneities can be either voids or hard inclusions. We assume von Mises elastoplastic material behaviour for these structures. The material properties heterogeneous structures are: $2E_1 = E_2 = 2$, $\nu_1 = \nu_2 = \nu_3 = 0.3$, $\sigma_1^c = \sigma_2^c = \sigma_3^c = 0.25$ and $\hat{H}_1^p = \hat{H}_2^p = \hat{H}_3^p = 10^{-2}$. The material properties for the macroscale homogenised model with voids and inclusions are calculated by using the MTT as follows, respectively: $E_3 = 0.5, 1.3$. To analyse the influence of different microstructural features on the accuracy of the proposed multiscale framework, we consider the geometry and distribution of the voids and hard inclusions to be similar in the two structures. We restrict the displacement along the x and y directions on the lower end and apply traction $\tau = (0, 0.18)$ incrementally (in 30 increments) on the top edge along the y direction.

We employ two circular zooms fixed over a background mesh (see Figure 5.10). We refine the mesh inside the zoom regions with a refinement scale defined as $s = \frac{1}{16}$ (means each coarse element is subdivided hierarchically into 16 fine elements), where the largest element size is $H = 0.06$. The discretised physical domain of multiresolution models in Figures 5.10b,c show that all the three interfaces intersect the coarse background mesh (see Figure 5.10a) for both models in a fully arbitrary

manner.

Next, we solve the nonlinear problem and assess the corresponding solution fields. The displacement field component u_y for two models in Figure 5.11 is smooth, especially in cut elements. Moreover, the stress field component σ_{yy} shown in Figure 5.12, is smooth for both structures. However, as expected, the structure with hard inclusion inherits more stiffness and absorbs more stresses inside and outside the zoom.

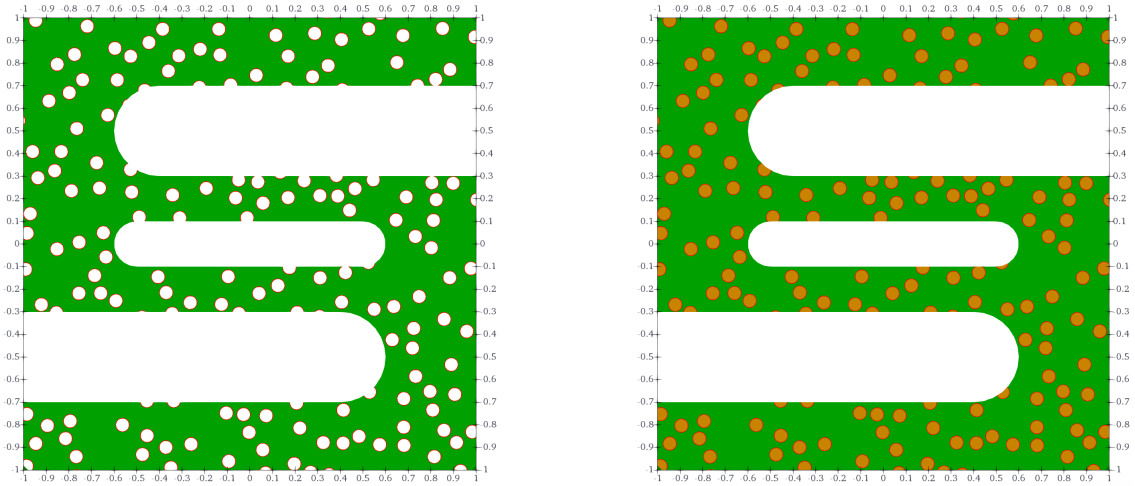

(a) (b)

Figure 5.9: Geometry of the heterogeneous structures; a) heterogeneities are voids, b) heterogeneities are hard inclusions

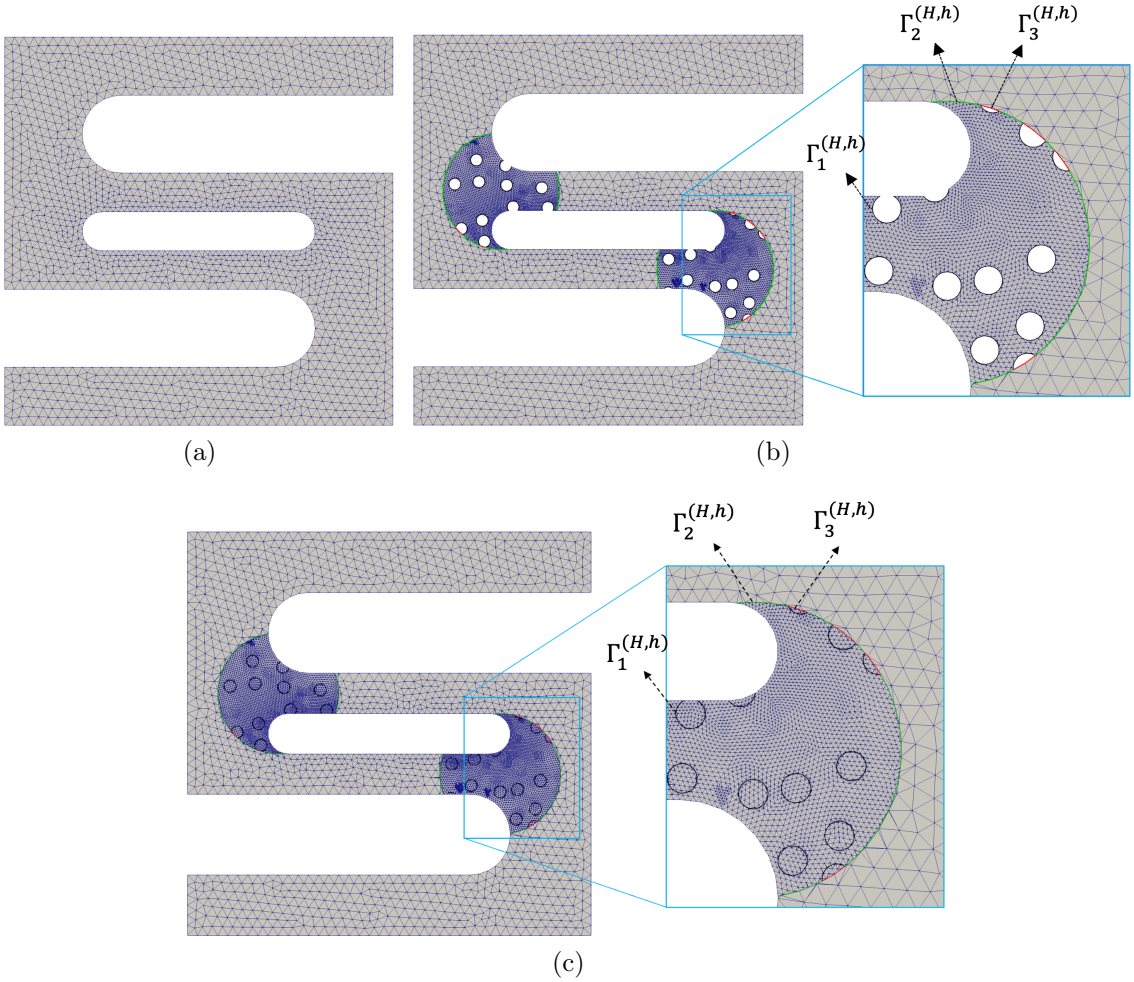

Figure 5.10: Computational meshes; a) coarse mesh, b) multiresolution mesh for the porous microstructure, c) multiresolution mesh for the microstructure with hard inclusions. The intersected elements are shown with their integration sub-triangles.

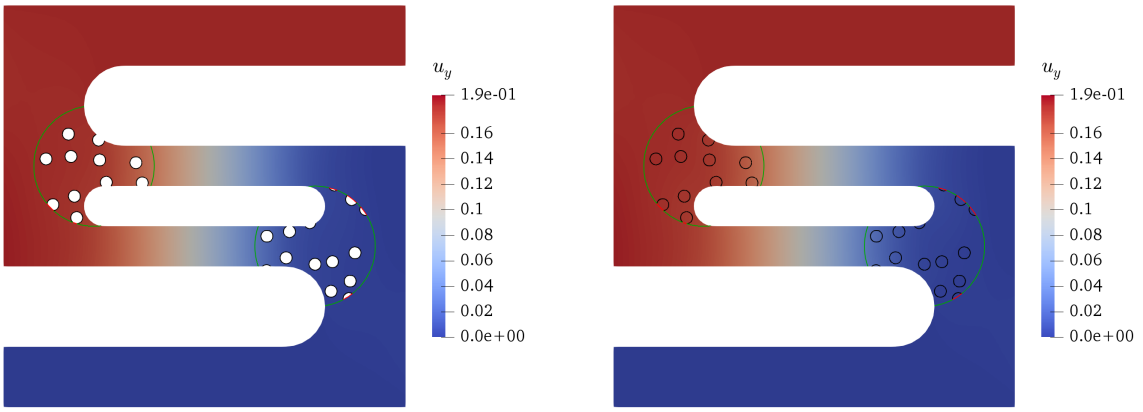

(a) (b)

Figure 5.11: Displacement field u_y for the heterogeneous structures in the last time step; a) heterogeneities are voids, b) heterogeneities are hard inclusions

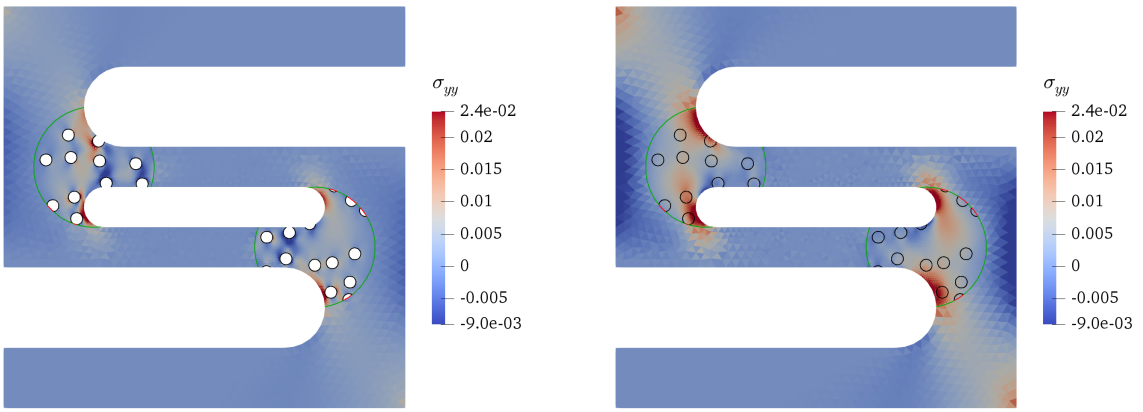

(a) (b)

Figure 5.12: Stress component σ_{yy} for the last time step; a) heterogeneities are voids, b) heterogeneities are hard inclusions

5.3.3 S shape porous structure with elastoplasic behaviour using moving zooms

This section is devoted to the numerical study of a moving zoom for the proposed multiresolution with a von Mises plasticity material behaviour. We here consider the S shape microporous structure analysed in section 5.3.2. However, contrary to the previous section, we will not fix the zooms over the background mesh but relocate them during the simulation. As shown in Figure 5.13, this relocation is carried out arbitrarily and independent of background mesh configuration. In this study, we change the location and size of zooming manually during the simulation to assess the numerical efficiency; however, using an adaptive approach would be more relevant from the physics point of view.

We show the displacement component u_y field for three different time in Figure 5.14. The results show that the multiscale solution with a nonlinear material stays convergent in each time step, even with the relocation of the zooming region. Furthermore, the global behaviour during simulation stays smooth and without oscillations.

Next, we show the results in the form of plastic strain growth during the simulation. We compute the effective plastic strain at three time steps and show the results in Figure 5.15. The changes in the zooms' location and size during the simulation are intended to capture the plastic strain growth.

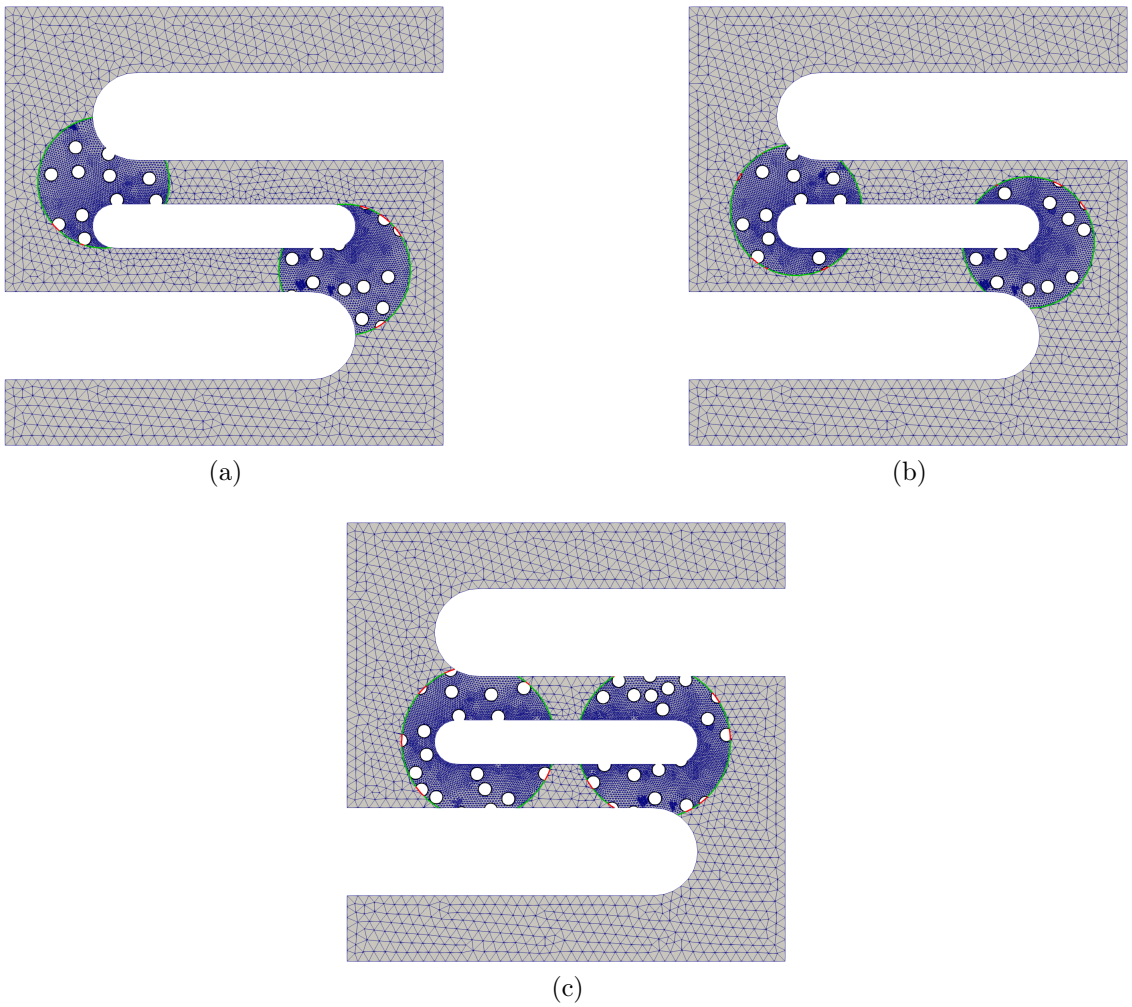

Figure 5.13: Computational meshes for the microporous heterogeneous structure with different set of zooms at various time steps, a) $\tau = (0, 0.05)$, b) $\tau = (0, 0.12)$ and c) $\tau = (0, 0.18)$. All the cut elements are depicted with their sub-triangles (used for their integration).

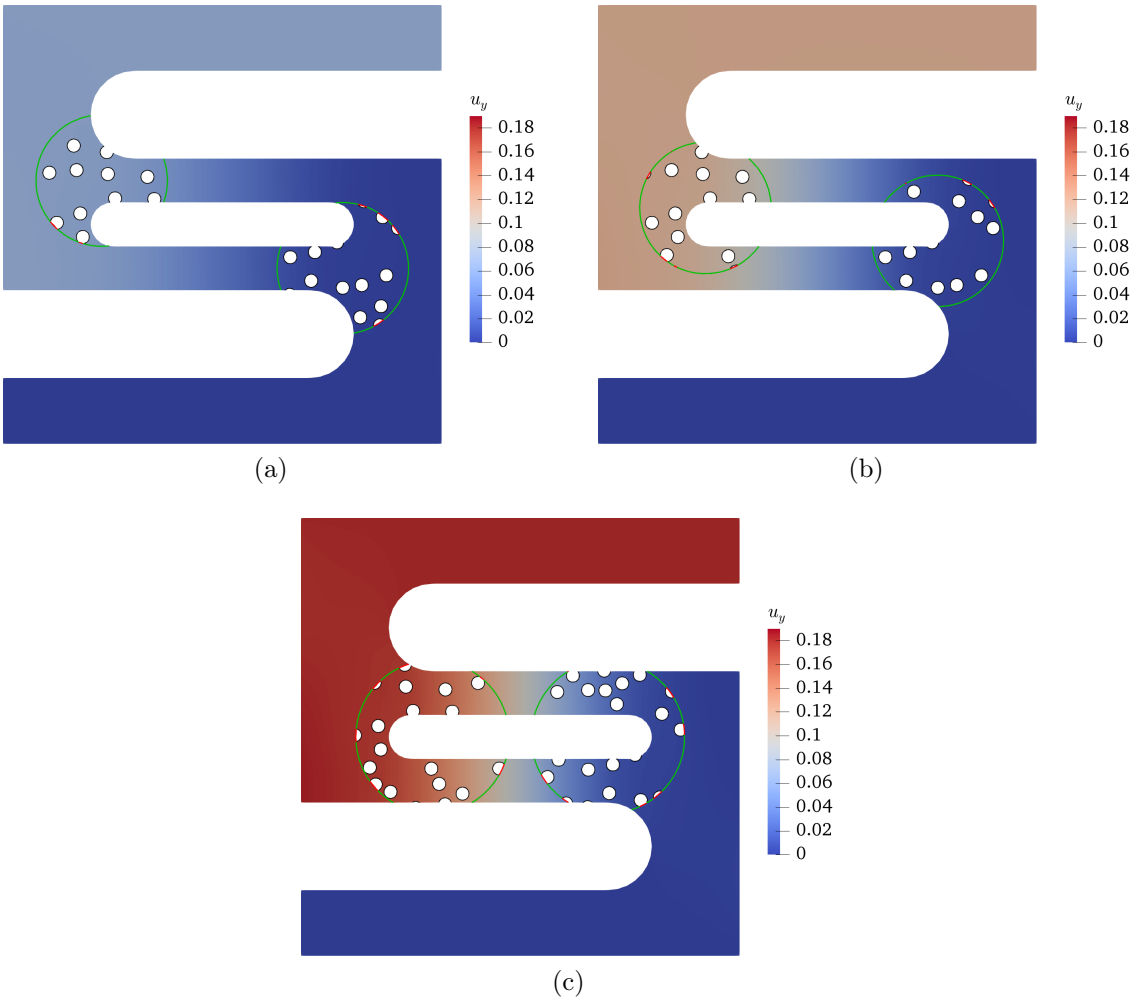

Figure 5.14: Displacement component u_y for the microporous heterogeneous structure with different set of zooms; a) $\tau = (0, 0.05)$, b) $\tau = (0, 0.12)$ and c) $\tau = (0, 0.18)$.

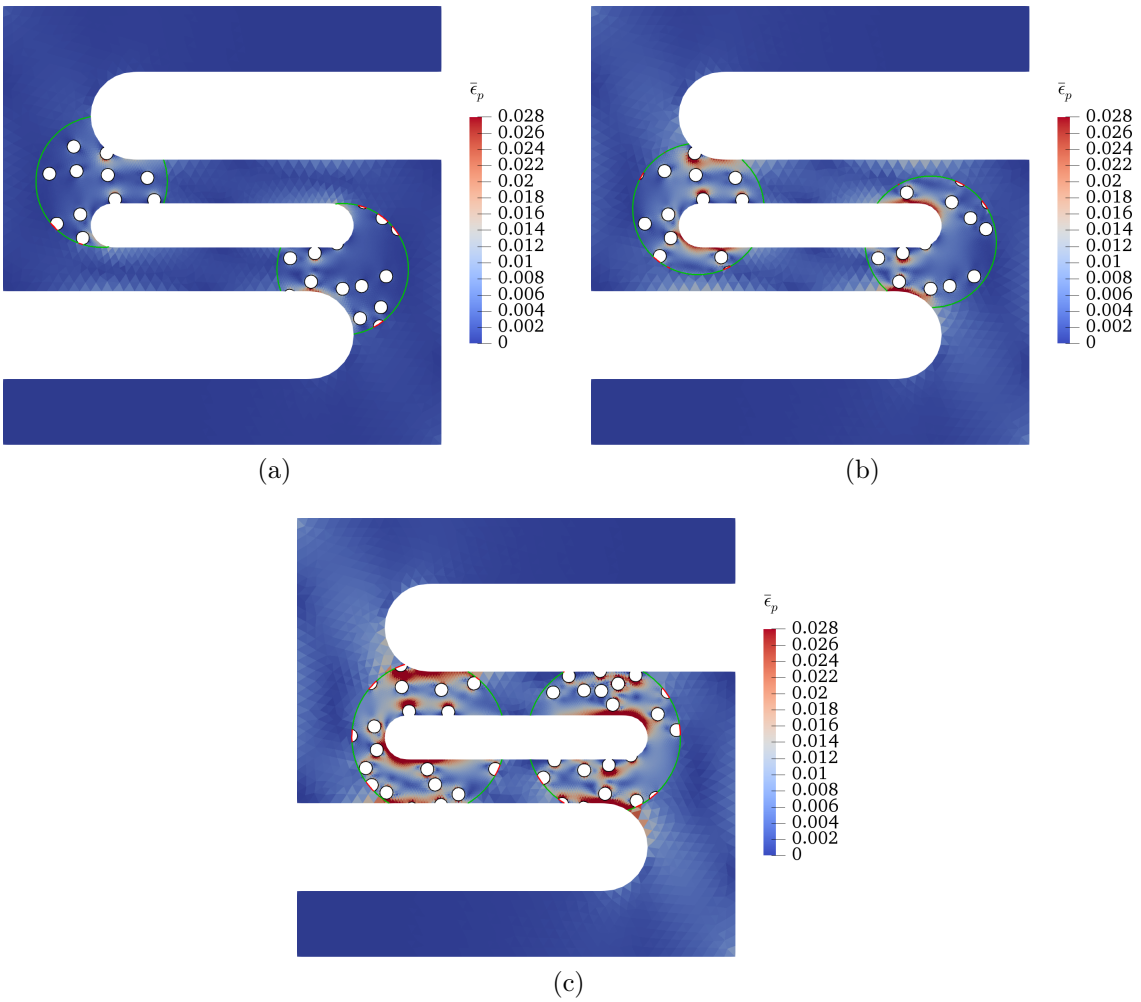

Figure 5.15: Effective plastic strain $\bar{\varepsilon}_p$ contours; a) $\tau = (0, 0.05)$, b) $\tau = (0, 0.12)$ and c) $\tau = (0, 0.18)$.

5.4 Conclusion

In this chapter, we developed another novel concurrent multiscale method based on CutFEM that couples micro and macroscale models through Nitsche's formulation over a sharp interface. We utilised three sets of interfaces to approximate the microstructure and zoom geometries over a multiresolution fixed background mesh. However, the arbitrary intersection of interfaces with the background mesh creates stability issues as follows:

- Stability of cut elements by only a single interface, including one of the following interfaces: $\Gamma_1^{(H,h)}$, $\Gamma_2^{(H,h)}$ and $\Gamma_3^{(H,h)}$.
- Stability of the cut elements intersected simultaneously by $\Gamma_1^{(H,h)}$, $\Gamma_2^{(H,h)}$ and $\Gamma_3^{(H,h)}$.

In our multiscale framework, we addressed the above-mentioned issues by applying the ghost penalty regularisation technique for the intersected elements. The regularisation includes displacement gradient jump term across the interface.

The framework was successfully applied for heterogeneous structures with linear elasticity and plasticity material properties. The numerical results showed that our concurrent multiscale technique is capable of modelling heterogeneous structures with complex microstructures with either micropores or micro inclusions in a mesh-independent way. The method was stable and accurate for different types of microstructures with pores or inclusions. Moreover, the relocation of the zoomed regions during the simulation was carried out seamlessly.

Chapter 6

Conclusion and Future Research

6.1 Conclusion

It has been widely recognised that several macroscopic phenomena, including fracture and failure, originate from the mechanics of the corresponding microstructure. The properties of microstructure constituents (e.g. the shape, size, volume fraction and material properties) all have a remarkable impact on the structure's response at the macroscale. Computational modelling of such heterogeneous materials is a challenging task for several reasons. Firstly, due to the multiscale nature of these materials, various essential length-scale properties need to be linked and reflected accurately in the computational model. Secondly, the computational resource is a limiting factor for a direct numerical simulation of large-scale structures. Concurrent multiscale modelling is capable of alleviating both challenges mentioned above. This framework is particularly appealing when modelling large structures, where complicated processes such as failure only occur in a small (local) portion of the structure, while the behaviour of the rest of the domain remains linear.

As discussed in chapters 1 and 2, there is an obvious need to use advanced discretisation methods for problems with complex microstructures and/or time-dependent geometries to improve the robustness and efficiency of computational analysis. The advanced discretisation methods, such as the CutFEM technique, approximate the

solution of boundary value problems with unfitted meshes, alleviating mesh-related obstacles. This is also crucial when dealing with progressive phenomena in the context of concurrent multiscale modelling, where the corresponding zooming interface moves or changes during the simulation.

This thesis focused on the application of the CutFEM technique for concurrent multiscale analysis. The use of CutFEM allowed us to represent the geometries of microstructure geometry and micro-macro interface mesh independently. Two novel coupling frameworks were developed for linking the macroscale and microscale models owning complex microstructures.

In the first concurrent multiscale framework, we presented a mixing technique to couple the micro and macro scale models over a single computational mesh. We used a homogenised FEM model in the macro subdomain and the CutFEM model representing the microstructure in the microscale domain (or zooming region). We showed that using the homogenised FEM model in the macroscale model alleviates the geometrical artefacts perceived in the counterpart adaptive CutFEM simulations, which is mainly because of coarse level set functions. Moreover, utilising the mixing strategy within a smoothed micro/macro coupling interface ensured the well conditioning of the system matrix, particularly when the micropores were cut by the zooming interface. We tested the framework for 2D and 3D linear elasticity problems with complex microstructures. The corresponding results were promising in terms of accuracy and efficiency.

In the second concurrent multiscale method, unlike the first one, we proposed a sharp interface between micro and macro scale models for coupling purposes. The coupling is based on Nitsche's method. Then, we refine the mesh in the microscale region hierarchically. Moreover, like the first framework, we employ ghost penalty regularisation to stabilise intersected elements by two types of interfaces representing (1) the zooming region and (2) the microstructure. We showed that our results are stable even when the elements are intersected simultaneously by the two interfaces. The methodology was applied successfully for linear elasticity and plasticity problems with stationary and moving zooming interfaces.

In the third contribution that is presented in chapter 4, we applied the smoothed

concurrent multiscale method for phase field fracture problems. The micro and macro scale phase fields were computed over a single computational mesh and were mixed through a smooth function in their transition region. The corresponding numerical results demonstrated that the mixing technique is reliable for phase field problems that are intrinsically nonlinear. Moreover, the results provided compelling evidence of the advantages of the concurrent multiscale modelling over employing the full microscale CutFEM in terms of computational costs.

In this thesis, we developed our computational methodologies within a widely used open source finite element platform, called FEniCS [196]. The FEniCS is based on several components including the UFL [197] as is an interface for creating forms and the DOLFIN [198] as a finite element library. Our CutFEM-based frameworks were extended in the CutFEM library [5] that has been developed on the FEniCS platform.

6.2 Future research

This last section discusses the possible extensions of the present work in following aspects:

- An extension of two proposed concurrent multiscale methods for the problems that their zooming regions are not known beforehand. This aim requires to develop an efficient adaptive scheme that dynamically locates the appropriate zooming regions based on criteria such as error estimators or machine learning algorithms, reducing computational costs and enhancing accuracy.

- Extension of the CutFEM and concurrent multiscale methods for discrete crack problems. In such problems, further treatments will be required for the elements intersected simultaneously by the interfaces related to the crack, microstructure and zooming regions.

- Large deformation problems. Current multiscale methodologies are limited to a small deformation regime, which can be extended to materials with large

deformation behaviours, such as soft tissues.

- Investigating the performance of proposed coupling techniques for multiscale problems with different constitutive models in the fine and coarse regions, for instance, continuum-atomistic or continuum-molecular.

- Employing high order interfaces within our concurrent multiscale frameworks, which will improve the accuracy of complex geometries representations with coarse elements.

- In multiphysics problems, particularly when local progressive phenomena occur, such as hydraulic fractures. In this regard, a further application of the phase field fracture model within our concurrent multiscale frameworks can be investigated.

Bibliography

[1] J. Oliver, A. E. Huespe, P. J. Sánchez, A comparative study on finite elements for capturing strong discontinuities: E-fem vs x-fem, Computer methods in applied mechanics and engineering 195 (37-40) (2006) 4732–4752. doi:https://doi.org/10.1016/j.cma.2005.09.020.

[2] T. Zohdi, P. Wriggers, A domain decomposition method for bodies with heterogeneous microstructure basedon material regularization, International Journal of Solids and Structures 36 (17) (1999) 2507–2525. doi:https://doi.org/10.1016/S0020-7683(98)00124-3.

[3] T. I. Zohdi, J. T. Oden, G. J. Rodin, Hierarchical modeling of heterogeneous bodies, Computer methods in applied mechanics and engineering 138 (1-4) (1996) 273–298. doi:https://doi.org/10.1016/S0045-7825(96)01106-1.

[4] P. Raghavan, S. Ghosh, Concurrent multi-scale analysis of elastic composites by a multi-level computational model, Computer Methods in Applied Mechanics and Engineering 193 (6) (2004) 497–538. doi:https://doi.org/10.1016/j.cma.2003.10.007.

[5] E. Burman, S. Claus, P. Hansbo, M. Larson, A. Massing, Cutfem: discretizing geometry and partial differential equations, International Journal for Numerical Methods in Engineering 104 (2015) 472–501. doi:https://doi.org/10.1002/nme.4823.

[6] E. Burman, P. Hansbo, Fictitious domain finite element methods using cut elements: I. a stabilized lagrange multiplier method, Computer Methods in Applied Mechanics and Engineering 199 (41) (2010) 2680 – 2686. doi:https://doi.org/10.1016/j.cma.2010.05.011.

[7] E. Burman, P. Hansbo, Fictitious domain finite element methods using cut elements: Ii. a stabilized nitsche method, Applied Numerical Mathematics 62 (4) (2012) 328 – 341. doi:https://doi.org/10.1016/j.apnum.2011.01.008.

[8] A. Massing, B. Schott, W. A. Wall, A stabilized nitsche cut finite element method for the oseen problem, Computer Methods in Applied Mechanics and Engineering 328 (2018) 262 – 300. doi:https://doi.org/10.1016/j.cma.2017.09.003.

[9] J. Fish, The s-version of the finite element method, Computers & Structures 43 (3) (1992) 539 – 547. doi:https://doi.org/10.1016/0045-7949(92)90287-A.

[10] B. Lamichhane, B. Wohlmuth, Mortar finite element for interface problems, Computing 72 (2004) 333–348. doi:https://doi.org/10.1007/s00607-003-0062-y.

[11] E. B. Tadmor, M. Ortiz, R. Phillips, Quasicontinuum analysis of defects in solids, Philosophical Magazine A 73 (6) (1996) 1529–1563. doi:https://doi.org/10.1080/01418619608243000.

[12] G. J. Wagner, W. K. Liu, Coupling of atomistic and continuum simulations using a bridging scale decomposition, Journal of Computational Physics 190 (2003) 249–274. doi:https://doi.org/10.1016/S0021-9991(03)00273-0.

[13] L. A. Beex, P. Kerfriden, T. Rabczuk, S. Bordas, Quasicontinuum-based multiscale approaches for plate-like beam lattices experiencing in-plane and out-of-plane deformation, Computer Methods in Applied Mechanics and Engineering 279 (2014) 348–378. doi:https://doi.org/10.1016/j.cma.2014.06.018.

[14] S. Xiao, T. Belytschko, A bridging domain method for coupling continua with molecular dynamics, Computer Methods in Applied Mechanics and Engineering 193 (2004) 1645–1669. doi:https://doi.org/10.1016/j.cma.2003.12.053.

[15] T. Belytschko, S. Xiao, Coupling methods for continuum model with molecular model, International Journal for Multiscale Computational Engineering 1 (2003) 115–126. doi:10.1615/IntJMultCompEng.v1.i1.100.

[16] H. B. Dhia, Further insights by theoretical investigations of the multiscale arlequin method, International Journal for Multiscale Computational Engineering 6 (2008) 215–232. doi:10.1615/IntJMultCompEng.v6.i3.30.

[17] H. B. Dhia, Multiscale mechanical problems: the arlequin method, Comptes Rendus de l'Academie des Sciences Series IIB Mechanics Physics Astronomy 326 (1998) 899–904.

[18] H. Dhia, G. Rateau, The arlequin method as a flexible engineering design tool, International Journal for Numerical Methods in Engineering 62 (2005) 1442–1462. doi:https://doi.org/10.1002/nme.1229.

[19] P.-A. Guidault, T. Belytschko, On the l^2 and the h^1 couplings for an overlapping domain decomposition method using lagrange multipliers, International Journal for Numerical Methods in Engineering 70 (2007) 322–350. doi:https://doi.org/10.1002/nme.1882.

[20] R. Gracie, T. Belytschko, Concurrently coupled atomistic and xfem models for dislocations and cracks, International Journal for Numerical Methods in Engineering 78 (2009) 354–378. doi:10.1002/nme.2488.

[21] J. Fish, M. A. Nuggehally, M. S. Shepard, C. R. Picu, S. Badia, M. L. Parks, H. B. Dhia, Concurrent atc coupling based on a blend of the continuum stress and the atomistic force, Computer Methods in Applied Mechanics and Engineering 196 (2007) 4548–4560. doi:https://doi.org/10.1016/j.cma.2007.05.020.

[22] P. T. Bauman, H. B. Dhia, N. Elkhodja, T. Oden, S. Prudhomme, On the application of the arlequin method to the coupling of particle and continuum models, Computational Mechanics 42 (2008) 511–530. doi:https://doi.org/10.1007/s00466-008-0291-1.

[23] A. Massing, M. G. Larson, A. Logg, Efficient implementation of finite element methods on nonmatching and overlapping meshes in three dimensions, SIAM Journal on Scientific Computing 35 (1) (2013) C23–C47. doi:https://doi.org/10.1137/11085949X.

[24] N. Moës, J. Dolbow, T. Belytschko, A finite element method for crack growth without remeshing, International Journal for Numerical Methods in Engineering 46 (1) (1999) 131–150. doi:https://doi.org/10.1002/(SICI)1097-0207(19990910)46:1<131::AID-NME726>3.0.CO;2-J.

[25] J.-C. Passieux, J. Réthoré, A. Gravouil, M.-C. Baietto, Local/global non-intrusive crack propagation simulation using a multigrid x-fem solver, Computational Mechanics 52 (6) (2013) 1381–1393. doi:https://doi.org/10.1007/s00466-013-0882-3.

[26] E. Burman, Ghost penalty, Comptes Rendus Mathematique 348 (2010) 1217–1220. doi:https://doi.org/10.1016/j.crma.2010.10.006.

[27] A. Hansbo, P. Hansbo, A finite element method for the simulation of strong and weak discontinuities in solid mechanics, Computer methods in applied mechanics and engineering 193 (33-35) (2004) 3523–3540. doi:https://doi.org/10.1016/j.cma.2003.12.041.

[28] A. Johansson, M. G. Larson, A. Logg, Multimesh finite elements with flexible mesh sizes, Computer Methods in Applied Mechanics and Engineering 372 (2020) 113420. doi:https://doi.org/10.1016/j.cma.2020.113420.

[29] R. Guldberg, S. Hollister, G. Charras, The accuracy of digital image-based finite element models, Journal of Biomechanical Engineering (1998). doi:https://doi.org/10.1115/1.2798314.

[30] P. Bhattacharya, D. Betts, G. H. van Lenthe, A novel contact interaction formulation for voxel-based micro-finite-element models of bone, International Journal for Numerical Methods in Engineering 115 (2018) 411–426. doi:https://doi.org/10.1002/nme.5810.

[31] E. Lopez, E. Abisset-Chavanne, F. Lebel, R. Upadhyay, S. Comas, C. Binetruy, F. Chinesta, Advanced thermal simulation of processes involving materials exhibiting fine-scale microstructures, International Journal of Material Forming 9 (2016) 179–202. doi:https://doi.org/10.1007/s12289-015-1222-2.

[32] T. Pan, C. Chen, Q. Yu, Three-dimensional micromechanical modeling of concrete degradation under multiphysics fields, Composite Structures 175 (2017) 7–18. doi:https://doi.org/10.1016/j.compstruct.2017.05.008.

[33] J. Homminga, R. Huiskes, B. Van Rietbergen, P. Rüegsegger, H. Weinans, Introduction and evaluation of a gray-value voxel conversion technique, Journal of Biomechanics 34 (4) (2001) 513–517. doi:10.1016/s0021-9290(00)00227-x.

[34] A. Rouwane, R. Bouclier, J.-C. Passieux, J.-N. Périé, Adjusting fictitious domain parameters for fairly priced image-based modeling: Application to the regularization of digital image correlation, Computer Methods in Applied Mechanics and Engineering 373 (2021) 113507. doi:https://doi.org/10.1016/j.cma.2020.113507.

[35] J. Parvizian, A. Düster, E. Rank, Finite cell method, Computational Mechanics 41 (2007) 121–133. doi:https://doi.org/10.1007/s00466-007-0173-y.

[36] E. Nadal, J. Ródenas, J. Albelda, M. Tur, J. Tarancón, F. Fuenmayor, Efficient finite element methodology based on cartesian grids: application to structural shape optimization, in: Abstract and applied analysis, Vol. 2013, Hindawi, 2013, pp. 1–19. doi:https://doi.org/10.1155/2013/953786.

[37] J. C. Simo, J. Oliver, F. Armero, An analysis of strong discontinuities induced by strain-softening in rate-independent inelastic solids, Computational mechanics 12 (5) (1993) 277–296. doi:https://doi.org/10.1007/BF00372173.

[38] R. I. Borja, A finite element model for strain localization analysis of strongly discontinuous fields based on standard galerkin approximation, Computer Methods in Applied Mechanics and Engineering 190 (11) (2000) 1529–1549. doi:https://doi.org/10.1016/S0045-7825(00)00176-6.

[39] C. Miehe, F. Welschinger, M. Hofacker, Thermodynamically consistent phase-field models of fracture: Variational principles and multi-field fe implementations, International Journal for Numerical Methods in Engineering 83 (10) (2010) 1273–1311. doi:https://doi.org/10.1002/nme.2861.

[40] C. Miehe, M. Hofacker, F. Welschinger, A phase field model for rate-independent crack propagation: Robust algorithmic implementation based on operator splits, Computer Methods in Applied Mechanics and Engineering 199 (45) (2010) 2765–2778. doi:https://doi.org/10.1016/j.cma.2010.04.011.

[41] A. Hansbo, P. Hansbo, An unfitted finite element method, based on nitsche's method, for elliptic interface problems, Computer Methods in Applied Mechanics and Engineering 191 (2002) 5537–5552. doi:https://doi.org/10.1016/S0045-7825(02)00524-8.

[42] E. Burman, S. Claus, A. Massing, A stabilized cut finite element method for the three field stokes problem, SIAM Journal on Scientific Computing 37 (4) (2015) A1705–A1726. doi:https://doi.org/10.1137/140983574.

[43] A. Massing, M. G. Larson, A. Logg, M. E. Rognes, A stabilized nitsche overlapping mesh method for the stokes problem, Numerische Mathematik 128 (1) (2014) 73–101. doi:https://doi.org/10.1007/s00211-013-0603-z.

[44] R. Becker, E. Burman, P. Hansbo, A nitsche extended finite element method for incompressible elasticity with discontinuous modulus of elasticity, Computer Methods in Applied Mechanics and Engineering 198 (41-44) (2009) 3352–3360. doi:https://doi.org/10.1016/j.cma.2009.06.017.

[45] B. L. Freeman, A multi-point constraint unfitted finite element method, Advanced Modeling and Simulation in Engineering Sciences 9 (1) (2022) 1–22. doi:https://doi.org/10.1186/s40323-022-00232-w.

[46] S. Claus, S. Bigot, P. Kerfriden, Cutfem method for stefan-signorini problems with application in pulsed laser ablation, SIAM Journal on Scientific Computing 40 (2018) 1444–1469. doi:https://doi.org/10.1137/18M1185697.

[47] S. Farina, S. Claus, J. S. Hale, A. Skupin, S. Bordas, A cut finite element method for spatially resolved energy metabolism models in complex neuro-cell morphologies with minimal remeshing, Advanced Modeling and Simulation in Engineering Sciences 8 (1) (2021) 1–32. doi:https://doi.org/10.1186/s40323-021-00191-8.

[48] S. Claus, P. Kerfriden, A stable and optimally convergent latin-cutfem algorithm for multiple unilateral contact problems, International Journal for Numerical Methods in Engineering 113 (2018) 938–966. doi:https://doi.org/10.1002/nme.5694.

[49] S. Claus, P. Kerfriden, A cutfem method for two-phase flow problems, Computer Methods in Applied Mechanics and Engineering 348 (2019) 185–206. doi:https://doi.org/10.1016/j.cma.2019.01.009.

[50] A. Massing, M. G. Larson, A. Logg, Efficient implementation of finite element methods on nonmatching and overlapping meshes in three dimensions, SIAM Journal on Scientific Computing 35 (1) (2013) C23–C47. doi:https://doi.org/10.1137/11085949X.

[51] E. Burman, P. Hansbo, M. G. Larson, Cutfem based on extended finite element spaces, Numerische Mathematik (2022) 1–39doi:https://doi.org/10.1007/s00211-022-01313-z.

[52] T. Rabczuk, J.-H. Song, X. Zhuang, C. Anitescu, Extended finite element and meshfree methods, Academic Press, 2019.

[53] J. Nitsche, Über ein variationsprinzip zur lösung von dirichlet-problemen bei verwendung von teilräumen, die keinen randbedingungen unterworfen sind, in: Abhandlungen aus dem mathematischen Seminar der Universität Hamburg, Vol. 36, Springer, 1971, pp. 9–15.

[54] X. He, W. Deng, An interface penalty parameter free nonconforming cut finite element method for elliptic interface problems, Applied Numerical Mathematics 173 (2022) 434–452. doi:https://doi.org/10.1016/j.apnum.2021.12.011.

[55] S. Claus, P. Kerfriden, F. Moshfeghifar, S. Darkner, K. Erleben, C. Wong, Contact modeling from images using cut finite element solvers, Advanced Modeling and Simulation in Engineering Sciences 8 (2021) 1–23. doi:https://doi.org/10.1186/s40323-021-00197-2.

[56] P. Kerfriden, S. Claus, I. Mihai, A mixed-dimensional cutfem methodology for the simulation of fibre-reinforced composites, Advanced Modeling and Simulation in Engineering Sciences 18 (2020).

[57] B. Flemisch, A. Fumagalli, A. Scotti, A review of the xfem-based approximation of flow in fractured porous media, Advances in discretization methods (2016) 47–76doi:https://doi.org/10.1007/978-3-319-41246-7_3.

[58] P. Kerfriden, S. Claus, I. Mihai, A mixed-dimensional cutfem methodology for the simulation of fibre-reinforced composites, Advanced Modeling and Simulation in Engineering Sciences 7 (1) (2020) 1–26. doi:https://doi.org/10.1186/s40323-020-00154-5.

[59] A. Johansson, B. Kehlet, M. G. Larson, A. Logg, Multimesh finite element methods: Solving pdes on multiple intersecting meshes, Computer Methods in Applied Mechanics and Engineering 343 (2019) 672 – 689. doi:https://doi.org/10.1016/j.cma.2018.09.009.

[60] J. S. Dokken, A. Johansson, A. Massing, S. W. Funke, A multimesh finite element method for the navier–stokes equations based on projection methods,

Computer Methods in Applied Mechanics and Engineering 368 (2020) 113129. doi:https://doi.org/10.1016/j.cma.2020.113129.

[61] B. Schott, C. Ager, W. A. Wall, Monolithic cut finite element–based approaches for fluid-structure interaction, International Journal for Numerical Methods in Engineering 119 (8) (2019) 757–796. doi:https://doi.org/10.1002/nme.6072.

[62] S. Duczek, F. Duvigneau, U. Gabbert, The finite cell method for tetrahedral meshes, Finite Elements in Analysis and Design 121 (2016) 18–32. doi:https://doi.org/10.1016/j.finel.2016.07.004.

[63] F. Xu, D. Schillinger, D. Kamensky, V. Varduhn, C. Wang, M.-C. Hsu, The tetrahedral finite cell method for fluids: Immersogeometric analysis of turbulent flow around complex geometries, Computers & Fluids 141 (2016) 135–154. doi:https://doi.org/10.1016/j.compfluid.2015.08.027.

[64] S. Duczek, U. Gabbert, The finite cell method for polygonal meshes: poly-fcm, Computational Mechanics 58 (4) (2016) 587–618. doi:https://doi.org/10.1007/s00466-016-1307-x.

[65] B. Szabó, A. Düster, E. Rank, The p-version of the finite element method, Encyclopedia of computational mechanics (2004). doi:https://doi.org/10.1002/0470091355.ecm003g.

[66] M. Dauge, A. Düster, E. Rank, Theoretical and numerical investigation of the finite cell method, Journal of Scientific Computing 65 (3) (2015) 1039–1064. doi:https://doi.org/10.1007/s10915-015-9997-3.

[67] K. Larsson, S. Kollmannsberger, E. Rank, M. G. Larson, The finite cell method with least squares stabilized nitsche boundary conditions, Computer Methods in Applied Mechanics and Engineering 393 (2022) 114792. doi:https://doi.org/10.1016/j.cma.2022.114792.

[68] A. Düster, J. Parvizian, Z. Yang, E. Rank, The finite cell method for three-dimensional problems of solid mechanics, Computer methods in applied mechanics and engineering 197 (45-48) (2008) 3768–3782. doi:https://doi.org/10.1016/j.cma.2008.02.036.

[69] B. Wassermann, S. Kollmannsberger, S. Yin, L. Kudela, E. Rank, Integrating cad and numerical analysis:'dirty geometry'handling using the finite cell method, Computer Methods in Applied Mechanics and Engineering 351 (2019) 808–835. doi:https://doi.org/10.1016/j.cma.2019.04.017.

[70] D. Kamensky, M.-C. Hsu, D. Schillinger, J. A. Evans, A. Aggarwal, Y. Bazilevs, M. S. Sacks, T. J. Hughes, An immersogeometric variational framework for fluid–structure interaction: Application to bioprosthetic heart valves, Computer methods in applied mechanics and engineering 284 (2015) 1005–1053. doi:https://doi.org/10.1016/j.cma.2014.10.040.

[71] O. Marco, R. Sevilla, Y. Zhang, J. J. Ródenas, M. Tur, Exact 3d boundary representation in finite element analysis based on cartesian grids independent of the geometry, International Journal for Numerical Methods in Engineering 103 (6) (2015) 445–468. doi:https://doi.org/10.1002/nme.4914.

[72] L. Giovannelli, J. Ródenas, J. Navarro-Jimenez, M. Tur, Direct medical image-based finite element modelling for patient-specific simulation of future implants, Finite Elements in Analysis and Design 136 (2017) 37–57. doi:https://doi.org/10.1016/j.finel.2017.07.010.

[73] J. Gutiérrez-Gil, E. Nadal, O. León, O. A. G. Estrada, J. Albelda, J. Ródenas, Application of the cartesian grid finite element method to image-based bone remodelling process, in: 5th ECCOMAS Young Investigators Conference, 2019.

[74] M. Tur, J. Albelda, J. M. Navarro-Jimenez, J. J. Rodenas, A modified perturbed lagrangian formulation for contact problems, Computational Mechanics 55 (4) (2015) 737–754. doi:https://doi.org/10.1007/s00466-015-1133-6.

[75] M. Tur, J. Albelda, O. Marco, J. J. Ródenas, Stabilized method of imposing dirichlet boundary conditions using a recovered stress field, Computer Methods in Applied Mechanics and Engineering 296 (2015) 352–375. doi:https://doi.org/10.1016/j.cma.2015.08.001.

[76] J. M. Navarro-Jiménez, M. Tur, J. Albelda, J. J. Ródenas, Large deformation frictional contact analysis with immersed boundary method, Computational Mechanics 62 (4) (2018) 853–870. doi:https://doi.org/10.1007/s00466-017-1533-x.

[77] M. Ortiz, Y. Leroy, A. Needleman, A finite element method for localized failure analysis, Computer methods in applied mechanics and engineering 61 (2) (1987) 189–214. doi:https://doi.org/10.1016/0045-7825(87)90004-1.

[78] T. Belytschko, J. Fish, B. E. Engelmann, A finite element with embedded localization zones, Computer methods in applied mechanics and engineering 70 (1) (1988) 59–89. doi:https://doi.org/10.1016/0045-7825(88)90180-6.

[79] E. N. Dvorkin, A. M. Cuitiño, G. Gioia, Finite elements with displacement interpolated embedded localization lines insensitive to mesh size and distortions, International journal for numerical methods in engineering 30 (3) (1990) 541–564. doi:https://doi.org/10.1002/nme.1620300311.

[80] T. Belytschko, T. Black, Elastic crack growth in finite elements with minimal remeshing, International journal for numerical methods in engineering 45 (5) (1999) 601–620. doi:https://doi.org/10.1002/(SICI)1097-0207(19990620)45:5<601::AID-NME598>3.0.CO;2-S.

[81] N. Sukumar, N. Moës, B. Moran, T. Belytschko, Extended finite element method for three-dimensional crack modelling, International journal for numerical methods in engineering 48 (11) (2000) 1549–1570. doi:https://doi.org/10.1002/1097-0207(20000820)48:11<1549::AID-NME955>3.0.CO;2-A.

[82] P. M. Areias, T. Belytschko, A comment on the article "a finite element method for simulation of strong and weak discontinuities in solid mechanics" by a.

hansbo and p. hansbo [comput. methods appl. mech. engrg. 193 (2004) 3523–3540], Computer methods in applied mechanics and engineering 9 (195) (2006) 1275–1276. doi:10.1016/j.cma.2005.03.006.

[83] J. M. Melenk, I. Babuška, The partition of unity finite element method: basic theory and applications, Computer methods in applied mechanics and engineering 139 (1-4) (1996) 289–314. doi:https://doi.org/10.1016/S0045-7825(96)01087-0.

[84] S. Mohammadi, Extended finite element method: for fracture analysis of structures, John Wiley & Sons, 2008.

[85] N. Sukumar, D. L. Chopp, N. Moës, T. Belytschko, Modeling holes and inclusions by level sets in the extended finite-element method, Computer methods in applied mechanics and engineering 190 (46-47) (2001) 6183–6200. doi:https://doi.org/10.1016/S0045-7825(01)00215-8.

[86] J. Chessa, T. Belytschko, An extended finite element method for two-phase fluids, Journal of Applied Mechanics 70 (1) (2003) 10–17. doi:https://doi.org/10.1115/1.1526599.

[87] N. Moës, M. Cloirec, P. Cartraud, J.-F. Remacle, A computational approach to handle complex microstructure geometries, Computer methods in applied mechanics and engineering 192 (28-30) (2003) 3163–3177. doi:https://doi.org/10.1016/S0045-7825(03)00346-3.

[88] J. Yvonnet, H. L. Quang, Q.-C. He, An xfem/level set approach to modelling surface/interface effects and to computing the size-dependent effective properties of nanocomposites, Computational Mechanics 42 (1) (2008) 119–131. doi:https://doi.org/10.1007/s00466-008-0241-y.

[89] S. Wu, D. Hoxha, N. Belayachi, et al., Modeling mechanical behavior of geomaterials by the extended finite-element method, in: The Fifth International Conference on Multiscale Materials Modeling, 2010, p. xx. doi:hal-00684156.

[90] F. Liu, R. Borja, A contact algorithm for frictional crack propagation with the extended finite element method, International Journal for Numerical Methods in Engineering 70 (2008) 1489–1512. doi:https://doi.org/10.1002/nme.2376.

[91] C. Linder, F. Armero, Finite elements with embedded strong discontinuities for the modeling of failures in solids, International Journal for Numerical Methods in Engineering 72 (2007) 1391–1433. doi:https://doi.org/10.1002/nme.2042.

[92] E. Samaniego, T. Belytschko, Continuum–discontinuum modelling of shear bands, International Journal for Numerical Methods in Engineering 62 (13) (2005) 1857–1872. doi:https://doi.org/10.1002/nme.1256.

[93] E. Mikaeili, B. Schrefler, Xfem, strong discontinuities and second-order work in shear band modeling of saturated porous media, Acta Geotechnica 13 (2018) 1249–1264. doi:https://doi.org/10.1007/s11440-018-0734-6.

[94] E. Mikaeili, P. Liu, Numerical modeling of shear band propagation in porous plastic dilatant materials by xfem, Theoretical and Applied Fracture Mechanics 95 (2018) 164–176. doi:https://doi.org/10.1016/j.tafmec.2018.02.018.

[95] S. Bordas, B. Moran, Enriched finite elements and level sets for damage tolerance assessment of complex structures, Engineering Fracture Mechanics 73 (9) (2006) 1176–1201. doi:https://doi.org/10.1016/j.engfracmech.2006.01.006.

[96] P. Broumand, A. Khoei, The extended finite element method for large deformation ductile fracture problems with a non-local damage-plasticity model, Engineering Fracture Mechanics 112 (2013) 97–125. doi:https://doi.org/10.1016/j.engfracmech.2013.10.002.

[97] P.-A. Guidault, O. Allix, L. Champaney, C. Cornuault, A multiscale extended finite element method for crack propagation, Computer Methods in Applied

Mechanics and Engineering 197 (5) (2008) 381–399. doi:https://doi.org/10.1016/j.cma.2007.07.023.

[98] M. Holl, T. Rogge, S. Loehnert, P. Wriggers, R. Rolfes, 3d multiscale crack propagation using the xfem applied to a gas turbine blade, Computational mechanics 53 (1) (2014) 173–188. doi:https://doi.org/10.1007/s00466-013-0900-5.

[99] M. Duflot, The extended finite element method in thermoelastic fracture mechanics, International Journal for Numerical Methods in Engineering 74 (5) (2008) 827–847. doi:https://doi.org/10.1002/nme.2197.

[100] T. Mohammadnejad, A. Khoei, An extended finite element method for hydraulic fracture propagation in deformable porous media with the cohesive crack model, Finite Elements in Analysis and Design 73 (2013) 77–95. doi:https://doi.org/10.1016/j.finel.2013.05.005.

[101] E. Mikaeili, M. Kazemi, S. Mohammadi, Xfem modeling of cohesive crack propagation in saturated porous media, International Journal of Computing Communication and Instrumentation Engineering 3 (2016) 36–41. doi:http://dx.doi.org/10.15242/IJCCIE.AE0116012.

[102] J. C. Simo, M. Rifai, A class of mixed assumed strain methods and the method of incompatible modes, International journal for numerical methods in engineering 29 (8) (1990) 1595–1638. doi:https://doi.org/10.1002/nme.1620290802.

[103] R. I. Borja, A finite element model for strain localization analysis of strongly discontinuous fields based on standard galerkin approximation, Computer Methods in Applied Mechanics and Engineering 190 (11-12) (2000) 1529–1549. doi:https://doi.org/10.1016/S0045-7825(00)00176-6.

[104] D. Dias-da Costa, J. Alfaiate, L. Sluys, E. Júlio, A comparative study on the modelling of discontinuous fracture by means of enriched nodal and element

techniques and interface elements, International Journal of Fracture 161 (1) (2010) 97–119. doi:https://doi.org/10.1007/s10704-009-9432-6.

[105] R. I. Borja, Assumed enhanced strain and the extended finite element methods: A unification of concepts, Computer methods in applied mechanics and engineering 197 (33-40) (2008) 2789–2803. doi:https://doi.org/10.1016/j.cma.2008.01.019.

[106] E. Roubin, A. Vallade, N. Benkemoun, J.-B. Colliat, Multi-scale failure of heterogeneous materials: A double kinematics enhancement for embedded finite element method, International Journal of Solids and Structures 52 (2015) 180–196. doi:https://doi.org/10.1016/j.ijsolstr.2014.10.001.

[107] P. Hauseux, E. Roubin, D. M. Seyedi, J.-B. Colliat, Fe modelling with strong discontinuities for 3d tensile and shear fractures: application to underground excavation, Computer Methods in Applied Mechanics and Engineering 309 (2016) 269–287. doi:https://doi.org/10.1016/j.cma.2016.05.014.

[108] Y. Sun, E. Roubin, J. Shao, J.-B. Colliat, Strong discontinuity fe analysis for heterogeneous materials: The role of crack closure mechanism, Computers & Structures 251 (2021) 106556. doi:https://doi.org/10.1016/j.compstruc.2021.106556.

[109] M. Nikolić, X. N. Do, A. Ibrahimbegovic, Ž. Nikolić, Crack propagation in dynamics by embedded strong discontinuity approach: Enhanced solid versus discrete lattice model, Computer Methods in Applied Mechanics and Engineering 340 (2018) 480–499. doi:https://doi.org/10.1016/j.cma.2018.06.012.

[110] J. Čarija, M. Nikolić, A. Ibrahimbegovic, Ž. Nikolić, Discrete softening-damage model for fracture process representation with embedded strong discontinuities, Engineering Fracture Mechanics 236 (2020) 107211. doi:https://doi.org/10.1016/j.engfracmech.2020.107211.

[111] M. Poluektov, Ł. Figiel, A cut finite-element method for fracture and contact problems in large-deformation solid mechanics, Computer Methods in Applied

Mechanics and Engineering 388 (2022) 114234. doi:https://doi.org/10.1016/j.cma.2021.114234.

[112] E. A. de Souza Neto, D. Peric, D. R. Owen, Computational methods for plasticity: theory and applications, John Wiley & Sons, 2008. doi:10.1002/9780470694626.

[113] A. A. Griffith, Vi. the phenomena of rupture and flow in solids, Philosophical transactions of the royal society of london. Series A, containing papers of a mathematical or physical character 221 (582-593) (1921) 163–198.

[114] G. R. Irwin, Analysis of stresses and strains near the end of a crack traversing a plate, Journal of Applied Mechanics 24 (1957) 361–364.

[115] I. Babuška, U. Banerjee, Stable generalized finite element method (sgfem), Computer methods in applied mechanics and engineering 201 (2012) 91–111. doi:https://doi.org/10.1016/j.cma.2011.09.012.

[116] S. S. Ghorashi, N. Valizadeh, S. Mohammadi, Extended isogeometric analysis for simulation of stationary and propagating cracks, International Journal for Numerical Methods in Engineering 89 (9) (2012) 1069–1101. doi:https://doi.org/10.1002/nme.3277.

[117] J.-Y. Wu, Unified analysis of enriched finite elements for modeling cohesive cracks, Computer Methods in Applied Mechanics and Engineering 200 (45) (2011) 3031–3050. doi:https://doi.org/10.1016/j.cma.2011.05.008.

[118] R. H. J. PEERLINGS, R. DE BORST, W. A. M. BREKELMANS, J. H. P. DE VREE, Gradient enhanced damage for quasi-brittle materials, International Journal for Numerical Methods in Engineering 39 (19) (1996) 3391–3403. doi:https://doi.org/10.1002/(SICI)1097-0207(19961015)39:19<3391::AID-NME7>3.0.CO;2-D.

[119] G. Francfort, J.-J. Marigo, Revisiting brittle fracture as an energy minimization problem, Journal of the Mechanics and Physics of Solids 46 (8) (1998) 1319–1342. doi:https://doi.org/10.1016/S0022-5096(98)00034-9.

[120] B. Bourdin, G. Francfort, J.-J. Marigo, Numerical experiments in revisited brittle fracture, Journal of the Mechanics and Physics of Solids 48 (2000) 797–826. doi:https://doi.org/10.1016/S0022-5096(99)00028-9.

[121] B. Bourdin, G. A. Francfort, J.-J. Marigo, The variational approach to fracture, Journal of Elasticity 91 (2008) 5–148. doi:https://doi.org/10.1007/s10659-007-9107-3.

[122] X. Zhuang, S. Zhou, G. Huynh, P. Aerias, T. Rabczuk, Phase field modelling and computer implementation: A review, Engineering Fracture Mechanics (2022) 108234doi:10.1016/j.engfracmech.2022.108234.

[123] M. J. Bordena, T. J. Hughesb, C. M. Landisb, A. Anvaric, I. J. Lee, A phase-field formulation for fracture in ductile materials: Finite deformation balance law derivation, plastic degradation, and stress triaxiality effects, Computer Methods in Applied Mechanics and Engineering 312 (2016) 130–166. doi:https://doi.org/10.1016/j.cma.2016.09.005.

[124] C. Miehe, F. Aldakheel, A. Raina, Phase field modeling of ductile fracture at finite strains: A variational gradient-extended plasticity-damage theory, International Journal of Plasticity 84 (2016) 1–32. doi:https://doi.org/10.1016/j.ijplas.2016.04.011.

[125] T. K. Mandal, V. P. Nguyen, J.-Y. Wu, Length scale and mesh bias sensitivity of phase-field models for brittle and cohesive fracture, Engineering Fracture Mechanics 217 (2019) 106532. doi:https://doi.org/10.1016/j.engfracmech.2019.106532.

[126] C. V. Verhoosel, R. de Borst, A phase-field model for cohesive fracture, International Journal for Numerical Methods in Engineering 96 (2013) 43–62. doi:https://doi.org/10.1002/nme.4553.

[127] J. Vignollet, S. May, R. de Borst, C. V. Verhoosel, Phase-field models for brittle and cohesive fracture, Meccanica 49 (2014) 2587–2601. doi:https://doi.org/10.1007/s11012-013-9862-0.

[128] A. Karma, D. A. Kessler, H. Levine, Phase-field model of mode iii dynamic fracture, Phys. Rev. Lett. 87 (2001) 045501. doi:10.1103/PhysRevLett.87.045501.

[129] H. Henry, H. Levine, Dynamic instabilities of fracture under biaxial strain using a phase field model, Phys. Rev. Lett. 93 (2004) 105504. doi:10.1103/PhysRevLett.93.105504.

[130] K. Pham, H. Amor, J.-J. Marigo, C. Maurini, Gradient damage models and their use to approximate brittle fracture, International Journal of Damage Mechanics 20 (4) (2011) 618–652. doi:10.1177/1056789510386852.

[131] J.-Y. Wu, A unified phase-field theory for the mechanics of damage and quasi-brittle failure, Journal of the Mechanics and Physics of Solids 103 (2017) 72–99. doi:https://doi.org/10.1016/j.jmps.2017.03.015.

[132] V. P. Nguyen, J.-Y. Wu, Modeling dynamic fracture of solids with a phase-field regularized cohesive zone model, Computer Methods in Applied Mechanics and Engineering 340 (2018) 1000–1022. doi:https://doi.org/10.1016/j.cma.2018.06.015.

[133] A. Singh, T. S. Sandhu, S. Pal, Interplay of various fracture mechanisms in bio-inspired staggered structure, Mechanics of Materials 139 (2019) 103215. doi:https://doi.org/10.1016/j.mechmat.2019.103215.

[134] C. Miehe, L.-M. Schaenzel, H. Ulmer, Phase field modeling of fracture in multi-physics problems. part i. balance of crack surface and failure criteria for brittle crack propagation in thermo-elastic solids, Computer Methods in Applied Mechanics and Engineering 294 (2015) 449–485. doi:https://doi.org/10.1016/j.cma.2014.11.016.

[135] S. Burke, C. Ortner, E. Süli, An adaptive finite element approximation of a variational model of brittle fracture, SIAM Journal on Numerical Analysis 48 (2010) 980–1012. doi:https://doi.org/10.1137/080741033.

[136] T. Heister, M. F. Wheeler, T. Wick, A primal-dual active set method and predictor-corrector mesh adaptivity for computing fracture propagation using a phase-field approach, Computer Methods in Applied Mechanics and Engineering 290 (2015) 466–495. doi:https://doi.org/10.1016/j.cma.2015.03.009.

[137] H. Hirshikesh, A. Pramod, H. Waisman, S. Natarajan, Adaptive phase field method using novel physics based refinement criteria, Computer Methods in Applied Mechanics and Engineering 383 (2021) 113874. doi:https://doi.org/10.1016/j.cma.2021.113874.

[138] T. Wick, Goal functional evaluations for phase-field fracture using pu-based dwr mesh adaptivity, Computational Mechanics 57 (6) (2016) 1017–1035. doi:https://doi.org/10.1007/s00466-016-1275-1.

[139] S. Weißer, T. Wick, The dual-weighted residual estimator realized on polygonal meshes, Computational Methods in Applied Mathematics 18 (4) (2018) 753–776. doi:https://doi.org/10.1515/cmam-2017-0046.

[140] O. A. González-Estrada, E. Nadal, J. Ródenas, P. Kerfriden, S. P.-A. Bordas, F. Fuenmayor, Mesh adaptivity driven by goal-oriented locally equilibrated superconvergent patch recovery, Computational Mechanics 53 (5) (2014) 957–976. doi:https://doi.org/10.1007/s00466-013-0942-8.

[141] F. Tian, X. Tang, T. Xu, J. Yang, L. Li, A hybrid adaptive finite element phase-field method for quasi-static and dynamic brittle fracture, International Journal for Numerical Methods in Engineering 120 (9) (2019) 1108–1125. doi:https://doi.org/10.1002/nme.6172.

[142] R. Patil, B. Mishra, I. Singh, An adaptive multiscale phase field method for brittle fracture, Computer Methods in Applied Mechanics and Engineering 329 (2018) 254–288. doi:https://doi.org/10.1016/j.cma.2017.09.021.

[143] B. Budiansky, On the elastic moduli of some heterogeneous materials, Journal of the Mechanics and Physics of Solids 13 (4) (1965) 223–227. doi:https://doi.org/10.1016/0022-5096(65)90011-6.

[144] R. Hill, A self-consistent mechanics of composite materials, Journal of the Mechanics and Physics of Solids 13 (4) (1965) 213–222. doi:https://doi.org/10.1016/0022-5096(65)90010-4.

[145] J. W. Hutchinson, Bounds and self-consistent estimates for creep of polycrystalline materials, Proceedings of the Royal Society of London. Series A, Mathematical and Physical Sciences 348 (1652) (1976) 101–127.
URL http://www.jstor.org/stable/79120

[146] M. Berveiller, A. Zaoui, An extension of the self-consistent scheme to plastically-flowing polycrystals, Journal of the Mechanics and Physics of Solids 26 (5) (1978) 325–344. doi:https://doi.org/10.1016/0022-5096(78)90003-0.

[147] W. Voigt, Ueber die beziehung zwischen den beiden elasticitätsconstanten isotroper körper, Annalen der Physik 274 (12) (1889) 573–587. doi:https://doi.org/10.1002/andp.18892741206.

[148] A. Reuss, Berechnung der fließgrenze von mischkristallen auf grund der plastizitätsbedingung für einkristalle ., ZAMM - Journal of Applied Mathematics and Mechanics / Zeitschrift für Angewandte Mathematik und Mechanik 9 (1) (1929) 49–58. doi:https://doi.org/10.1002/zamm.19290090104.

[149] Z. Hashin, S. Shtrikman, A variational approach to the theory of the elastic behaviour of multiphase materials, Journal of the Mechanics and Physics of Solids 11 (2) (1963) 127–140. doi:https://doi.org/10.1016/0022-5096(63)90060-7.

[150] T. Mori, K. Tanaka, Average stress in matrix and average elastic energy of materials with misfitting inclusions, Acta Metallurgica 21 (5) (1973) 571–574. doi:https://doi.org/10.1016/0001-6160(73)90064-3.

[151] I. Babuška, Solution of interface problems by homogenization. i, SIAM Journal on Mathematical Analysis 7 (5) (1976) 603–634.

[152] F. Feyel, A multilevel finite element method fe2 to describe the response of highly non-linear structures using generalized continua, Computer Methods in Applied Mechanics and Engineering 192 (28) (2003) 3233–3244. doi:https://doi.org/10.1016/S0045-7825(03)00348-7.

[153] F. Feyel, Multiscale fe2 elastoviscoplastic analysis of composite structures, Computational Materials Science 16 (1-4) (1999) 344–354. doi:https://doi.org/10.1016/S0927-0256(99)00077-4.

[154] F. Vernerey, W. K. Liu, B. Moran, Multi-scale micromorphic theory for hierarchical materials, Journal of the Mechanics and Physics of Solids 55 (12) (2007) 2603–2651. doi:https://doi.org/10.1016/j.jmps.2007.04.008.

[155] W. K. Liu, C. McVeigh, Predictive multiscale theory for design of heterogeneous materials, Computational Mechanics 42 (2) (2008) 147–170. doi:https://doi.org/10.1007/s00466-007-0176-8.

[156] V. Kouznetsova, M. G. Geers, W. Brekelmans, Multi-scale second-order computational homogenization of multi-phase materials: a nested finite element solution strategy, Computer methods in applied Mechanics and Engineering 193 (48-51) (2004) 5525–5550. doi:https://doi.org/10.1016/j.cma.2003.12.073.

[157] E. Bosco, V. Kouznetsova, E. Coenen, M. Geers, A. Salvadori, A multiscale framework for localizing microstructures towards the onset of macroscopic discontinuity, Computational Mechanics 54 (2) (2014) 299–319. doi:https://doi.org/10.1007/s00466-014-0986-4.

[158] P. J. Sanchez, P. J. Blanco, A. E. Huespe, R. A. Feijóo, Failure-oriented multi-scale variational formulation: micro-structures with nucleation and evolution of softening bands, Computer Methods in Applied Mechanics and Engineering 257 (2013) 221–247. doi:https://doi.org/10.1016/j.cma.2012.11.016.

[159] V. P. Nguyen, O. Lloberas-Valls, M. Stroeven, L. J. Sluys, Computational homogenization for multiscale crack modeling. implementational and computational aspects, International Journal for Numerical Methods in Engineering 89 (2) (2012) 192–226. doi:https://doi.org/10.1002/nme.3237.

[160] E. Coenen, V. Kouznetsova, M. Geers, Multi-scale continuous–discontinuous framework for computational-homogenization–localization, Journal of the Mechanics and Physics of Solids 60 (8) (2012) 1486–1507. doi:https://doi.org/10.1016/j.jmps.2012.04.002.

[161] A. Toselli, O. Widlund, Domain decomposition methods-algorithms and theory, Vol. 34, Springer Science & Business Media, 2004.

[162] P. Le Tallec, Y.-H. De Roeck, M. Vidrascu, Domain decomposition methods for large linearly elliptic three-dimensional problems, Journal of Computational and Applied Mathematics 34 (1) (1991) 93–117. doi:https://doi.org/10.1016/0377-0427(91)90150-I.

[163] C. Farhat, F.-X. Roux, A method of finite element tearing and interconnecting and its parallel solution algorithm, International journal for numerical methods in engineering 32 (6) (1991) 1205–1227. doi:https://doi.org/10.1002/nme.1620320604.

[164] J. T. Oden, T. I. Zohdi, Analysis and adaptive modeling of highly heterogeneous elastic structures, Computer methods in applied mechanics and engineering 148 (3-4) (1997) 367–391. doi:https://doi.org/10.1016/S0045-7825(97)00032-7.

[165] T. Zohdi, P. Wriggers, C. Huet, A method of substructuring large-scale computational micromechanical problems, Computer Methods in Applied Mechanics

and Engineering 190 (43) (2001) 5639–5656. doi:https://doi.org/10.1016/S0045-7825(01)00189-X.

[166] P. Ladevèze, O. Loiseau, D. Dureisseix, A micro–macro and parallel computational strategy for highly heterogeneous structures, International Journal for Numerical Methods in Engineering 52 (1-2) (2001) 121–138. doi:https://doi.org/10.1002/nme.274.

[167] P. Ladevèze, J.-C. Passieux, D. Néron, The latin multiscale computational method and the proper generalized decomposition, Computer Methods in Applied Mechanics and Engineering 199 (21-22) (2010) 1287–1296. doi:https://doi.org/10.1016/j.cma.2009.06.023.

[168] A. Akbari-Rahimabadi, P. Kerfriden, S. Bordas, Scale selection in nonlinear fracture mechanics of heterogeneous materials, Philosophical Magazine 95 (2015) 3328–3347. doi:https://doi.org/10.1080/14786435.2015.1061716.

[169] B. Raju Akula, J. Vignollet, V. A. Yastrebov, Stabilized mortex method for mesh tying along embedded interfaces, arXiv e-prints (2019) arXiv–1902doi:https://doi.org/10.48550/arXiv.1902.04003.

[170] Z. C. WaiChing Sun, J. Choo, Mixed arlequin method for multiscale poromechanics problems, International Journal for Numerical Methods in Engineering 111 (2017) 624–659. doi:https://doi.org/10.1002/nme.5476.

[171] L. Gendre, A. Olivier, P. Gosselet, F. Comte, Non-intrusive and exact global/local techniques for structural problems with local plasticity, Computational Mechanics 44 (2009) 233–245. doi:https://doi.org/10.1007/s00466-009-0372-9.

[172] M. Wangermez, O. Allix, P.-A. Guidault, O. Ciobanu, C. Rey, Non-intrusive global-local analysis of heterogeneous structures based on a second-order interface coupling, Computational Mechanics 69 (5) (2022) 1241–1257. doi:https://doi.org/10.1007/s00466-022-02141-6.

[173] T. Gerasimov, N. Noii, O. Allix, L. De Lorenzis, A non-intrusive global/local approach applied to phase-field modeling of brittle fracture, Advanced modeling and simulation in engineering sciences 5 (1) (2018) 1–30. doi:https://doi.org/10.1186/s40323-018-0105-8.

[174] F. Aldakheel, N. Noii, T. Wick, P. Wriggers, A global–local approach for hydraulic phase-field fracture in poroelastic media, Computers & Mathematics with Applications 91 (2021) 99–121. doi:https://doi.org/10.1016/j.camwa.2020.07.013.

[175] L. Gendre, A. Olivier, P. Gosselet, A two-scale approximation of the schur complement and its use for non-intrusive coupling, International Journal for Numerical Methods in Engineerings 87 (2011) 889–905. doi:https://doi.org/10.1002/nme.3142.

[176] O. Bettinotti, O. Allix, B. Malherbe, A coupling strategy for adaptive local refinement in space and time with a fixed global model in explicit dynamics, Computational Mechanics 53 (4) (2014) 561–574. doi:https://doi.org/10.1007/s00466-013-0917-9.

[177] P. Gupta, J. Pereira, D.-J. Kim, C. Duarte, T. Eason, Analysis of three-dimensional fracture mechanics problems: A non-intrusive approach using a generalized finite element method, Engineering Fracture Mechanics 90 (2012) 41–64. doi:https://doi.org/10.1016/j.engfracmech.2012.04.014.

[178] Z. Li, The immersed interface method using a finite element formulation, Applied Numerical Mathematics 27 (3) (1998) 253–267. doi:https://doi.org/10.1016/S0168-9274(98)00015-4.

[179] Y. Liu, Q. Sun, X. Fan, A non-intrusive global/local algorithm with non-matching interface: derivation and numerical validation, Computer Methods in Applied Mechanics and Engineering 277 (2014) 81–103. doi:https://doi.org/10.1016/j.cma.2014.04.012.

[180] P. Gosselet, M. Blanchard, O. Allix, G. Guguin, Non-invasive global–local coupling as a schwarz domain decomposition method: acceleration and generalization, Advanced Modeling and Simulation in Engineering Sciences 5 (1) (2018) 1–23. doi:https://doi.org/10.1186/s40323-018-0097-4.

[181] B. He, L. Schuler, P. Newell, A numerical-homogenization based phase-field fracture modeling of linear elastic heterogeneous porous media, Computational Materials Science 176 (2020) 109519. doi:https://doi.org/10.1016/j.commatsci.2020.109519.

[182] M. Ambati, T. Gerasimov, L. De Lorenzis, A review on phase-field models of brittle fracture and a new fast hybrid formulation, Computational Mechanics 55 (2015) 383–405. doi:https://doi.org/10.1007/s00466-014-1109-y.

[183] V. Kouznetsova, M. G. Geers, W. M. Brekelmans, Multi-scale constitutive modelling of heterogeneous materials with a gradient-enhanced computational homogenization scheme, International journal for numerical methods in engineering 54 (8) (2002) 1235–1260. doi:https://doi.org/10.1002/nme.541.

[184] V. G. Kouznetsova, M. Geers, W. Brekelmans, Size of a representative volume element in a second-order computational homogenization framework, International Journal for Multiscale Computational Engineering 2 (4) (2004). doi:10.1615/IntJMultCompEng.v2.i4.50.

[185] Ł. Kaczmarczyk, C. J. Pearce, N. Bićanić, Scale transition and enforcement of rve boundary conditions in second-order computational homogenization, International Journal for Numerical Methods in Engineering 74 (3) (2008) 506–522. doi:https://doi.org/10.1002/nme.2188.

[186] N. Nguyen, J. Yvonnet, J. Réthoré, A. B. Tran, Identification of fracture models based on phase field for crack propagation in heterogeneous lattices in a context of non-separated scales, Computational Mechanics 63 (2018) 1047–1068. doi:https://doi.org/10.1007/s00466-018-1636-z.

[187] M. Hossain, C.-J. Hsueh, B. Bourdin, K. Bhattacharya, Effective toughness of heterogeneous media, Journal of the Mechanics and Physics of Solids 71 (2014) 15–32. doi:https://doi.org/10.1016/j.jmps.2014.06.002.

[188] P. Cheng, H. Zhu, W. Sun, Y. Shen, J. Fish, A concurrent multiscale approach for fracturing of brittle composites based on the superposition-based phase field model, International Journal for Multiscale Computational Engineering 20 (2) (2022). doi:10.1615/IntJMultCompEng.2022042334.

[189] E. Mikaeili, S. Claus, P. Kerfriden, Concurrent multiscale analysis without meshing: Microscale representation with cutfem and micro/macro model blending, Computer Methods in Applied Mechanics and Engineering 393 (2022) 114807. doi:https://doi.org/10.1016/j.cma.2022.114807.

[190] V. Hernandez, J. E. Roman, V. Vidal, Slepc: A scalable and flexible toolkit for the solution of eigenvalue problems, ACM Trans. Math. Softw. 31 (3) (2005) 351–362. doi:10.1145/1089014.1089019.

[191] M. Imani, A. M. Goudarzi, S. M. Rabiee, M. Dardel, The modified mori-tanaka scheme for the prediction of the effective elastic properties of highly porous ceramics, Ceramics International 44 (14) (2018) 16489 – 16497. doi:https://doi.org/10.1016/j.ceramint.2018.06.066.

[192] T. Mura, Micromechanics of Defects in Solids, Springer Netherlands, 1987. doi:10.1007/978-94-009-3489-4.

[193] E. Perilli, F. Baruffaldi, F. T. M. Visentin, B. Bordini, A. Capperllo, M. Vicenconti, Micro-ct examination of human bone specimens: effects of polymethylmethacrylate embedding on structural parameters, Journal of Microscopy 225 (2007) 192–200. doi:10.1111/j.1365-2818.2007.01731.x.

[194] R. Fletcher, Practical methods of optimization (2000). doi:10.1002/9781118723203.

[195] E. Mikaeili, S. Claus, P. Kerfriden, A novel hierarchical multiresolution framework using cutfem, arXiv preprint arXiv:2201.04698 (2022). doi:https://doi.org/10.48550/arXiv.2201.04698.

[196] M. Alnæs, J. Blechta, J. Hake, A. Johansson, B. Kehlet, A. Logg, C. Richardson, J. Ring, M. Rognes, G. Wells, The fenics project version 1.5, Archive of Numerical Software 3 (01 2015). doi:10.11588/ans.2015.100.20553.

[197] M. S. Alnæs, A. Logg, K. B. Ølgaard, M. E. Rognes, G. N. Wells, Unified form language: A domain-specific language for weak formulations of partial differential equations, Association for Computing Machinery 40 (2014).

[198] A. Logg, G. N. Wells, Dolfin: Automated finite element computing, ACM Trans. Math. Softw. 37 (apr 2010).